Amorphous Glass-Coated Ferromagnetic Wires in Microwave Engineering

A dissertation by

Iñigo Liberal

under the supervision of

Ramón Gonzalo and **Iñigo Ederra**

submitted in fulfillment of the requirements for the degree of
Doctor of Philosophy at the Public University of Navarra

Department of Electrical and Electronic Engineering

Pamplona, May 2013

Universidad Pública de Navarra
Nafarroako Unibertsitate Publikoa

Start it as a stranger,
finish it as a friend.

upna
Universidad Pública de Navarra
Nafarroako Unibertsitate Publikoa

Abstract

This dissertation deals with the use of glass-coated amorphous ferromagnetic wires in microwave engineering. To this end, analytical and equivalent circuit models of the scattering of electromagnetic fields by a single ferromagnetic wire are formulated. Those models are employed to study the main phenomena related to the scattering by a ferromagnetic wire, including the transition from surface to bulk effects, and the multiple peculiarities of the absorption spectrum. Fundamental limits on the balance of powers involved in the scattering problem, as well as their technological implications, are also addressed. Moreover, structures composed of several ferromagnetic wires are modeled as artificial electromagnetic materials (which are found to belong to the class of artificial dielectrics with magnetically controlled permittivity) and artificial impedance surfaces.

Based on these fundamental studies, reconfigurable electromagnetic absorbers and mechanical-stress contact-less sensors are identified as the most promising applications. In this regard, proof-of-concept designs of a wideband absorber with a reconfigurable non-absorbing notch, and a reconfigurable absorber with a narrow absorbing band are presented. These absorbers could be employed in practice to track objects hidden to external observers and to mitigate interferences in wireless communications. As for contact-less sensing, a retrieval technique aimed to characterize the wires under mechanical-stresses is introduced. The frequency position of the natural ferromagnetic resonance of the studied wires is seen to increase along with elongation, which suggests a potential use as contactless sensors for architectural and health monitoring.

upna
Universidad Pública de Navarra
Nafarroako Unibertsitate Publikoa

Resumen

En esta tesis se ha estudiado el uso de hilos ferromagnéticos recubiertos de vidrio en ingeniería de microondas. Para este fin, se han formulado modelos analíticos y equivalentes circuitales de la interacción entre un hilo ferromagnético y campos electromagnéticos. Dichos modelos se han utilizado para estudiar los fenómenos más relevantes relacionados con la interacción entre un hilo ferromagnético y campos electromagnéticos, incluyendo la transición de efectos superficiales a volumétricos, y las múltiples peculiaridades del espectro de absorción. Además, se han investigado los límites fundamentales en el equilibrio de potencias presente en interacciones de un hilo ferromagnético con campos electromagnéticos, así como sus implicaciones tecnológicas. Estructuras consistentes en varios hilos ferromagnéticos se han modelado como materiales electromagnéticos artificiales (los cuales pertenecen a la clase de materiales dieléctricos con permitividad controlada por las propiedades magnéticas de los hilos) y superficies artificiales.

Basado en estos estudios fundamentales, absorbentes electromagnéticos reconfigurables y sensores de estrés mecánico basados en técnicas de radar se han identificado como las aplicaciones más prometedoras. A este respecto, se han presentado diseños de prueba de concepto de un absorbente de banda ancha con una banda estrecha de reflexión, y un absorbente de banda estrecha. Dichos dispositivos podrían utilizarse en la práctica para monitorizar objetos ocultos a observadores externos, y para mitigar interferencias en comunicaciones inalámbricas. En lo concerniente a sensores de estrés mecánico basados en técnicas de radar, se ha presentado un procedimiento para caracterizar los hilos bajo estreses mecánicos. Utilizando dicha técnica se han caracterizado hilos en los que la posición en frecuencia de la resonancia ferromagnética natural aumenta en función del estrés aplicado. Estos resultados sugieren el uso de hilos ferromagnéticos para monitorizar estructuras arquitectónicas e implantes.

Contents

Universidad Pública de Navarra
Nafarroako Unibertsitate Publikoa

Chapter 1

Introduction

This preliminary chapter explains the background, goal and motivation of this work. For the sake of clarity, it starts introducing some basic concepts concerning amorphous glass-coated ferromagnetic wires, their fabrication and properties.

1.1 Amorphous Glass-Coated Ferromagnetic Wires

Amorphous glass-coated ferromagnetic wires consist of a metallic amorphous wire, with a diameter typically in the order of microns, covered with a Pyrex coating [1]. Fig. 1.1 represents a Scanning Electron Microscope (SEM) image of one of these wires.

These wires are fabricated by means of a modified Taylor-Ulitovsky method, described in Section 1.1.1, in which both coating and metallic

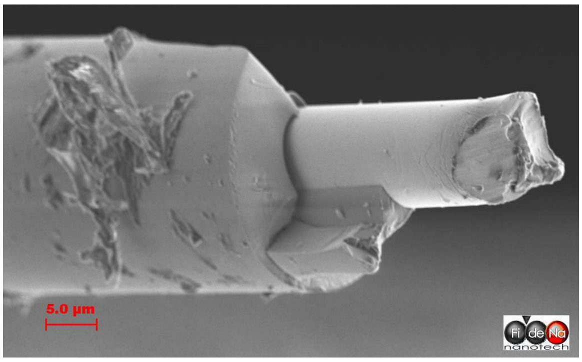

Figure 1.1 – SEM image of a glass-coated amorphous ferromagnetic wire. The image was taken at the Foundation for the Research and Development of Nanotechnology in Navarra (Fidena) with the assistance of J. Bravo.

core are processed at the same time. On the one hand, Pyrex-type borosilicate compositions are usually employed for the wire coating. Note that the coating is not selected due to its electromagnetic properties, but in order to fulfill the technological demands of the fabrication process. On the other hand, the metallic core is made of a complex alloy, e.g., (CoFeNiMn)(SiBCMo) [2], which is selected on the basis of its electrical and magnetic properties. In particular, (CoFeNiMn) are the main alloy elements that determine the ferromagnetic properties of the wire, and (SiBCMo) are added to enable the amorphicity of the alloy. Additional components such as Cr can also be employed in order to enhance chemical properties of the alloy, such as corrosion resistance.

Amorphous glass-coated ferromagnetic wires are known to feature good mechanical, electric and, more importantly, magnetic properties, such as Large Barkhausen jump (LBE) [3], Giant Magneto Impedance (GMI) [4] and Natural Ferromagnetic Resonance (NFMR) [5]. Because of that, amorphous glass-coated ferromagnetic wires have a wide range of potential applications, and have been traditionally demanded in the sensing field [6]. A survey of their more relevant properties has been included in Section 1.1.2.

For the sake of brevity, amorphous glass-coated ferromagnetic wires will be simply referred to as "ferromagnetic wires" along this dissertation. Naturally, there are other structures that might be also labeled as ferromagnetic wires. However, this abuse of language has been considered necessary to simplify the reading of the dissertation and the illustration of the results.

1.1.1 Fabrication Process

Amorphous glass-coated ferromagnetic wires are fabricated by rapid quenching from the melt by using the modified Taylor-Ulitovsky method [7, 8], also known as the glass-coated melt spinning method. All the wires measured in this dissertation have been fabricated through such technique in collaboration with Prof. M. Vázquez at the Material Science Institute of Madrid (ICMM), Group of Nanomagnetism and Magnetization Processes.

Fig. 1.2 represents a schematic drawing (extracted from [9]) of the Taylor-Ulitovsky fabrication process, as well as a photograph taken during the fabrication of the wires at the Material Science Institute of Madrid (ICMM). The process can be summarized as follows: In the first place, the metallic alloy that composes the core is put into a Pyrex-like glass

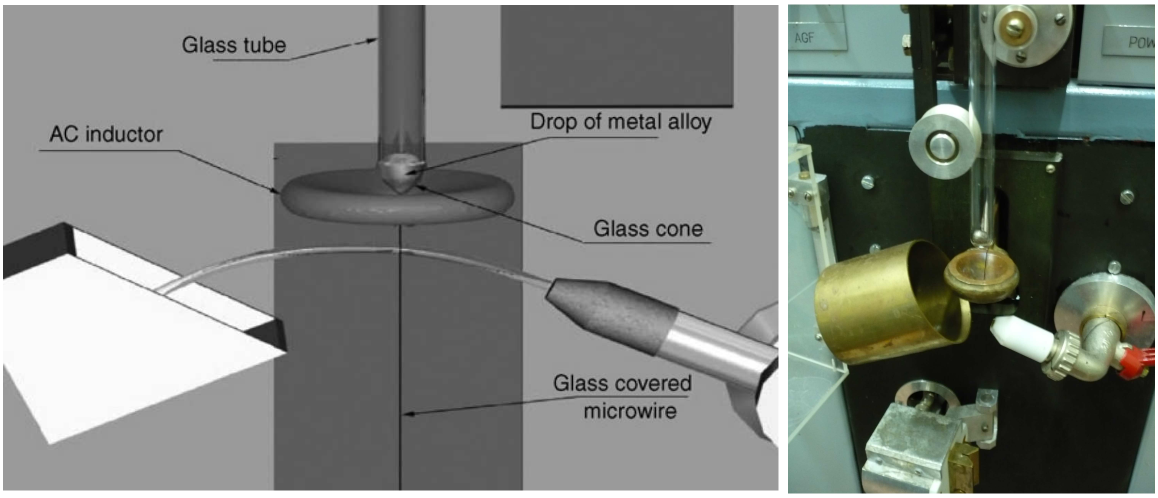

Figure 1.2 – Schematic drawing (extracted from [9]) of the Taylor-Ulitovsky fabrication process, and photograph taken during the fabrication of the wires at the Material Science Institute of Madrid (ICMM)

tube and placed within a coil, which acts as a heater. Then, the alloy is melted by the field produced by the coil and the end of the glass tube is softened, enveloping the metal. Hence, around the molten metal there is a glass cover which allows the drawing of the capillarity. Along this process the glass tube displaces down, and the as-formed wire is cooled by a water jet. High cooling rates are needed to form a continuous wire, namely, to achieve solidification before breaking into droplets. Finally, the wire is collected by a spinning wheel as it falls down below the cooling system. In this manner, the outcome is a wire forming a roll with lengths typically on the order of hundreds of meters - kilometers [9]. Fig. 1.3 includes a photograph of a single ferromagnetic wire forming a roll, which was taken during the fabrication of the wires at the Material Science Institute of Madrid (ICMM).

The geometrical parameters of the wire can be controlled during the fabrication process. On the one hand, the radius of the metallic core can be adjusted by varying the wires drawing speed, increasing when it decreases. On the other hand, the thickness of the glass cover is controlled by the glass tubes displacement speed, increasing when it increases. Typical core radius ranges between 1 μm and 50 μm. The thickness of the coating is in the range of 2 μm to 15 μm. However, recent advances in the processing technique have produced metallic cores of submicron- (400 nm radius [10]) and nano- (45 nm radius [11]) dimensions. These results pave the way to an inexpensive and mass production of ferromagnetic

Figure 1.3 – Photograph of a single ferromagnetic wire forming a roll. (The photograph was taken during the fabrication of the wires at the Material Science Institute of Madrid (ICMM))

nanowires.

While the composition of the metallic alloy is generally selected to tailor the wire electromagnetic properties, the coating is selected for technological reasons associated to the fabrication process. In particular, Pyrex-type borosilicate compositions are usually employed to fulfill the fabrication requirements, which are given in terms of drawing temperature, thermal expansion coefficient, viscosity, and chemical activity with the metallic core [12].

To sum up, some of the main advantages of this fabrication process are [9]:

1. The wires are produced in a one-step process.
2. Repeatability of wire properties at mass production.
3. Wide range of variation in parameters (geometrical and physical).
4. Fabrication of continuous long pieces of wires up to 10.000 m.
5. Control and adjustment of geometrical parameters.

Furthermore, the glass-coated wires can be further post-processed after the wire formation to improve their properties for particular applications. In some cases, the glass-coating is removed by chemical dissolution, which can be convenient, for example, to increase the sensibility of magnetic sensors [2]. In these cases, the glass is etched with a hydrofluoric acid, whose solution must be controlled to avoid etching of the metal core. Note that the glass removal affects the internal stresses of the wire, and therefore the impact of the glass removal on the wire magnetic properties must be taken into account.

The fabricated glass-coated wires can also be subjected to thermal treatments in order to improve their magnetic properties [13]. These annealing processes give rise to a variety of effects such as structural relaxation, growing of crystallites and appearance of new phases depending on the annealing temperature and the wire composition, which leads to a magnetic softening o hardening of the amorphous material [14].

1.1.2 Properties

This Section introduces a survey of the most relevant mechanical, chemical, electrical and magnetic properties of ferromagnetic wires.

Mechanical Properties

Due to their amorphous nature, ferromagnetic wires lack of long-range chemical and topological order, performing superior mechanical properties than crystalline composites. A review of the mechanical properties of these wires can be found in [15].

In summary, amorphous glass-coated ferromagnetic wires bring together ductile behavior at bending, shearing and compression; as well as high values of fracture strength. Moreover, the mechanical properties of ferromagnetic wires depend very strongly on their dimensions, being the glass cover thickness the most influential parameter. This fact is not only due to the mechanical properties of the cover, but also to the stresses induced in the metallic core. Consequently, the glass removal influences the mechanical properties of the wires, increasing their elongation, but reducing the fracture strength limit. Furthermore, annealing affects the internal stresses of the wires, and therefore it also has an impact on their mechanical properties, which vary as a function of the core composition.

Chemical Properties

As other amorphous metals, ferromagnetic wires are characterized high corrosion resistances, produced by their chemical and structural homogeneity. Moreover, the chemical resistance of these wires can be improved by the addition of other materials to the alloy, such as Cr, leading to corrosion resistances even higher than those of stainless steels. Furthermore, the glass coating can be selected to prevent corrosion at specific environments [2].

Electrical Properties

Amorphous glass-coated ferromagnetic wires are electric conductors, though their conductivities are typically 100 times smaller than their crystalline counterparts. Therefore, their conductivity is mainly defined by the structural disorder, while it is quite stable against temperature changes. Typical values of electrical conductivity at room temperature are around 10^5 S/m for Fe-rich and Co-rich wires [2].

Magnetic Properties

Amorphous glass-coated ferromagnetic wires present outstanding magnetic properties, Large Barkhausen jump (LBE) [3], Giant Magneto Impedance (GMI) [4] and Natural Ferromagnetic Resonance (NFMR) [5]. Therefore, most of the research on these wires has been focused on the investigation of their magnetic properties.

- **Magnetic Properties as a Function of Composition and Geometry**

The magnetic properties of the wires are determined by the properties of the alloy forming the core, as well as the distribution of internal stresses in the core. Thus, these properties can be tailored through the composition and geometry of the wires.

In the first place, the metals which compound the alloy of the ferromagnetic core determine the sign and magnitude of the magnetostriction constant. On the one hand, Fe-rich wires have a positive magnetostriction constant, which leads to a square bistable hysteresis loop (see Fig. 1.4(c)); characterized by a large and unique Barkhausen jump, being the

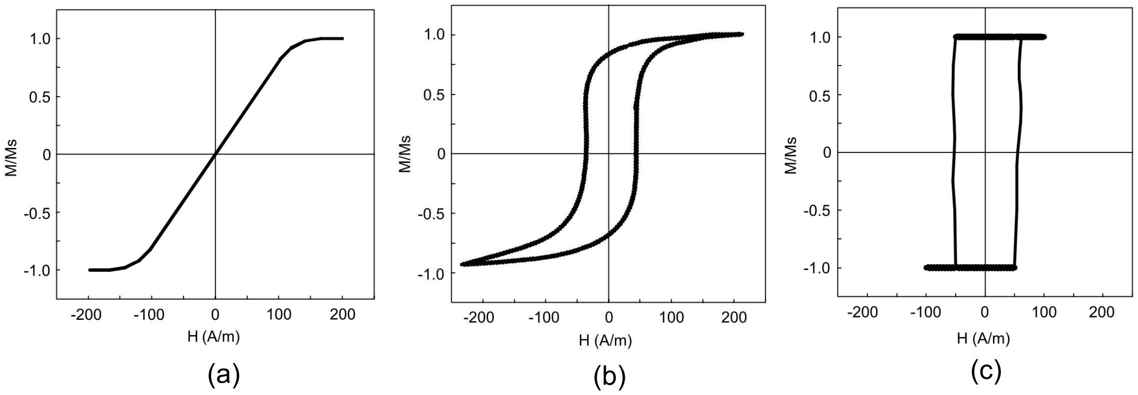

Figure 1.4 – Typical hysteresis loops corresponding to wires with different magnetostriction constant: (a) negative, (b) vanishing but negative, and (c) positive (Figures extracted from [9].)

remanence magnetization almost equal to the magnetization at saturation. On the contrary, Co-based wires have a negative magnetostriction constant, exhibiting minimal hysteresis (see Fig. 1.4(a)). Interestingly, Co-rich wires with a given proportion of Fe are characterized by a very small and negative magnetostriction constant (see Fig. 1.4(b)), and the magnetization process take place first by domain wall motion and then by magnetization orientation.

Secondly, the geometrical dimensions of the wires have control over the distribution of internal stresses produced during the fabrication, and thus over the magnetic properties. These stresses are mainly due to the solidification process, differences between the thermal coefficients of metal and glass, and the mechanical drawing. Although there are models that describe the internal distribution of stresses of the wires [2, 9], only the relationship between the geometrical dimensions and the magnetic properties will be included here for the sake of brevity. In this context, it has been has been shown that a reduction in the ratio between the inner core diameter and the total wire diameter, ρ, leads to a reduction of the remanence magnetization and an increase of the coercivity [3]. Moreover, the magnetization at saturation is reduced when ρ is decreased [3].

Naturally, the use of post-processing techniques on the fabrication of the wires, such as the coating removal and annealing processes, also influences their magnetic properties. For example, the coating removal modifies the internal stresses induced on the ferromagnetic core, thus altering the magnetic properties of the wires. Specifically, the coating removal diminish the axial stresses acting over the metallic core, which weakens the bistable hysteresis loop of wires with positive magntostriction constant [2].

- **Magnetoimpedance Effect**

One of the most outstanding magnetic properties of ferromagnetic wires is the Magneto Impedance (MI) effect. Along the dissertation, this effect is defined as variations on the current flowing along a ferromagnetic wire due to changes on its magnetic properties (e.g., those produced by an external magnetic field). This general definition includes any alteration of the magnetization, such as changes in the size and shape of the magnetization domains, as well as changes in the magnetization direction and strength on a single domain. In view of the significant impedance changes produced by weak magnetic fields in the MHz frequency range, the MI effect is usually regarded as giant magneto-impedance (GMI) [4,6,16–19].

This property enables the use of ferromagnetic wires as sub nT magnetic field sensors. As a matter of fact, the sensitivity, defined as the impedance change ratio per Oersted (Oe), runs into more than 100%/Oe at MHz frequencies. A similar effect is present at GHz frequencies, although the wires feature reduced sensitivities [20]. This is reflected in Fig. 1.5, which represents a typical plot of impedance as a function of the external axial magnetic field. Among ferromagnetic wires, those with vanishing but negative magnetostriction constant are usually preferred for MI based applications, since they feature a larger sensitivity as a consequence of their circumferential anisotropy.

- **Ferromagnetic Resonance**

At microwave frequencies, the magnetic behavior of the wires is dominated by the Ferromagnetic Resonance (FMR) [1, 21]. This effect originates on the precessional motion of the magnetization of a ferromagnetic material in response to an external magnetic field. Macroscopically, it leads to a gyrotropic permeability tensor whose components follow a Lorentzian frequency domain behavior [22, 23]. The presence and characteristics of the FMR in wires is typically investigated by inspecting the absorption spectrum of the wires, which is measured in resonant cavities [24–26] microstrip lines [27] and/or coaxial lines [28–30].

The FMR in wires with positive and large magnetostriction constants (e.g., Fe-rich wires) is of particular interest. The reason for this is that a

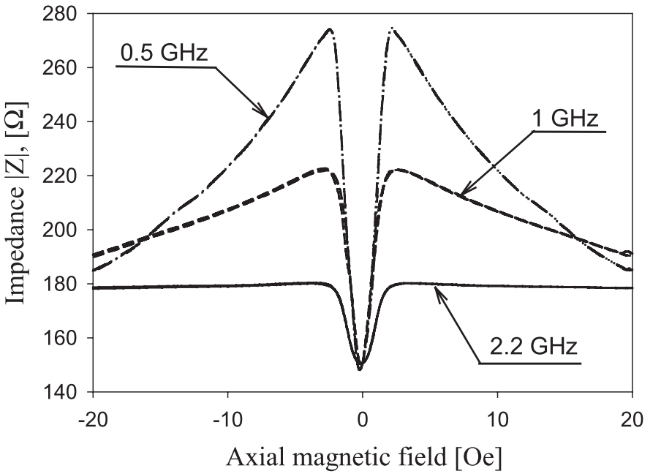

Figure 1.5 – High-frequency impedance plot as a function of a axial external magnetic field. (Extracted from [20]).

positive large magnetostriction constant reinforces the shape anisotropy giving rise to a strong uniaxial anisotropy. This strong anisotropy results in a Natural Ferromagnetic Resonance (NFMR), namely, FMR in the absence of applied magnetic field. Examples of Fe-rich wires featuring NFMR in the GHz frequency range can be found in [5,31]. In other words, ferromangetic wires with positive and large magnetostriction constants operate as permanent magnets in GHz frequency range. In this manner, it is possible to avoid the use of bulky electromagnets to polarize the wires.

1.2 State-of-the-Art: Ferromagnetic Wires in Microwave Engineering

Technological applications of ferromagnetic wires have been traditionally related to the field of sensing devices in the low-frequency range (up to MHz). For example, magnetoimpedance (MI) based sensors in which the ferromagnetic wire is integrated in an electronic circuit have been popular for applications not only including very sensitive magnetic field sensors [6], but also mechanical stress, temperature, position, chemical and multi-functional sensors [32]. Over the last few years, interesting properties such as the MI and FMR effects have suggested the use of ferromagnetic wires in microwave engineering [1].

To begin with, since the MI effect is present at the GHz frequency range, the scattering by a single ferromagnetic wire and/or the response of a composite made of ferromagnetic wires can be tuned through the action of the external magnetic fields. This effect has been theoretically investigated in [33, 34], and it could be exploited in all sort of **reconfigurable devices** such as filters, transmission lines, circulators and antennas. In general, state-of-the-art reconfigurable devices based on varactors, PIN diodes and/or MEMS [35] require from the design of complex feeding networks. This difficulty can be overcome with the use of ferromagnetic wires, since the whole system can be tuned with the use of a single coil/electromagnet. Moreover, it has been found that DC currents flowing along the wires enable the tuning of the wire magnetic properties, as if the wire were affected by an effective external DC magnetic field [36, 37]. This effect paves the way for the development of reconfigurable devices based on ferromagnetic wires with a simple, fully integrated mechanism. In this regard, some experimental works have characterized the MI effect at GHz frequencies [37–39], and variations in the reflection/transmission from composites of ferromagnetic wires as a function of a DC magnetic field have been reported in [40, 41]. However, no design for a particular reconfigurable device has been presented yet.

Additionally, the magnetic properties of the wires, and thus the scattering by a ferromagnetic wire, can also be a function of other external magnitudes such as mechanical-stresses, temperature or chemical activity [2]. Since these variations can be retrieved through inverse scattering techniques, ferromagnetic wires enable radar-based **contact-less sensing**. Particular attention has been devoted to mechanical-stress contactless sensors, which could be applicable, for example, in architectural and health monitoring [42]. Specifically, the characterization of the MI effect at GHz frequencies under mechanical stresses has been carried out by integrating the wires in transmission lines, such as microstrip lines [38,39,42], coaxial cables [43,44] and waveguides [45]. However, it is very challenging to apply mechanical stresses within experiments in which both wires ends are connected to a transmission line. Moreover, additional post-processing is required to recover the actual wire impedance from measurements of a wire integrated within a transmission line, which is often neglected. Thus, it can be concluded that a reliable technique to characterize the GHz MI effect under mechanical stresses is yet lacking. Differently, free-space measurements of the variations in the reflection/transmission properties of a composite of wires under mechanical stresses has been reported in [46,47].

While this experimental works can be considered the first in-situ experiments for contact-less sensing, measurements of the wires operating in a realistic, application-oriented, environment have not been presented yet.

Moreover, previous experiments on ferromagnetic wires for self-sensing materials have been focused on Co-rich wires [38,39,42,45–47]. Most probably, this is due to the heritage of low-frequency MI sensors, in which the largest impedance variations are achieved with negative but near-zero magnetostriction constants. However, Fe-rich wires, which have not been investigated yet in this context, could be advantageous in the design of radar-based contact-less sensors. Note that Fe-rich wires feature positive and large magnetostriction constants, which results in a dominant axial magnetization and in the presence of the NFMR at GHz frequencies [3,5]. Therefore, Fe-rich wires are advantageous for high-frequency sensors, since no biasing field is required to produce the FMR. Even in the presence of a biasing field, Fe-rich wires provide a stronger and higher-frequency FMR due to their higher magnetization at saturation, thus leading to higher spatial resolutions and smaller antennas. Moreover, a high magnetostriction constant ensures a strong response to external mechanical stresses.

Ferromagnetic wires are characterized by high magnetic losses at frequencies close to the FMR, as well as high ohmic losses produced by the reduction in conductivity due to its amorphous nature. Therefore, ferromagnetic wires are good candidates for the development of **electromagnetic absorbers**, which are demanded by a wide range of applications including stealth, EMC, biomedical engineering and communication systems. In view of the properties exposed in Section 1.1.2, radar absorbing materials (RAMs) [48] made of diluted ferromagnetic wires could outperform conventional ferrite absorbers in terms of higher self-biasing frequency, weight, profile and chemical resistance. The work of Baranov [49] was probably the first in opening up the possibility of employing ferromagnetic wires to the development of RAMs, which impulsed several publications devoted to the characterization of the absorption properties of these wires [24–30]. In particular, the absorption spectrum of ferromagnetic wires has been investigated in resonant cavities [24–26], microstrip lines [27] and/or coaxial lines [28–30].

Moreover, the absorption performance of composites with diluted short ferromagnetic wires has been presented in [1, 49–51]. These experiments are focused around 10 GHz and demonstrate that composites of ferromagnetic wires reduce the reflection from a ground plane to levels below -10 dB over a few GHz bandwidth, centered at the FMR frequency. The presented absorbers consist either of composites of wires backed by a ground plane or of thin layers of wires placed at a given distance to the ground plane. However, the former composites are thick enough to contain structural resonances, and the latter are typically placed at a $\lambda/4$ distance to the ground plane. Moreover, the length of the wires is usually tailored to excited axial (half-wavelength) resonances along the wires. Therefore, it is still a matter of debate if the magnetic properties of the wires have been exploited in this previous experimental studies. In addition, a fair comparison between ferromagnetic wire-based and state-of-the-art absorbers has not been presented yet.

Wires featuring FMR effect have also triggered the research on the design of **metamaterials**. Note that the permeability of the wires is negative at frequencies above the FMR [22, 23]. In addition, a negative effective permittivity is to be expected due to the plasma-like response of wire media. Thus, ferromagnetic wires can be considered strong candidates for the development of double-negative (DNG) media (in the sense of an artificial electromagnetic material simultaneously featuring negative permittivity and permeability). The advantages of using ferromagnetic wires are twofold: the use of a single particle to design both permittivity and permeability, and the aforementioned reconfigurable capabilities.

In this regard, previous experimental studies carried out in a joint effort between the Antenna Group and the Physics Department of the Public University of Navarra [31] (and also at other institutions [36, 52, 53]) have reported transmission windows in arrays of ferromagnetic wires, which, following a similar thought process than that of D.R. Smith's seminal paper [54], were identified as an evidence of double negative (DNG) metamaterials. However, the conclusion extracted from the experimental data is controversial since the filling factor of the measured arrays of wires is too small to have a significant effective permeability. For example, theoretical studies considering DNG media based on other kinds of ferromagnetic wires make use of non-conductive, significantly thicker wires [55–57]. Therefore, there is a need of a theoretical basis to understand the origin of the observed transmission windows, and, in general, to analyze the potential of this class of ferromagnetic wires for metamaterial design.

1.3 Goal and Motivation of this Work

This dissertation deals with the use of amorphous glass-coated ferromagnetic wires in microwave engineering. As it was anticipated, interesting properties of the wires such as MI and FMR effects have triggered the research on the use of these wires for diverse applications including reconfigurable devices, contact-less sensors, electromagnetic absorbers and metamaterials. Although some efforts have already been made in this direction, it has been also argued that most of these efforts have been experimentally driven, and that they are mostly focused on characterizing the properties of single wires and/or the reflection/transmission properties of composites of ferromagnetic wires. Therefore, it can be concluded that there is a lack of the modeling tools required to confront the challenges inherent to the design of ferromagnetic wire-based systems. Moreover, it has also been commented that some of the conclusions extracted from those experimental works have been controversial, e.g., those related to electromagnetic absorbers and metamaterial design. Thus, there is also a need of theoretical tools to shed more light into those experiments.

Therefore, the first and foremost objective of this work is to develop modeling tools, e.g., equivalent and approximate circuit models, for the design of microwave systems based on ferromagnetic wires. Furthermore, those models are employed to investigate the main phenomena excited in the scattering by ferromagnetic wires, for example, the transition from surface to bulk effects, and the multiple peculiarities of their absorption spectrum. Based on these fundamental studies, the models developed along this dissertation will also serve to clarify some of the aforementioned controversies concerning electromagnetic absorbers and metamaterials. Moreover, circuit models will prove advantageous to investigate the main potentialities and limitations of ferromagnetic wires, to identify the most promising applications, and to derive simple design rules.

To finalize, this dissertation also contributes to the experimental efforts in the field. In particular, and responding to some of the aforementioned demands in the development of contact-less sensors, a technique aimed to characterize the MI effect at GHz frequencies under mechanical stresses is presented, and the magnetostrictive behavior of Fe-rich wires at GHz frequencies is experimentally investigated for the first time.

1.4 Structure of the document

The document is divided in the following sections:

Chapter 1

The present chapter explains the background, goal and motivation of this work. Moreover, it also introduces basic concepts concerning amorphous glass-coated ferromagnetic wires, their fabrication and properties.

Chapter 2

The second chapter gathers the analytical methods through which ferromagnetic wires are modeled along the dissertation. Approximate and equivalent circuit models are formulated to enable an intuitive interpretation of the interaction between ferromagnetic wires and electromagnetic fields. Furthermore, the experimental and numerical validation of the models is also included.

Chapter 3

Based on the models developed in Chapter 2, this chapter introduces a detailed analysis of the influence of the wire geometry in the scattering by ferromagnetic wires. Particular attention is devoted to the transition from surface to bulk effects. Moreover, a comprehensive analysis of the absorption spectrum of long and short ferromagnetic wires is included.

Chapter 4

Some of the fundamental limits in the scattering by ferromagnetic wires are elucidated in this chapter. In particular, the chapter deals with the correlation of scattering and absorption processes, and how it leads to upper bounds in the absorbed, extracted and scattered powers.

Chapter 5

Chapter 5 is focused on the modeling of ensembles of wires as artificial electromagnetic materials. The homogenization approach is derived based on previous works on wire media, and this formulation is employed to shed some light into previous experiments focused on the development of metamaterials based on ferromagnetic wires. Finally, the validity of the homogenization approach is numerically assessed.

Chapter 6

Artificial impedance surfaces and reconfigurable absorbers based on grids of ferromagnetic wires are investigated in Chapter 6. A closed form expression for the load required to excite a resonance in a grid of wires placed in the proximity of a ground plane is derived. Furthermore, a feasibility study of the implementation of such a load with ferromagnetic wires and other alternative implementations is presented. Moreover, the chapter includes two proof-of-concept designs of reconfigurable absorbers based on resistive sheets made of ferromagnetic wires.

Chapter 7

This chapter addresses the use of ferromagnetic wires in contact-less sensing. To this end, a procedure to characterize the wire distributed impedance under mechanical stresses is introduced, and the magnetostrictive effect of Fe-rich wires is evaluated by using such procedure. Moreover, the performance of such wires as contact-less sensors based on single-wire and material-oriented systems is estimated.

Chapter 8

This chapter offers a brief summary of the results presented in this dissertation, together with some final conclusions and future work lines.

Chapter 2

Analytical Modeling of the Scattering by Ferromagnetic Wires

2.1 Introduction

Analytical models are of the utmost importance in applied electromagnetics and microwave engineering. Even though most systems are described through well-established classical electrodynamics, the equations governing them are so complex that in practice they are typically solved numerically, and it is a cumbersome task to extract any physical insight. Therefore, analytical models are essential to provide the physical understanding required to inspire new ideas and boost innovative engineering concepts.

Following this philosophy, while the response of a ferromagnetic wire to electromagnetic fields has been rigorously studied, most remarkably on L. Kraus's seminal paper [58], this chapter intends to formulate analytical models that help understanding the interaction between electromagnetic fields and ferromagnetic wires. Thus, this chapter gathers the methods through which the ferromagnetic wires will be modeled along the dissertation, including equivalent and approximate models, as well as the experimental and numerical validation of such models.

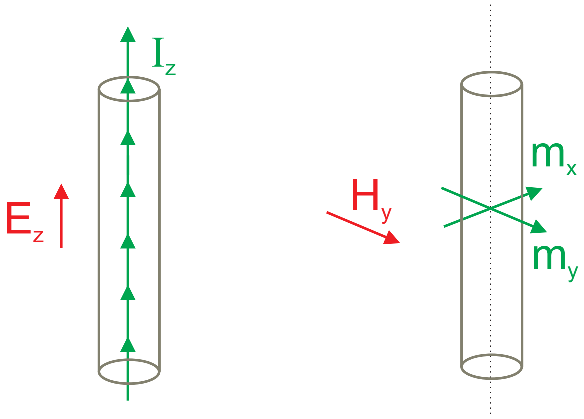

Figure 2.1 – Sketch of the first order excitations in a ferromagnetic wire: magnetoimpedance effect and magnetic dipolar excitation.

2.2 Preliminary Description

Let us have an intuitive look at the properties of a ferromagnetic wire prior to the formulation of any mathematical model. Geometrically, the wires have cylindrical shapes with circular cross-sections of the order of microns, and lengths as long as hundreds of meters (though the wires can be cut to smaller, more practical, lengths). Since $1\,\mu\text{m} = 1/3 \cdot 10^{-4}\lambda$ at 10 GHz, it can be fairly assumed that, within the GHz frequency range, the wires are electrically thin structures.

Electromagnetically, the wires are relatively good conductors ($\sigma \sim 10^5\,\text{S/m}$) and have one or several magnetization domains. Therefore, whenever an electromagnetic field illuminates a ferromagnetic wire one should expect the excitation of conduction currents and magnetic dipoles. Furthermore, the current circulating parallel to the wire axis should be dominant, due to the small cross-sections of the wires, and any current perpendicular to the wire axis could in principle be neglected. Moreover, the wire axis is the preferred direction for the magnetization, and thus the magnetic dipolar excitation is mostly contained within the plane perpendicular to the wire axis. These two elementary effects are depicted in Fig. 2.1. Therefore, it can be concluded that the ferromagnetic wire mainly responds to electromagnetic fields with the electric field polarized along the wire axis, and any other incident polarization can in principle be neglected.

Interestingly, the electric current flowing along the wire is not uniquely defined by the wire conductivity, but it is also a function of its magnetic properties. This effect is usually labelled as the *magnetoimpedance (MI)* *effect*, and it enables to tune the electric response of the wire by modifying its magnetic properties. Similarly, the excitation of magnetic dipoles is affected by the wire conductivity. Unfortunately, this effect results into the presence of eddy current losses, which weakens the magnetic dipolar excitation. As a matter of fact, due to the small cross-sections of the wires and eddy current losses, the excitation of magnetic dipoles is a secondary effect in most conductive wires.

2.3 Scattering by Long Ferromagnetic Wires

2.3.1 Mathematical Solution to the Scattering Problem

2.3.1.1 General Solution

Fig. 2.2 depicts a sketch of a generic scattering problem. From a mathematical standpoint, the electromagnetic fields can be written as the sum of incident (i.e., the field produced by the sources illuminating the wire, the field in the absence of the wire) and scattered (i.e., the field produced by the wires in response to the incident electromagnetic field) fields, i.e.,

$$\mathbf{E} = \mathbf{E}^i + \mathbf{E}^s \tag{2.1}$$

$$\mathbf{H} = \mathbf{H}^i + \mathbf{H}^s \tag{2.2}$$

Furthermore, the wire geometry (elongated shape and circular section) suggests the description of the fields as a basis of cylindrical harmonics [59]. In general, the cylindrical harmonic decomposition includes variations of the field in the r, ϕ and z directions. However, theoretical treatments of ferromagnetic wires usually assume invariance of the fields along the wire axis (the z-axis) [17, 58], reducing the problem to a 2D problem (see Fig. 2.2). By doing so, the incident and scattered electromagnetic fields *outside the wire* can be written as [59]

$$\mathbf{E}^i = \sum_{n=-\infty}^{\infty} e^{-jn\phi} \left[\widehat{\mathbf{z}} A_n^{TM} J_n\left(k_0 r\right) - A_n^{TE} \left(\widehat{\boldsymbol{\phi}} J'_n\left(k_0 r\right) - \widehat{\mathbf{r}} jn \frac{J_n\left(k_0 r\right)}{k_0 r} \right) \right] \tag{2.3}$$

$$\mathbf{H}^i = -\frac{j}{\eta_0} \sum_{n=-\infty}^{\infty} e^{-jn\phi} \left[\widehat{\mathbf{z}} A_n^{TE} J_n\left(k_0 r\right) + A_n^{TM} \left(\widehat{\boldsymbol{\phi}} J'_n\left(k_0 r\right) - \widehat{\mathbf{r}} jn \frac{J_n\left(k_0 r\right)}{k_0 r} \right) \right] \tag{2.4}$$

$$\mathbf{E}^s = \sum_{n=-\infty}^{\infty} e^{-jn\phi} \left[\widehat{\mathbf{z}} B_n^{TM} H_n^{(2)}(k_0 r) - B_n^{TE} \left(\widehat{\boldsymbol{\phi}} H_n^{(2)\prime}(k_0 r) - \widehat{\mathbf{r}} jn \frac{H_n^{(2)}(k_0 r)}{k_0 r} \right) \right] \tag{2.5}$$

$$\mathbf{H}^s = -\frac{j}{\eta_0} \sum_{n=-\infty}^{\infty} e^{-jn\phi} \left[\widehat{\mathbf{z}} B_n^{TE} H_n^{(2)}(k_0 r) + B_n^{TM} \left(\widehat{\boldsymbol{\phi}} H_n^{(2)\prime}(k_0 r) - \widehat{\mathbf{r}} jn \frac{H_n^{(2)}(k_0 r)}{k_0 r} \right) \right] \tag{2.6}$$

where $J_n(-)$ stands for the Bessel function of the first kind and order n, and $H_n^{(2)}(-)$ for the Hankel function of the second kind and order n. In addition, $k_0 = \omega\sqrt{\mu_0\varepsilon_0}$ and $\eta_0 = \sqrt{\mu_0/\varepsilon_0}$ stand for the free-space propagation constant and medium impedance, respectively. A_n^{TZ} and B_n^{TZ}, $Z = E, M$, are the incident and scattered field coefficients, respectively, defined with electric field units. The A_n^{TZ} coefficients are defined by the properties of the sources of the incident field, and the B_n^{TZ} coefficients are a function of the geometrical and electromagnetic properties of the wire. In general, the B_n^{TZ} coefficients are found by solving the boundary value problem on the surface of the wire.

Note that the fields within the wire cannot be written without specifying the wire properties, and therefore they will only be written for particular examples. However, quantities of interest such as the absorbed and scattered powers can be determined through the incident and scattered fields, enabling the study of such magnitudes for a generic ferromagnetic wire. To begin with, the absorbed power per unit length (recall that it is a 2D problem), P_{abs}^L, represents the power dissipated within the wire, and

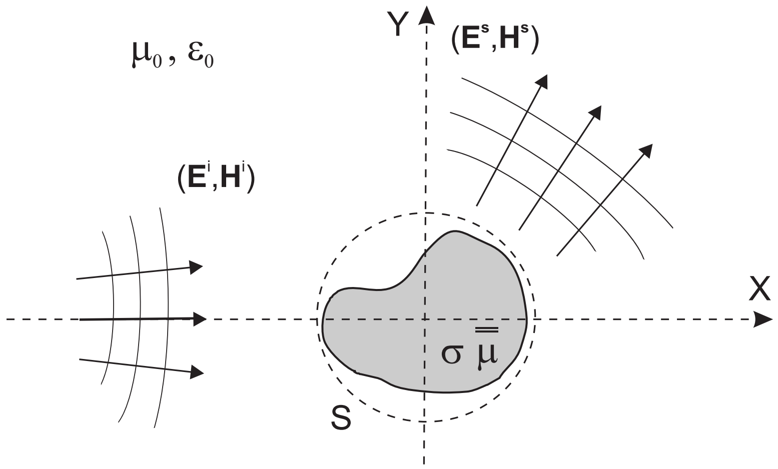

Figure 2.2 – Sketch of the scattering problem: geometry and relevant fields.

it is found as the power entering the scatterer, i.e., the surface integral of the (inward) Poynting vector

$$P^L_{\text{abs}} = -\frac{1}{2} \oiint_S \text{Re}\,\left[\mathbf{E} \times (\mathbf{H})^*\right] \cdot \hat{\mathbf{n}}\, dS \tag{2.7}$$

Similarly, the scattered power (per unit length) represents the power carried away from the scattering object by the scattered field, i.e., the surface integral of the Poynting vector of the scattered field

$$P^L_{\text{scat}} = \frac{1}{2} \oiint_S \text{Re}\,\left[\mathbf{E}^s \times (\mathbf{H}^s)^*\right] \cdot \hat{\mathbf{n}}\, dS \tag{2.8}$$

Due to the orthogonality of cylindrical harmonics [59]

$$\int_0^{2\pi} e^{-j(n-m)\phi} d\phi = 2\pi\delta_{nm} \tag{2.9}$$

a total power quantity is equal to the sum of the same power quantity associated with each mode. Moreover, making use of the Wronskian [59]

$$J_n\left(k_0 r\right) Y_n'\left(k_0 r\right) - J_n'\left(k_0 r\right) Y_n\left(k_0 r\right) = \frac{2}{\pi k_0 r} \tag{2.10}$$

the following properties of Bessel and Hankel functions can be derived

$$\text{Re}\left[-jH_n^{(2)}\left(k_0 r\right)\left(H_n^{(2)\prime}\left(k_0 r\right)\right)^*\right] = \frac{2}{\pi k_0 r} \tag{2.11}$$

and

$$\begin{aligned} &\text{Re}\left[C_1 J_n\left(k_0 r\right)\left(-jC_2 H_n^{(2)\prime}\left(k_0 r\right)\right)^*\right. \\ &\left.+C_2 H_n^{(2)}\left(k_0 r\right)\left(-jC_1 J_n'\left(k_0 r\right)\right)^*\right] = -\text{Re}\left[C_1\left(C_2\right)^*\right]\frac{2}{\pi k_0 r} \end{aligned} \tag{2.12}$$

Making use of the orthogonality of cylindrical harmonics (2.9), and the Bessel function properties (2.11)-(2.12), the quantities: P^L_{abs}, P^L_{scat}, can be rewritten explicitly as the multipole sums:

$$P^L_{\text{abs}} = -\frac{2}{\eta_0 k_0} \sum_{n=-\infty}^{\infty} \sum_{Z=E,M} \text{Re}\left[\left(A_n^{TZ}\right)^* B_n^{TZ}\right] + \left|B_n^{TZ}\right|^2 \tag{2.13}$$

$$P^L_{\text{scat}} = \frac{2}{\eta_0 k_0} \sum_{n=-\infty}^{\infty} \sum_{Z=E,M} \left|B_n^{TZ}\right|^2 \tag{2.14}$$

2.3.1.2 Solution for Static and Uniform Axial Magnetizations

In the most general case, the ferromagnetic core of the wire is composed by multiple magnetization domains whose magnetization tensor and geometry dynamically change in reaction to electromagnetic fields. Despite such complexity, many technologically interesting cases can be modeled by a simpler single and static axial magnetization domain. Specifically, this model is potentially applicable in the GHz range to microwires saturated by an external DC magnetic field, Fe-rich ferromagnetic microwires featuring NFMR [3, 5], and ferromagnetic nanowires fabricated through the Taylor-Ulitovski technique [10, 11]. Therefore, this particular case is studied in detail.

Electric and Magnetic Properties

Under the assumption of a single static magnetization domain along the wire axis, the wire ferromagnetic core can be treated as a linear homogeneous material. On the one hand, the electrical response is dominated by its electrical conductivity that, for the purposes of determining the $(\mathbf{E}, \mathbf{H})$ electromagnetic fields, is equivalent to a wire permittivity [22]:

$$\varepsilon_{\mathrm{w}} = \varepsilon_0 - j\frac{\sigma}{\omega} \tag{2.15}$$

On the other hand, the magnetic response can be modeled as a gyrotropic permeability tensor. In particular, the permeability tensor for a magnetization domain oriented along the wire axis (Z-axis) is given by [22]

$$\bar{\bar{\mu}} = \begin{bmatrix} \mu & j\mu_t & 0 \\ -j\mu_t & \mu & 0 \\ 0 & 0 & \mu_0 \end{bmatrix} \tag{2.16}$$

where

$$\mu = \mu_0 \frac{\omega_H^{\mathbb{C}}\left(\omega_H^{\mathbb{C}} + \omega_M\right) - \omega^2}{\left(\omega_H^{\mathbb{C}}\right)^2 - \omega^2} \tag{2.17}$$

$$\mu_t = \mu_0 \frac{\omega_M \omega}{\left(\omega_H^{\mathbb{C}}\right)^2 - \omega^2} \tag{2.18}$$

where $\omega_M = \mu_0 \gamma M_s$ is the resonance frequency at the saturation limit, with γ being the gyromagnetic ratio, M_s the saturation magnetization. $\omega_H^{\mathbb{C}} = \omega_H + j\alpha\omega$ is the complex Larmor resonance frequency, with $\omega_H =$

$\mu_0 \gamma H_{\text{eff}}$ and α being the dimensionless Gilbert damping constant that takes into account magnetic losses. H_{eff} is an effective magnetic field that gathers any external DC magnetic field, magnetic fields produced by DC currents flowing along the wire and the anisotropy field.

When electromagnetic fields propagate in such media there are two different responses depending on the wave polarization. Firstly, if the magnetic field is polarized parallel to the wire magnetization (i.e. Z-axis), the field is unaffected by the magnetization of the medium, as it can be inferred from (2.16). Secondly, if the magnetic field is transverse to such axis, it is affected by the magnetization leading to the so-called extraordinary waves [22], characterized by a component of the magnetic field in the direction of propagation. In such a case, the propagation within the wire is governed by propagation constant, k_{w}, and medium impedance η_{w}, given by [22]

$$k_{\text{w}}^2 = \omega^2 \varepsilon_{\text{w}} \mu_{\text{w}} \tag{2.19}$$

$$\eta_{\text{w}}^2 = \frac{\mu_{\text{w}}}{\varepsilon_{\text{w}}} \tag{2.20}$$

where μ_{w} is the wire effective scalar permeability for the purposes of propagation, given by

$$\mu_{\text{w}} = \frac{\mu^2 - \mu_t^2}{\mu} = \mu_0 \frac{\left(\omega_H^{\mathbb{C}} + \omega_M\right)^2 - \omega^2}{\omega_H^{\mathbb{C}} \left(\omega_H^{\mathbb{C}} + \omega_M\right) - \omega^2} \tag{2.21}$$

It is apparent from (2.21) that for small damping μ_{w} presents a pole and a zero approximately at the resonant and antiresonant frequencies

$$\omega_{\text{res}} \simeq \sqrt{\omega_H \left(\omega_H + \omega_M\right)} \tag{2.22}$$

$$\omega_{\text{ares}} \simeq \omega_H + \omega_M \tag{2.23}$$

This resonant behaviour is evidenced in Fig. 2.3, which depicts the effective scalar permeability, propagation constant and medium impedance within a ferromagnetic wire with typical values [24, 52, 53] $\sigma = 1.5 \cdot 10^5\,\text{S/m}$, $\mu_0 M_s = 0.55\,\text{T}$, $\alpha = 0.02$, $\gamma = 2 \cdot 10^{11}\,\text{T}^{-1} s^{-1}$ and $H_{\text{eff}} = 123\,\text{kA/m}$. For such material parameters, resonance and antiresonance appear approximately at 10.5 GHz and 22.5 GHz, respectively. It can be concluded that magnetic losses are maximized at the resonance, and that the real part of the effective permeability is negative between resonant and

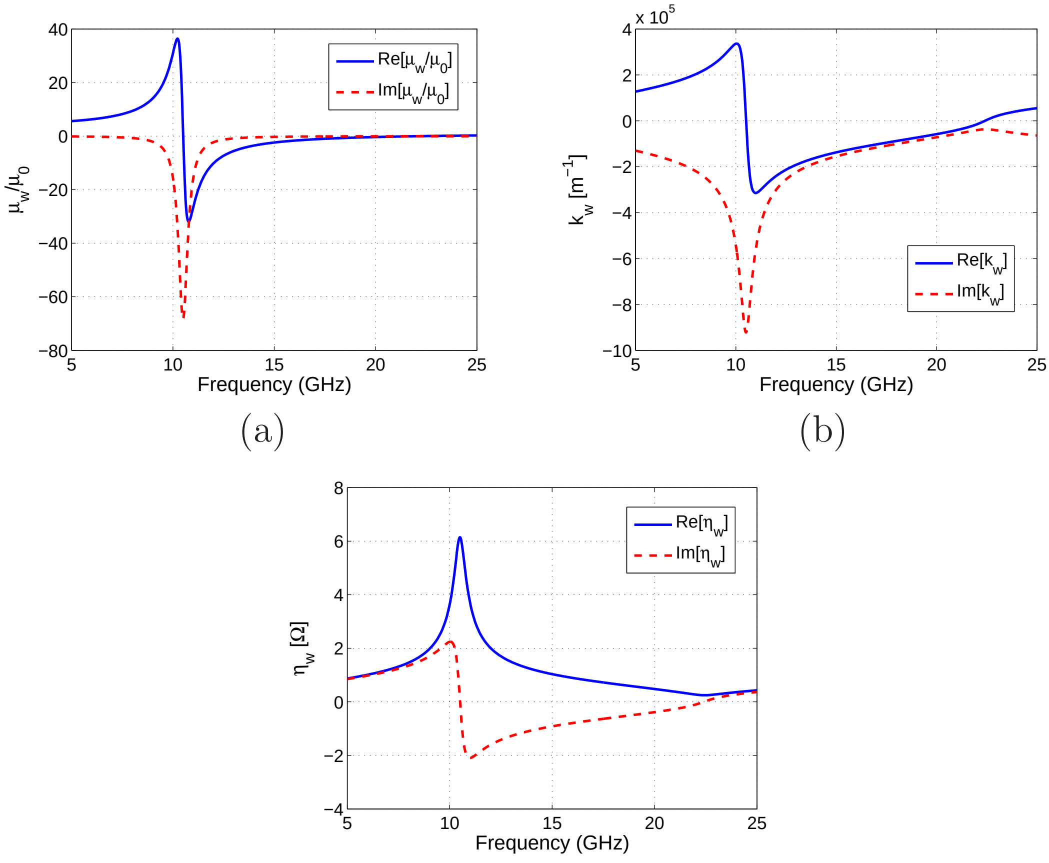

(a) (b)

(c)

Figure 2.3 – (a) Effective scalar permeability (b) propagation constant and (c) medium impedance within a ferromagnetic wire characterized by typical Co-rich values

antiresonant frequencies. Despite the fact that the real part of the permittivity has been neglected due to the dominant role of the conductivity, the sign of the propagation constant between resonance and antiresonance frequencies is negative, since the condition [60] $\mu'_{\rm w}\varepsilon''_{\rm w} + \mu''_{\rm w}\varepsilon'_{\rm w} < 0$ holds due to the large electric losses produced by conductivity.

Scattering by Ferromagnetic Wires with Static and Uniform Magnetization

Consider the case when a plane wave propagating along the X-axis and with the electric field polarized along the Z-axis impinges on a ferromagnetic wire with its axis oriented along the Z-axis. Mathematically speaking, the analytical solution to the scattering of a plane-wave by a ferromagnetic wire with uniform and static magnetization resembles the scattering by a very thin ferrite post, studied in [61]. Following Section 2.3.1, all the fields involved in the scattering problem can be written in terms of cylindrical harmonics. To begin with, the components of the incident plane-wave propagating along the X-axis are written in terms of cylindrical harmonics as [62]

$$E_z^i(r,\phi) = E_0 \sum_{n=-\infty}^{\infty} j^n J_n(k_0 r) e^{-jn\phi} \tag{2.24}$$

$$H_r^i(r,\phi) = \frac{E_0}{\eta_0} \sum_{n=-\infty}^{\infty} n j^n \frac{J_n(k_0 r)}{k_0 r} e^{-jn\phi} \tag{2.25}$$

$$H_\phi^i(r,\phi) = -j\frac{E_0}{\eta_0} \sum_{n=-\infty}^{\infty} j^n J_n'(k_0 r) e^{-jn\phi} \tag{2.26}$$

In other words, the incident field coefficients are given by $A_n^{TM} = j^n E_0$ and $A_n^{TE} = 0$. Similarly, the components of the scattered field are chosen to represent outgoing waves. In addition, due to the cylindrical symmetry of the wire each mode interacts independently, so that the scattered field coefficients are proportional to the source coefficients $B_n^{TM} = b_n^{TM} A_n^{TM}$, and the scattered field is written as

$$E_z^s(r,\phi) = E_0 \sum_{n=-\infty}^{\infty} j^n b_n^{TM} H_n^{(2)}(k_0 r) e^{-jn\phi} \tag{2.27}$$

$$H_r^s(r,\phi) = \frac{E_0}{\eta_0} \sum_{n=-\infty}^{\infty} n j^n b_n^{TM} \frac{H_n^{(2)}(k_0 r)}{k_0 r} e^{-jn\phi} \tag{2.28}$$

$$H_\phi^s(r,\phi) = -j\frac{E_0}{\eta_0} \sum_{n=-\infty}^{\infty} j^n b_n^{TM} H_n^{(2)'}(k_0 r) e^{-jn\phi} \tag{2.29}$$

Finally, the internal field within the wire is represented by Bessel functions of the first kind

$$E_z^{int}(r,\phi) = E_0 \sum_{n=-\infty}^{\infty} j^n c_n^{TM} J_n(k_\mathrm{w} r) e^{-jn\phi} \tag{2.30}$$

$$H_r^{int}(r,\phi) = \frac{E_0}{\eta_\mathrm{w}} \sum_{n=-\infty}^{\infty} j^n c_n^{TM} \left[n\frac{J_n(k_\mathrm{w} r)}{k_\mathrm{w} r} - \frac{\mu_t}{\mu} J_n'(k_\mathrm{w} r) \right] e^{-jn\phi} \tag{2.31}$$

$$H_\phi^{int}(r,\phi) = -j\frac{E_0}{\eta_{\mathrm{w}}}\sum_{n=-\infty}^{\infty} j^n c_n^{TM}\left[J_n'(k_{\mathrm{w}}r) - n\frac{\mu_t}{\mu}\frac{J_n(k_{\mathrm{w}}r)}{k_{\mathrm{w}}r}\right]e^{-jn\phi} \tag{2.32}$$

The unknowns of the problem are the coefficients of the scattered and within the wire fields, which can be found by solving the boundary conditions, i.e. the continuity of the tangential electric and magnetic fields at the surface of the wire, leading to [61]

$$b_n^{TM} = \frac{J_n'(k_0a)J_n(k_{\mathrm{w}}a) - D_nJ_n(k_0a)}{D_nH_n^{(2)}(k_0a) - H_n^{(2)\prime}(k_0a)J_n(k_{\mathrm{w}}a)} \tag{2.33}$$

$$c_n^{TM} = \frac{2j}{\pi k_0 a}\frac{1}{D_nH_n^{(2)}(k_0a) - H_n^{(2)\prime}(k_0a)J_n(k_{\mathrm{w}}a)} \tag{2.34}$$

where a is the wire radius and D_n is defined as

$$D_n = \frac{\eta_0}{\eta_{\mathrm{w}}}\left[J_n'(k_{\mathrm{w}}a) - n\frac{\mu_t}{\mu k_{\mathrm{w}}a}J_n(k_{\mathrm{w}}a)\right] \tag{2.35}$$

2.3.2 Equivalent Circuit Model

Equations (2.3)-(2.6) represent a general solution to the scattering problem, provided that it has been reduced to a 2D problem. However, such solution can be excessively complex in many practical cases. Let us assume that the ferromagnetic wire is illuminated by an electromagnetic field that has a non-negligible polarization component along the wire axis. Since the wire is electrically thin (diameters of $10^{-4}\lambda \sim 10^{-5}\lambda$ at GHz frequencies), the main response of the wire is polarized along the wire axis, and the cross-polarization components can be neglected. This simple fact allows us to omit all TE modes. What is more, even within the TM modes, only the first terms of the series are needed to construct an accurate solution. Typically, the $n = 0, \pm 1$ terms are kept for electrically thin wires [58]. However, due to the relatively good conductivity and the extremely thin radius of the wires the bold approximation of keeping only the $n = 0$ term will be adopted. The validity of such approximation will be tested against experiments and full-wave numerical simulations along the dissertation. Therefore, the electric field scattered by a conductive ferromagnetic wire under the thin wire approximation can be simply written as

$$\mathbf{E}^s\big|_{n=0} = \widehat{\mathbf{z}}B_0^{TM}H_0^{(2)}(k_0r) \tag{2.36}$$

Additional insight can be obtained by examining equivalent sources. In particular, the electric field of (2.36) is equivalent to the electric field produced by an electric line source $\widehat{\mathbf{z}}I_{\mathrm{eq}}$, given by [62]

$$\mathbf{E}^{line} = -\widehat{\mathbf{z}}\frac{\eta_0 k_0}{4} I_{\mathrm{eq}} H_0^{(2)}\left(k_0 r\right) \tag{2.37}$$

The magnitude and phase of the equivalent current are a function of both the electric and magnetic properties of the wire, which can be understood again as the magnetoimpedance (MI) effect. However, it is worth remarking that the equivalent current does not necessarily correspond to the physical conduction currents flowing in the wire. In any event, the ferromagnetic wire can therefore be modeled as any structure supporting the same current distribution. For example, the electric field produced by an impedance-loaded perfect electric conductor (PEC) wire is given by [63]

$$\mathbf{E}^{lw} = -\widehat{\mathbf{z}}\frac{\eta_0 k_0}{4}\frac{E_{\mathrm{loc}}}{\alpha_0^{-1} + Z_{\mathrm{w}}} H_0^{(2)}\left(k_0 r\right) \tag{2.38}$$

where

$$\alpha_0^{-1} = \frac{\eta_0 k_0}{4}\left\{1 + j\frac{2}{\pi}\left[\ln\left(\frac{2}{k_0 a}\right) - \gamma\right]\right\} \tag{2.39}$$

is the susceptibility of a PEC wire, E_{loc} is the local field acting on the wire, Z_{w} is the distributed impedance, and $\gamma \simeq 0.5772$ is the Euler constant. It is apparent from (2.36) and (2.38) that fields produced by a ferromagnetic wire are equivalent to those of a PEC wire with an equivalent distributed impedance given by

$$Z_{\mathrm{w}} = -\frac{\eta_0 k_0}{4}\frac{E_{\mathrm{loc}}}{B_0^{TM}} - \alpha_0^{-1} \tag{2.40}$$

In this manner, the analogy with a line source current allow us to describe the scattering problem as the excitation of a line source current, whose magnitude and phase can be found as the equivalent circuit represented on Fig. 2.4. The equivalent circuit corresponds to a voltage source connected to a load. The voltage source describes the incident electric field. The load is composed by the series connection of a generic wire distributed impedance, Z_{w}, describing the physical phenomena taking place within the wire, connected in series to a resistance and inductance, $R_{\mathrm{scat}} + j\omega L = \alpha_0^{-1}$, describing the radiation and stored magnetic energy produced by a electric line source, i.e., the dominant physical phenomena

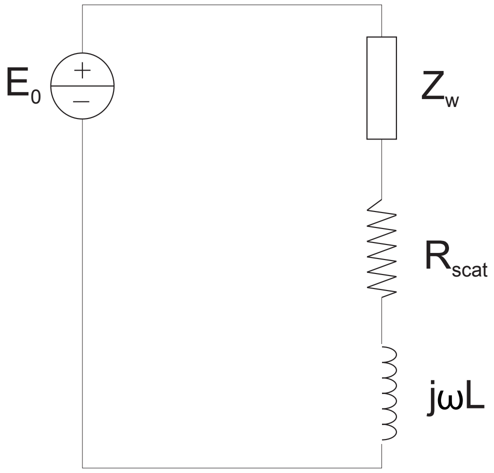

Figure 2.4 – Equivalent circuit model of the scattering by a ferromagnetic wire.

outside the wire. Note that this *equivalent* circuit model is not an approximation, but an exact way to rewrite (2.36) that also helps to elucidate the peculiarities of the scattering by a ferromagnetic wire. As a matter of fact, since the equivalent model constructs the same fields outside the wire than the ferromagnetic wire, any magnitude associated with such external fields can be also determined through the circuit model. For example, (2.7)-(2.8) reveal that absorbed and scattered powers can be computed through the incident and scattered fields. Therefore, it can be readily shown that the absorbed and scattered powers can also be computed in terms of the equivalent circuit model as follows

$$P^L_{\mathrm{abs}} = \frac{1}{2}\mathrm{Re}\left[Z_{\mathrm{w}}\right]\left|I_{\mathrm{eq}}\right|^2 \tag{2.41}$$

$$P^L_{\mathrm{scat}} = \frac{1}{2}R_{\mathrm{scat}}\left|I_{\mathrm{eq}}\right|^2 \tag{2.42}$$

This equivalent circuit model will prove to be a great tool to model ferromagnetic wires. The advantages of the model are twofold: Firstly, it provides an intuitive vision on the way in which the scattering process is modulated by the magnetic properties of the wire. Secondly, all the complexity of the wire magnetization is compiled into the distributed impedance, Z_{w}. This macroscopic parameter can be embedded in the design of systems based on ferromagnetic wires. By doing so, numerical simulations of system composed by wires extending through several wavelengths do not need to resolve details of the order of $10^{-4}\lambda \sim 10^{-5}\lambda$. Furthermore, if Z_{w} can be experimentally retrieved, as it is made in Chapter 7, there is no need for a detailed description of the micro and nano details of the internal magnetization domains to predict the response of the wire to external electromagnetic fields.

2.3.3 Experimental Validation of the Model

Even if the models have been derived based on a solid theoretical background and well-funded approximations, it is always convenient to test them against measurements. The experimental data should ratify the validity of both the thin wire and uniform and static magnetization approximations, as well as the overall correctness of the analytical solution.

Unfortunately, measuring the scattering from a micron-sized object in an anechoic chamber in the GHz frequency range is a cumbersome task. However, such difficulty can be overcome by performing the experiment within a closed environment, for example, a metallic rectangular waveguide. This Section introduces the theory behind the scattering by a ferromagnetic wire within a rectangular waveguide, as well as the experimental verification of the theoretical models through such experiment. Later on, the same experiment will be employed to study the absorption spectrum of ferromagnetic wires in Chapter 3, and to characterize the wires in view of their use as contact-less sensors in Chapter 7.

2.3.3.1 Theoretical Analysis of the Experimental Setup

As it happened in Section 2.3.1.2 with free-space scattering, the mathematical solution to the scattering by a ferromagnetic wire within a rectangular waveguide is very similar to that of a ferrite cylinder within the same waveguide. The latter has been thoroughly studied due to its multiple applications in microwave components such as polarizers and circulators [64–66]. In fact, a rigurous solution to this problem was introduced in [66]. Although corrected [67] and commented [68], the approach introduced there is a correct and general solution to the problem. However, such solution is tedious and complex so a different approach will be followed here leading to much simpler, but restricted, solution. Specifically, the solution is restricted to thin wires located in the middle of the waveguide.

Fig. 2.5 depicts the geometry of the problem. The excitation consists of a TE_{10} mode propagating along a metallic rectangular waveguide of height h and width d. A ferromagnetic wire is placed in the middle of it with the conductive core connected to the waveguide walls. Since there

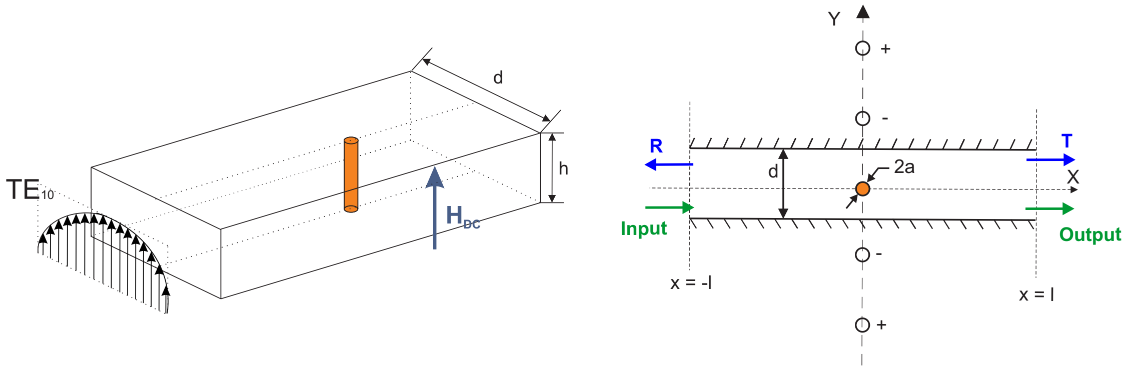

(a) (b)

Figure 2.5 – (a) 3D Sketch and (b) horizontal cut (xy-plane) of the experimental setup: ferromagnetic wire in the middle of a rectangular waveguide.

is no variation of the fields along the Z-axis the problem is reduced to a 2D problem in the XY plane. Therefore, the incident field can be written as [22]

$$\mathbf{E}^i\left(x,y\right)=\widehat{\mathbf{z}}E_0\cos\left(\frac{\pi y}{d}\right)e^{-jk_{\mathrm{wg},x}^{(1)}x} \tag{2.43}$$

where $k_{\mathrm{wg},x}^{(m)}=\sqrt{k_0^2-\left(\frac{m\pi}{d}\right)^2}$ stands for the propagation constant of the TE_{m0} mode. Note that a thin wire located at the origin of coordinates is subjected to uniform illumination, i.e., $\mathbf{E}^i\left(x,y\right)\Big|_{(x,y)\to 0}=\widehat{\mathbf{z}}E_0$. Therefore, the field scattered by the wire within a waveguide is equal to plane-wave scattering plus the addition of the infinite set of alternatively positive and negative images created by the walls of the waveguide (see Fig. 2.5(b)). Thus, the scattered field can be written as

$$\mathbf{E}^s\left(x,y\right)=\widehat{\mathbf{z}}b_0^{TM}E_{\mathrm{loc}}\sum_{n=-\infty}^{\infty}\left(-1\right)^nH_0^{(2)}\left(k_0\sqrt{x^2-\left(y-nd\right)^2}\right) \tag{2.44}$$

As demonstrated in Appendix A, Section A.2.3, the scattered field can be expressed in terms of the waveguide modes by transforming the series of Hankel functions in (2.44) by means of the Poisson summation formula

$$\mathbf{E}^s\left(x,y\right)=\widehat{\mathbf{z}}b_0^{TM}E_{\mathrm{loc}}\frac{4}{d}\sum_{m=1,3\ldots}\cos\left(\frac{m\pi}{d}y\right)\frac{e^{-jk_{\mathrm{wg},x}^{(m)}|x|}}{k_{\mathrm{wg},x}^{(m)}} \tag{2.45}$$

It can be concluded that when the wire is positioned at the center of the waveguide only the TE_{m0} modes with m being an odd number are excited. E_{loc} stands for the local field in the surface of the wire, given by the addition of the incident field and the field generated by the images

$$E_{\mathrm{loc}} = \frac{E_0}{1 - b_0^{TM} G_{\mathrm{int}}^{\mathrm{wg}}} \tag{2.46}$$

where the waveguide interaction parameter G_{wg} has been defined as

$$G_{\mathrm{int}}^{\mathrm{wg}} = \sum_{n \neq 0} (-1)^n \, H_0^{(2)}(k_0 \, |nd|) \tag{2.47}$$

Following Appendix A, Section A.2.4, $G_{\mathrm{int}}^{\mathrm{wg}}$ can be alternatively written as

$$G_{\mathrm{int}}^{\mathrm{wg}} = -1 + j\frac{2}{\pi}\left[\ln\left(\frac{k_0 d}{\pi}\right) + \gamma\right] + j\frac{4}{d} \sum_{m=1,3\ldots} \left(\frac{1}{j k_{\mathrm{wg},x}^{(m)}} - \frac{1}{\frac{\pi m}{d}}\right) \tag{2.48}$$

While (2.47) describes the waveguide-wire interaction as the effect produced by the images of the wire in the lateral metallic planes, (2.48) describes the waveguide-wire interaction in structural terms. For example, $\mathrm{Re}\,[G_{\mathrm{int}}^{\mathrm{wg}}] = -1$ when there are no modes propagating in the waveguide ($k_0 d < \pi$, $k_{\mathrm{wg},x}^{(m)} \epsilon \mathbb{I} \, \forall m$). This fact illustrates how the waveguide-wire interaction cancels out the propagating fields produced by the wire, so that the resultant fields are purely reactive. By contrast, some $k_{\mathrm{wg},x}^{(m)}$ become real for larger $k_0 d$. In such a case, the real part of the interaction constant increases, representing fields propagating away from the wire in the form of waveguide modes.

Once the scattered field is known, it is possible to compute measurable quantities. For example, let us assume that the experimental setup corresponds to the one depicted in Fig. 2.5. Under monomode operation, the measured scattering parameters are given by

$$S_{11} = \left.\frac{E_z^s}{E_z^i}\right|_{x=-l} = \frac{4}{k_{\mathrm{wg},x}^{(1)} d} \frac{1}{\left(b_0^{TM}\right)^{-1} - G_{\mathrm{int}}^{\mathrm{wg}}} e^{-j2k_{\mathrm{wg},x}^{(1)} l} \tag{2.49}$$

$$S_{21} = \left.\frac{E_z^s + E_z^i}{E_z^i}\right|_{x=l} = \left(1 + \frac{4}{k_{\mathrm{wg},x}^{(1)} d} \frac{1}{\left(b_0^{TM}\right)^{-1} - G_{\mathrm{int}}^{\mathrm{wg}}}\right) e^{-j2k_{\mathrm{wg},x}^{(1)} l} \tag{2.50}$$

In addition, the reflection, transmission and absorption power coefficients can be directly computed from the scattering parameters as $R = |S_{11}|^2$, $T = |S_{21}|^2$ and $A = 1 - |S_{11}|^2 - |S_{21}|^2$.

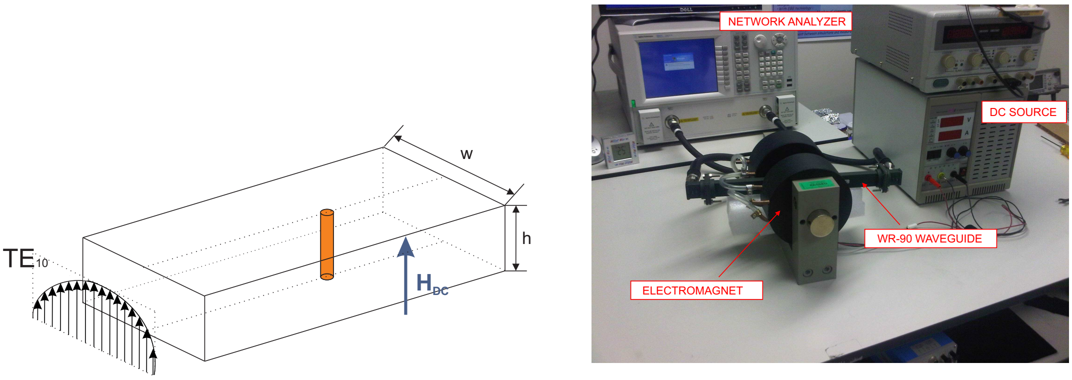

(a) (b)

Figure 2.6 – Sketch and photograph of the experimental setup. The wire is placed in between two WR-90 waveguides with its ends short-circuited to the metallic walls. An electromagnet has been positioned in such way that a DC magnetic field is applied parallel to the wire axis.

2.3.3.2 Experimental Verification of the Analytical Solution

A Co-rich $(\mathrm{Co}_{0.94}\mathrm{Fe}_{0.06})_{75}\mathrm{Si}_{12.5}\mathrm{B}_{12.5}$ ferromagnetic wire with metallic radius of 22.5 μm and mean total diameter (including the Pyrex coating) of 65 μm has been employed to experimentally validate the theoretical analysis. The wire was fabricated by means of the Taylor-Ulitovsky technique [7,8] in collaboration with Prof. M. Vázquez at the Material Science Institute of Madrid (ICMM). The purpose of the experiment is twofold: to check the correctness of the analytical solution, and to assess the validity of the thin wire and uniform and static magnetization approximations.

A sketch and photograph of the experimental setup are presented in Fig. 2.6. The wire is placed between two rectangular metallic WR-90 waveguides, so that when they are connected the wire is short-circuited and behaves as the theoretically studied infinitely long wire. The setup is calibrated at the waveguide ends. Moreover, an electromagnet is employed to apply a DC magnetic field along the wire axis. The frequency range is selected so that monomode operation is ensured, with the TE_{10} waveguide mode as incident high-frequency field. The reflection R, transmission T and absorption A power coefficients can be directly obtained from the measurement of the S-parameters: $R = |S_{11}|^2$, $T = |S_{21}|^2$ and $A = 1 - |S_{11}|^2 - |S_{21}|^2$.

The measurements were carried out at the measurement laboratory of the Antenna Group, Public University of Navarra, by A. Labrador (Physics Department, Public University of Navarra), who provided the

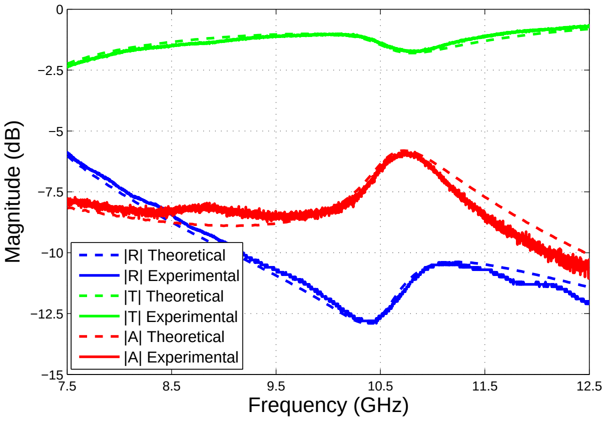

Figure 2.7 – Comparison between theoretical and measured reflection, transmission and absorption power coefficients of a Co-rich ferromagnetic wire within a WR-90 rectangular waveguide.

measured S-parameters. Such measurements were processed to test the analytical model. Specifically, Fig. 2.7 depicts the comparison between theoretical and measured reflection, transmission and absorption power coefficients. It can be concluded that there is an excellent agreement between the theoretical and experimental coefficients. Note that the wire properties were set as $\sigma = 1.5 \cdot 10^5\,\mathrm{S/m}$, $\mu_0 M_s = 0.55\,\mathrm{T}$, $\alpha = 0.02$, $\gamma = 2{\cdot}10^{11}\,\mathrm{T}^{-1}s^{-1}$ and $H_{\mathrm{eff}} = 123\,\mathrm{kA/m}$ to fit the theoretical model to the experimental data, and the adopted values are consistent with empirical values reported in the literature for Co-rich wires [24, 52, 53]. Therefore, this experiments demonstrates that the analytical solution to the problem is correct, and that the thin wire and uniform static approximations are accurate enough to model the scattering by these ferromagnetic wires.

2.4 Scattering by Short Ferromagnetic Wires

Due to the large lengths produced at fabrication, the response of ferromagnetic wires is usually modeled as that of infinitely-long wires. However, size and mechanical constraints impose the use of significantly shorter lengths for many practical applications. In such cases, axial resonances and non-uniform current distributions appear when the wire length is not much larger than the wavelength of operation, adding extra complexity to the scattering problem. This Section formulates integro-differential equations and approximate circuit models to deal with the scattering by a short ferromagnetic wire.

2.4.1 Mathematical Solution to the Scattering Problem

Consider then a ferromagnetic wire of length $2L$ and radius a, as depicted in Fig. 2.8. As usual, the solution to the scattering problem is found by enforcing the boundary conditions on the surface of the wire. In virtue of the Huygens Principle and equivalence theorem [62, 69], the original problem can be transformed to an equivalent one by including electric and magnetic currents on the surface of the wire. In this manner, the total electric field $\mathbf{E}(\mathbf{r}) = \mathbf{E}^i(\mathbf{r}) + \mathbf{E}^s(\mathbf{r})$ can be written as

$$\begin{aligned}\mathbf{E}\left(\mathbf{r}\right) = \mathbf{E}^i\left(\mathbf{r}\right) - \frac{j}{\omega\varepsilon_0}\left[k_0^2 + \nabla\nabla\cdot\right] \iint_S \mathbf{J}_S\left(\mathbf{r}'\right)\frac{e^{-jk_0R}}{4\pi R}dS \\ -\nabla\times\iint_S \mathbf{M}_S\left(\mathbf{r}'\right)\frac{e^{-jk_0R}}{4\pi R}dS\end{aligned} \tag{2.51}$$

where $R = |\mathbf{r} - \mathbf{r}'|$, while $\mathbf{J}_S$ and $\mathbf{M}_S$ are the equivalent electric and magnetic currents, respectively, which are given by

$$\mathbf{J}_S = \hat{\mathbf{n}} \times \mathbf{H} \tag{2.52}$$

$$\mathbf{M}_S = -\hat{\mathbf{n}} \times \mathbf{E} \tag{2.53}$$

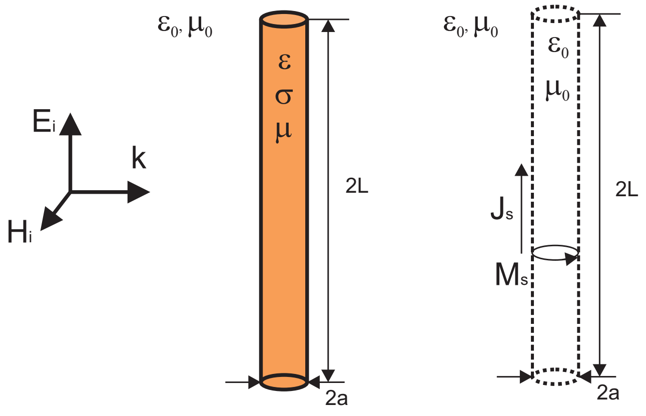

Figure 2.8 – Geometry of the original and equivalent problems of the scattering by a short ferromagnetic wire.

The values of the equivalent surface currents are to be found solving this integro-differential equation on the wire surface. Under the thin wire ($a \ll \lambda$) and high aspect ratio ($a \ll L$) approximations, the contribution coming from the surface magnetic current can be neglected and the surface electric current collapses to an azimuthally uniform current $\mathbf{J}_S(\mathbf{r}') = \widehat{\mathbf{z}} I(z')/\left(2\pi a\right)\delta\left(r' - a\right)$. In addition, the tangential incident field on the wire surface can be considered a constant, $\widehat{\mathbf{z}} \cdot \mathbf{E}^i(\mathbf{r}') = E_0$, whereas the tangential total electric field on the wire surface can be written as the product of the wire surface electric current and the wire distributed impedance $\widehat{\mathbf{z}} \cdot \mathbf{E}(\mathbf{r}') = Z_{\mathrm{w}} I\left(z'\right)$. In this manner, (2.51) on the surface of the wire is reduced to a generalized Pocklington equation

$$\frac{j\eta_0}{2\pi k_0}\left[k_0^2 + \partial_z^2\right]\int_{-L}^{L} I\left(z'\right) G\left(R\right) dz' + Z_{\mathrm{w}} I\left(z\right) = E_0 \tag{2.54}$$

where $G\left(R\right)$ is the exact thin wire kernel equal to

$$G\left(R\right) = \int_{0}^{2\pi} \frac{e^{-jk_0 R}}{4\pi R} d\phi' \tag{2.55}$$

The solution to the integro-differential equation (2.54) provides the surface current, $I\left(z\right)$ as a function of the excitation E_0. Analytical solutions to this equation have been introduced in [69–71]. However, the equation has several solutions and an iterative process is in general needed to achieve the correct value. Despite this, it has been proven that simple numerical methods can be adopted leading to accurate solutions [72]. In this dissertation, (2.54) is solved by using the method of moments following a point matching scheme with a triangular basis functions [73].

Once the surface current $I(z)$ is known, the electric and magnetic fields on the surface of the wires can be easily retrieved. Consequently, the absorbed and scattered powers can also be numerically computed as surface integrals, as in (2.7) and (2.8). However, it is probably simpler and more elegant to invoke again the equivalence principle to compute the absorbed power through the equivalent current distribution

$$P_{\mathrm{abs}} = \frac{1}{2} R_{\mathrm{w}} \int_{-L}^{L} \left|I(z)\right|^2 dz \tag{2.56}$$

and to find the scattered power as the power radiated by a linear distribution of current [74]

$$P_{\text{scat}} = \frac{\eta_0 k_0^2}{(4\pi)^2} \int_0^{2\pi} \int_0^{\pi} \left| \int_{-L}^{L} I\left(z'\right) e^{jk_0 \cos\theta z'} dz' \right|^2 \sin^3\theta dS \tag{2.57}$$

2.4.2 Approximate Circuit Model

While the previous section analysis represents an accurate solution to the scattering problem, it must be solved numerically and can hardly provide much physical insight into the scattering by a short ferromagnetic wire. This section introduces a simple circuit model that, despite being an approximation of the scattering solution, is reasonably accurate, and simple enough to provide physical insight into the interaction of short ferromagnetic wires with electromagnetic waves.

To begin with, the solution to the scattering problem becomes easier if the current distribution on the wire is known. To this end, it can hypothesized that, as with PEC dipole antennas, the current can be approximated by sinusoidal distributions [73]. In particular, the current distribution of a short-circuited receiving PEC dipole antenna is approximately given by

$$I(z) = I_R(0)\, f_R(z) \tag{2.58}$$

with

$$f_R(z) = \frac{\cos(k_0 z) - \cos(k_0 L)}{1 - \cos(k_0 L)} \tag{2.59}$$

Since the current distribution is supposed to be known, the problem is reduced to finding the magnitude of the current, $I_R(0)$. Fortunately, $I_R(0)$ can be easily determined by means of the reciprocity theorem as follows [75]

$$I_R(0) = \frac{V}{Z_{\text{in}} + Z_{\text{w}}^{\text{mod}}} \tag{2.60}$$

where V stands for the electromotive force induced by the incident field, given by

$$V = E_0 \int_{-L}^{L} f_T(z)\, dz \tag{2.61}$$

with $f_T(z)$ being the current distribution function of the reciprocal PEC dipole antenna in the transmitting mode

$$f_T(z) = \frac{\sin(k_0 L - k_0 |z|)}{\sin(k_0 L)} \tag{2.62}$$

In addition, Z_{in} is the self-impedance of the reciprocal transmitting PEC dipole antenna, and $Z_{\mathrm{w}}^{\mathrm{mod}}$ is an impedance term which takes into account the wire surface impedance, Z_{w}. In particular, the finite conductivity and magnetic response of the wire produce a voltage drop $Z_{\mathrm{w}} f_T(z)$ at each dz point of the wire, leading to

$$Z_{\mathrm{w}}^{\mathrm{mod}} = Z_{\mathrm{w}} \int_{-L}^{L} f_T^2\,(z)\,dz \tag{2.63}$$

Once the current on the wire has been determined through the circuit model, the absorbed and scattered powers can again be computed through (2.56) and (2.57), respectively.

It is apparent from (2.60) that the magnitude of the current distribution excited in a short ferromagnetic wire can be analyzed through a similar circuit model than the one developed for a long ferromagnetic wire (see Fig 2.4). To this end, the voltage source must be defined by the electromotive force produced by the incident field (2.61), the wire impedance is given by (2.63), accounting by the distributed effect on the wire surface, and the $R_{\mathrm{scat}} + j\omega L$ load must be substituted by the self-impedance of the reciprocal transmitting antenna Z_{in}, which is mostly capacitive for short wires.

2.4.3 Numerical Validation of the Model

The accuracy of this circuit model relies on the validity of the current distribution. Since the assumed current distributions were those of PEC dipole antennas [73], the circuit model is the more accurate the closer the wires behave as good conductors (i.e. the thicker the wires are). This is emphasized in Fig. 2.9, which depicts the absorbed power predicted by the method of moments and the circuit model for Co-rich wires with 22.5 μm, 5 μm and 2 μm radius and $2L = 9.8$ mm length. While there is almost a perfect match between both models for the thickest wire, the accuracy of the circuit model degrades as the wire radius decreases. Nevertheless, the circuit model provides a qualitative estimation of the absorption spectrum for all considered radii.

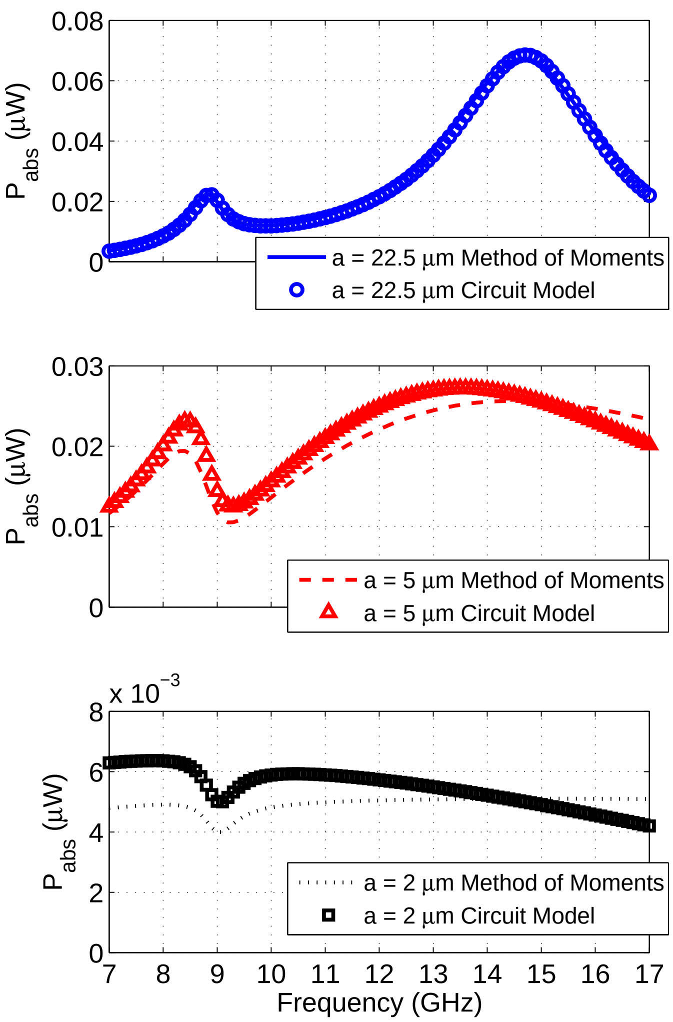

Figure 2.9 – Comparison of the absorption spectrum predicted by the method of moments and circuit model for Co-rich wires with $22.5\,\mu$m, $5\,\mu$m and $2\,\mu$m radius and $2L = 9.8\,$mm length.

2.5 Conclusions

The mathematical methods through which ferromagnetic wires are modeled along the dissertation have been introduced in this chapter. Following previous works, the response of infinitely-long wires has been modeled by means of a decomposition in cylindrical harmonics [17, 58, 61], and the scattering by finite-length wires has been addressed through a generalized Pocklington equation [69–71]. Moreover, equivalent and approximate circuit models have also been formulated. Specifically, it has been found that, within the thin wire approximation, the scattering by an infinitely-long ferromagnetic wire is equivalent to that of an impedance loaded wire, and the scattering by a finite size wire can be approximated by that of a PEC dipole antenna with sinusoidal current distribution, also loaded with a certain distributed impedance. Moreover, such circuit models have been validated experimentally (for infinite-long wires) and numerically (for finite-size wires).

Chapter 3

Surface and Bulk Effects in the Scattering by Ferromagnetic Wires

3.1 Introduction

It has been argued in Chapter 2 that, in the GHz frequency range, ferromagnetic wires are electrically thin structures. Under this perspective, one might conclude that the radius of the wires shall not have a great impact on the response of the wires to electromagnetic fields. In other words, it could be expected that changing the wire radius from $10^{-4}\lambda$ to $10^{-5}\lambda$ should not dramatically affect the scattering by a ferromagnetic wire. It turns out to be just the opposite. As a matter of fact, it has been experimentally found that variations of the wire radius on the order of microns produce dramatic changes on the scattering and absorption by a ferromagnetic wire. For example, Fig 3.1(a) represents the measured absorption power coefficient[1] of three different Co-rich wires of $a = 22.5\,\mu\text{m}$, $a = 5\,\mu\text{m}$ and $a = 2\,\mu\text{m}$ radius, corresponding to electric sizes of $a/\lambda = 7.5 \cdot 10^{-4}$, $a/\lambda = 1.67 \cdot 10^{-4}$ and $a/\lambda = 6.67 \cdot 10^{-5}$ at 10 GHz. Despite the fact that the wires have the same composition and were biased with the same electromagnet, there are significant differences in the absorption spectra.

The reason behind this apparently anomalous behavior is the strong mismatch between the free-space wavelength and the wavelength within

---

[1] The details of the experiment and the interpretation of the absorption spectra are reported later on in the chapter.

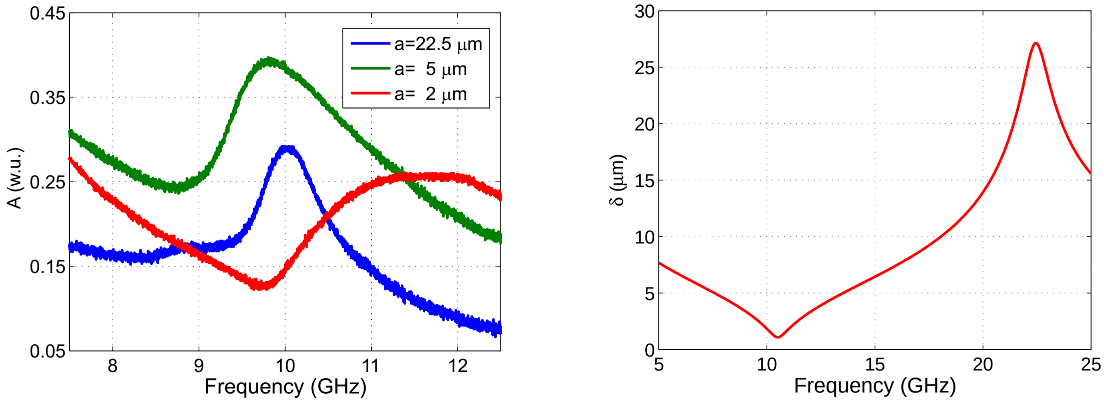

(a) (b)

Figure 3.1 – (a) Measured absorption power coefficient for Co-rich ferromagnetic wires with $a = 22.5\,\mu$m, $a = 5\,\mu$m and $a = 2\,\mu$m radius. (b) Skin-depth as a function of frequency for typical Co-rich ferromagnetic wire parameters.

the wire. As a matter of fact, it can be concluded from Fig. 3.1(b) that the penetration depth ($\delta = 1/k''_{\mathrm{w}}$) is of the order of microns around the resonance, so that the wire radii can be larger than, comparable to, or smaller than the penetration depth. Thus, radius changes of the order of microns produce a transition from surface to bulk effects.

Due to the crucial role of these effects in the scattering by ferromagnetic wires, this chapter will be fully devoted to the study of such effects. Specifically, the equivalent circuit model derived in Section 2.3.2 is employed in Section 3.2 to shed more light into the matter. Moreover, Fig. 3.1(a) exemplifies how the transition from surface to bulk effects hinders the interpretation of the absorption spectrum of ferromagnetic wires. This is highly inconvenient, since an accurate knowledge of the absorption spectrum is required from both technological (e.g., the design of electromagnetic absorbers) and material science (e.g., the determination of the magnetic properties through the frequency position of the FMR) points of view. Therefore, Section 3.3 introduces a detailed analysis of the absorption spectrum of ferromagnetic wires. Since axial resonances and non-uniform current distributions add extra complexity to the absorption spectrum of short wires, both long and short ferromagnetic wires are carefully addressed.

3.2 Analysis of Surface and Bulk Effects by means of Equivalent Circuit Models

Let us use the equivalent circuit model developed in Section 2.3.2 to gain more insight into the surface and bulk effects in the scattering by ferromagnetic wires. To this end, recall that, under the thin wire approximation ($k_0 a \ll 1$), the fields scattered by a ferromagnetic wire are equal to those scattered by an impedance-loaded PEC wire, with equivalent distributed impedance $Z_\mathrm{w} = R_\mathrm{w} + jX_\mathrm{w}$ given by

$$Z_\mathrm{w} = -\frac{\eta_0 k_0}{4}\left(b_0^{TM}\right)^{-1} - \alpha_0^{-1} \tag{3.1}$$

Assuming a single static axial magnetization domain, a closed-form for the distributed impedance can be found by substituting the values of b_0^{TM} given by (2.33) into (3.1). By doing so, Z_w can be written as

$$Z_\mathrm{w} = j\frac{\eta_\mathrm{w}}{2\pi a}\frac{J_0\left(k_\mathrm{w} a\right)}{J_0'\left(k_\mathrm{w} a\right)} \tag{3.2}$$

Intuitively, it can be readily checked that the equivalent impedance is equal to the wire surface impedance divided by the perimeter: $Z_\mathrm{w} = E_z\left(r = a\right) / \left[2\pi a H_\phi\left(r = a\right)\right]$. Furthermore, since Z_w is a function of η_w and k_w it is clear that the wire impedance is not only defined by the electric conductivity, but it is also greatly affected by the wire magnetic properties. In this manner, the magnetoimpadance effect (MI) is also described by the equivalent circuit model.

Due to the great mismatch between free-space and the wavelengths within the wire, it is found that, contrary to $k_0 a$, which always remains small, $k_\mathrm{w} a \ll 1$, $k_\mathrm{w} a \simeq 1$ and $k_\mathrm{w} a \gg 1$ are perfectly possible depending on the ratio between the wire radius and skin depth ($\delta = 1/k_\mathrm{w}''$). Since conductive wires are inherently lossy, the field is constrained to the wire surface for $k_\mathrm{w} a \gg 1$. Thus, such a case will be referred to as the skin-effect (SE) limit. By contrast, the fields are uniform within the wire for $k_\mathrm{w} a \ll 1$, and therefore such scenario will be referred to as the quasi-static (QS) limit.

Let us start with the QS limit. Taking small-argument approximations

$J_0(k_\mathrm{w}a) \simeq 1$ and $J_0'(k_\mathrm{w}a) \simeq -\frac{k_\mathrm{w}a}{2}$, Z_w can be approximately written as

$$Z_\mathrm{w}^{QS} \simeq \frac{1}{\pi a^2 \sigma} \tag{3.3}$$

which is equal to the inverse of the wire cross-section area times conductivity, corresponding to the electrical resistance of the wire. Therefore, in the QS limit Z_w becomes independent of the wire magnetic properties. In such scenario, the electric field inside the wire is uniform and the electric and magnetic responses decouple. This phenomenon is consistent with the fact that the electric field tends to be described by Poisson's equation as the electrostatic limit is approached.

As for the SE effect limit, taking the large (and complex) argument approximation $J_0(x) \simeq -jJ_0'(x)$, Z_w can be approximately written as

$$Z_\mathrm{w}^{SE} \simeq \frac{\eta_\mathrm{w}}{2\pi a} \tag{3.4}$$

It is apparent from (3.4) that Z_w becomes directly proportional to the medium impedance and inversely proportional to the wire perimeter. Since the current is concentrated in a smaller area, Z_w increases as the wire radius decreases. An additional physical interpretation of this fact is as follows: since the electromagnetic fields become more strongly constrained to the wire surface as the radius increases, in the very SE limit there is almost no field inside the wires, and the influence of the wire constitutive parameters tend to vanish, getting closer and closer to the behavior of a PEC wire, i.e., the distributed impedance tends to zero.

Summarizing, in both QS and SE limits the influence of the wire permeability on the zero-order response tends to vanish, and thus the intermediate cases will be the most interesting ones to tailor the response of the wire through its magnetic properties. Therefore, it is apparent that those radii in the transition from surface to bulk effects provide the larger correlation between the electric and magnetic responses of the wire. The regions of validity for the QS and SE limits depend on the geometrical and electromagnetic parameters of the wire, as well as on the frequency of operation.

To further clarify these phenomena, Fig. 3.2 represents the frequency behavior of the wire distributed impedance for wires of $50\,\mu$m, $10\,\mu$m, $1\,\mu$m and 100 nm. The wires have been modeled with typical Co-rich values [53]: conductivity $\sigma = 5 \cdot 10^5\,$S/m, gyromagnetic ratio $\gamma = 2 \cdot 10^{11}\,\mathrm{T}^{-1}\mathrm{s}^{-1}$, saturation magnetization $\mu_0 M_\mathrm{s} = 0.55\,$T, and magnetic loss

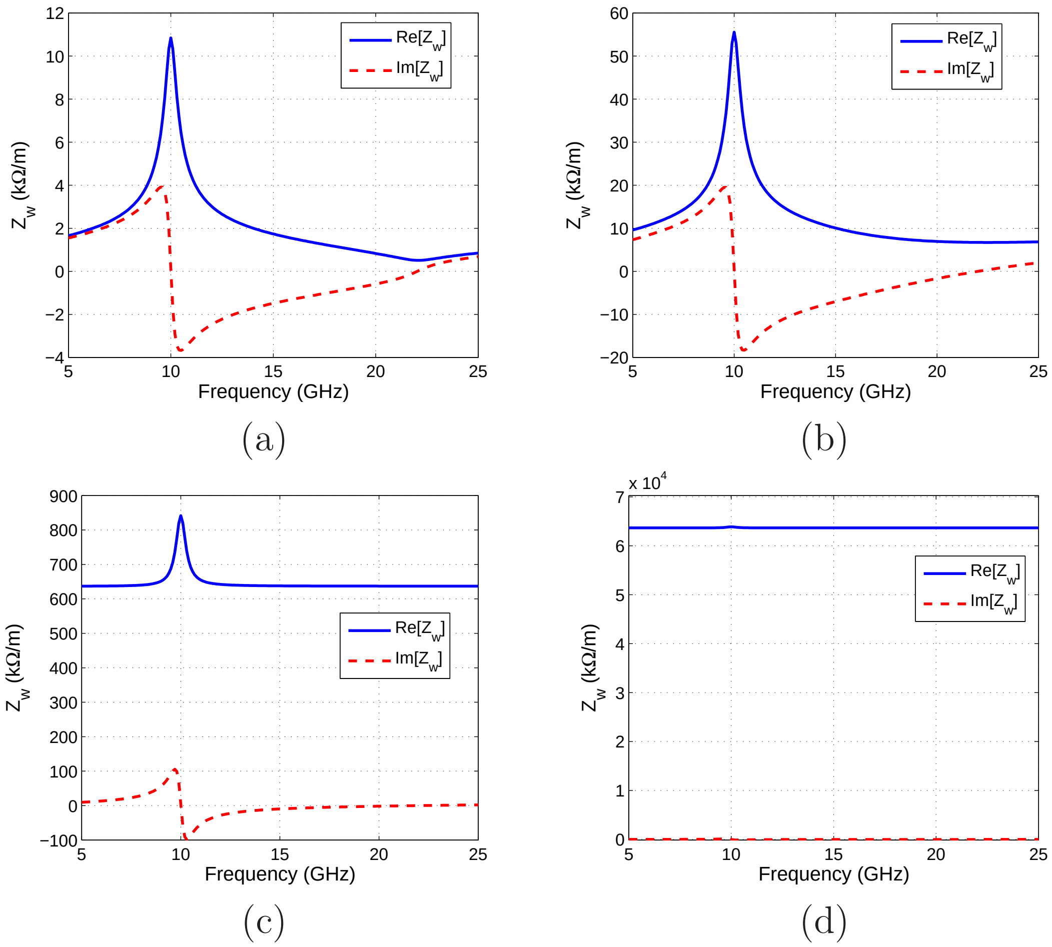

(a) (b)

(c) (d)

Figure 3.2 – Wire distributed impedance for Co-rich ferromagnetic wires of (a) 50 μm, (b) 10 μm, (c) 1 μm and (d) 100 nm radius.

factor $\alpha = 0.02$. An effective DC magnetic field $H_{\text{eff}} = 113.45\,\text{kA/m}$ is assumed, so that the FMR frequency is at 10 GHz and the AFMR frequency is located at approximately 22 GHz.

As it was anticipated, Z_{w} is low and resembles η_{w} in the strong SE limit (see Fig. 3.2(a), $a = 50\,\mu$m), exhibiting a maximum of resistance at the FMR frequency and a minimum at the AFMR frequency. Moreover, the equivalent inductance crosses zero at the FMR and AFMR frequencies, being capacitive between the FMR frequency and the AFMR frequency (corresponding to $\text{Re}[\mu_{\text{w}}] < 0$), and being inductive below the FMR frequency and above the AFMR frequency (corresponding to $\text{Re}[\mu_{\text{w}}] > 0$).

By contrast, the resistance becomes much larger than the reactance as the wire radius gets smaller, so that the similarity of Z_{w} with η_{w} disappears. For example, the impact of the AFMR in the resistance cannot be appreciated for a wire of 10 μm radius (see Fig. 3.2(b)), and the resistance is almost constant except for a peak at the FMR frequency for a radius of $1\,\mu$m (see Fig. 3.2(c)). Note that the penetration depth is minimized at the FMR frequency, and therefore that is the last frequency to converge to the QS regime. Finally, all frequencies converge to the QS limit for the wire of $a = 100\,$nm (see Fig. 3.2(d)). In such a case, the equivalent impedance is real and frequency independent, which confirms that it is also independent on the magnetic properties of the wire.

This simple study allows us to identify some of the main potentialities and limitations of ferromagnetic wires. On the bright side, ferromagnetic wires can play the role of impedance loaded wires in a large number of devices. In fact, Fig. 3.2 demonstrates that they have the potential to provide resistive, inductive and capacitive loading. What is more, all of the aforementioned loads can be tuned by means of external DC magnetic fields, DC currents or mechanical stresses. Thus, no complex feeding networks are required in reconfigurable devices based on ferromagnetic wires. On the downside, ferromagnetic wires are very lossy. In fact, it can be concluded from Fig. 3.2 that the resistance is always superior to the reactance, and this effect is the more dramatic the smaller the wire radius. In other words, the larger the reactive loading obtained from the wires, the larger the resistance to reactance ratio. This simple fact limits the scope of ferromagnetic wires in a number of reconfigurable devices where efficiency is critical. Therefore, the following chapters of the dissertation will emphasize the design of absorbers and sensors, where, in principle, losses are not a drawback. The physical principle behind this limitation is that, as the reactive loading is produced by magnetic domains within a conductive core, any reactive loading is accompanied by large ohmic losses. Therefore, the limitations imposed by losses could be overcome by heterogeneous structures with separated non-magnetic conductive regions and non-conductive magnetic regions. Unfortunately, the latter have not been fabricated by means of the Taylor-Ulitovsky technique yet.

3.3 On the Absorption Spectrum of Ferromagnetic Wires

3.3.1 Absorption Spectrum of Long Wires

3.3.1.1 Theoretical Analysis

The equivalent circuit model will also provide us with an intuitive explanation for the absorption spectra depicted in Fig. 3.1(a). To begin with, recall that the absorbed power can be written in circuital terms as (see equation (2.41))

$$P_{\text{abs}}^{L} = \frac{1}{2}\text{Re}\left[Z_{\text{w}}\right]\left|I_{\text{eq}}\right|^{2} = \frac{1}{2}\text{Re}\left[Z_{\text{w}}\right]\frac{\left|E_{0}\right|^{2}}{\left|R_{\text{scat}} + j\omega L + Z_{\text{w}}\right|^{2}} \tag{3.5}$$

It has been shown in the previous section how Z_{w} decreases as the wire radius increases. Moreover, it can be inferred from (2.39) that L dominates over R_{scat} for electrically thin wires ($k_0 a \ll 1$) (i.e., thin wires are inefficient scatterers). Therefore, it can be concluded that L defines the current flowing along wires much thicker than the penetration depth, i.e., in the SE limit, so that the absorbed power can be approximately written as

$$P_{\text{abs}}^{L} \simeq \frac{1}{2}R_{\text{w}}\frac{\left|E_{0}\right|^{2}}{\left(\omega L\right)^{2}} \tag{3.6}$$

Therefore, the absorption spectra of wires in which surfaces effects are dominant are expected to show a maximum of absorption at the FMR, corresponding to the maximum of the wire resistance, R_{w}. In other words, if the inductance produced by the equivalent current, L, is dominant, the wire distributed impedance, Z_{w}, has a negligible impact on the equivalent current, I_{eq}, and the absorption is maximized at the maximum of losses.

By contrast, Z_{w} becomes comparable to L as the radius decreases. This fact shifts the absorption maximum towards higher frequencies, since the capacitive contribution of X_{w} above the resonance compensates L, resulting in an increase of the equivalent current I_{eq}. Similarly, the inductive contribution of X_{w} below the resonance produces a decrease of I_{eq}, and thus a minimum of absorption. As a result, the absorption spectra of wires with intermediate radii are characterized by the sequence of a minimum and a maximum.

Subsequently, the wire resistance R_{w} becomes the dominant term for even thinner wires, so that the absorbed power simplifies to

$$P_{\mathrm{abs}}^{L} \simeq \frac{1}{2} R_{\mathrm{w}} \frac{\left|E_0\right|^2}{R_{\mathrm{w}}^2} = \frac{1}{2} \frac{\left|E_0\right|^2}{R_{\mathrm{w}}} \tag{3.7}$$

Counterintuitively, (3.7) reveals that the absorbed power is inversely proportional to losses for wires with radius smaller than the penetration depth. Therefore, such wires present a minima of absorption at the FMR resonance. In circuital terms, the excess of losses at the FMR produces a reduction of the excited current, which leads to a minimum of absorption. Note that these anomalous minima on the absorption spectrum have been erroneously interpreted by other authors as evidence of antiferromagnetic resonances [24], or even as an experimental proof of double negative metamaterials based on ferromagnetic wires [31, 36, 52].

Finally, the QS limit is reached as the wire radius becomes much smaller than the penetration depth, and the fields fully penetrate into the wire. In such a case, the electric and magnetic responses decouple, and a flat absorption spectra is to be expected. Specifically, $Z_{\mathrm{w}} \simeq \left(\pi a^2 \sigma\right)^{-1}$ is dominant over the other terms, so that the absorbed power can be written as

$$P_{\mathrm{abs}}^{L} \simeq \frac{1}{2} \pi a^2 \sigma \left|E_0\right|^2 \tag{3.8}$$

which is indeed a frequency independent absorption spectrum, corresponding to the volume integration of a uniform electric field over the electric losses (conductivity) of the wire. In passing, note that second order effects, which are usually hidden behind the dominant FMR resonance, could be more easily observed as small alterations of such flat spectra.

Although this equivalent circuit model clarifies the absorption spectrum, it is still not possible to identify the exact position of the resonance through a simple inspection. This can be solved by noting that the scattered power, P_{scat}^{L}, is also proportional to the square of I_{eq}, as shown in equation (2.42). Thus, the absorbed to scattered power ratio defined here as

$$\frac{P_{\mathrm{abs}}}{P_{\mathrm{scat}}} = \frac{R_{\mathrm{w}}}{R_{\mathrm{scat}}} \tag{3.9}$$

is independent of the current excited in the wire, and features a maximum at the resonance independently on the wire geometry. Therefore, such ratio can be adopted as a size-independent indicator of the FMR resonance frequency position.

3.3.1.2 Experimental Verification

Three different Co-rich $(\mathrm{Co}_{0.94}\mathrm{Fe}_{0.06})_{75}\mathrm{Si}_{12.5}\mathrm{B}_{12.5}$ ferromagnetic wires with 22.5 μm, 5 μm and 2 μm metallic radius and mean total diameter (including the Pyrex coating) of 65 μm, 33 μm and 14 μm, respectively, have been employed to experimentally validate the theoretical analysis. The samples have been fabricated by means of the Taylor-Ulitovsky technique [7, 8] in collaboration with Prof. M. Vázquez at the Material Science Institute of Madrid (ICMM). The experiment consisted of the waveguide experimental setup described in Section 2.3.3, and the measurements were carried out at the measurement laboratory of the Antenna Group, Public University of Navarra, by A. Labrador (Physics Department, Public University of Navarra), who provided the measured S-parameters.

As theoretically developed in Section 2.3.3, the incident electromagnetic field impinges on the ferromagnetic wire, which scatters some electromagnetic power in the form of cylindrical waves that, due to the influence of the metallic walls, is reflected back and transmitted forward as the TE_{10} waveguide mode. Therefore, the scattered power is proportional to twice the measured reflection power coefficient, $P_{\mathrm{scat}} \propto 2R = 2|S_{11}|^2$, and the absorbed power is proportional to the absorption power coefficient, $P_{\mathrm{abs}} \propto A = 1 - |S_{11}|^2 - |S_{21}|^2$. Consequently, the absorbed to scattered power ratio can be estimated as $P_{\mathrm{abs}}/P_{\mathrm{scat}} \simeq A/2R$.

The experimental data corresponding to the absorption power coefficient and absorbed to scattered power ratio for the three different wires are gathered in Fig. 3.3. To begin with, Fig. 3.3(a) represents the absorbed to scattered power ratio for the wire with 22.5 μm radius. Each line corresponds to a different biasing DC magnetic field as indicated in Table 3.1. While the response is flat for a null biasing ($H_1 = 0$ kA/m), the absorbed to scattered power ratio of biased wires is characterized by a peak that increases its frequency position along with H_{DC}. According to our model, this peak corresponds to the resonance and has been marked with a vertical line to compare it with the absorption spectrum, which is represented in Fig. 3.3(d). The absorption spectrum is also characterized by a peak that increases its frequency position along with H_{DC}. In agreement with the theoretical model, the absorption maxima are shifted towards higher frequencies with respect to the resonance, i.e., the peak of

H_1	0.0 kA/m
H_2	89.4 kA/m
H_3	117.7 kA/m
H_4	146.0 kA/m

Table 3.1 – H_{DC} biasing magnetic field

$P_{\text{abs}}/P_{\text{scat}}$ ratio.

The measurements corresponding to the wire of 5 μm radius are depicted in Figs. 3.3(b) and (e). Again, the absorbed to scattered power ratio is characterized by a maximum peak, and the measured values are larger than those obtained for the wire of 22.5 μm radius. Despite using the same bias field and wire composition, the FMR frequencies do not coincide with those of the 22.5 μm radius wire. Note that this is a typical effect in glass-coated amorphous wires [3], produced by changes on the anisotropy field of the wires due to the mechanical stresses produced during the fabrication processes, which are a function of the wire geometry (metallic and total radius). As for the absorption spectrum, it describes the minimum-maximum sequence predicted by the theoretical model.

Finally, the absorbed to scattered power ratio and absorption spectra of the wire with 2 μm radius are depicted in Figs. 3.3(c) and 3.3(f), respectively. As with the other wires, the absorbed to scattered power ratio spectrum is characterized by a maximum, which confirms the independency of this figure with respect to the geometry, and thus the possibility to unequivocally identify the FMR frequency. Furthermore, it can be concluded that the measured values of absorbed to scattered power ratio increase along with the wire radius. This behavior is consistent with the fact that R_{w} increases along with the wire radius (see Fig. 3.2), while $R_{\text{rad}} = \eta_0 k_0/4$ is independent on the wire geometry. Moreover, the absorption minima of the wire of 2 μm are precisely centered at the FMR frequency. In accordance to the theoretical model, the excess of losses present at the resonance results in a dip on the absorption spectra, for wires smaller than the penetration depth.

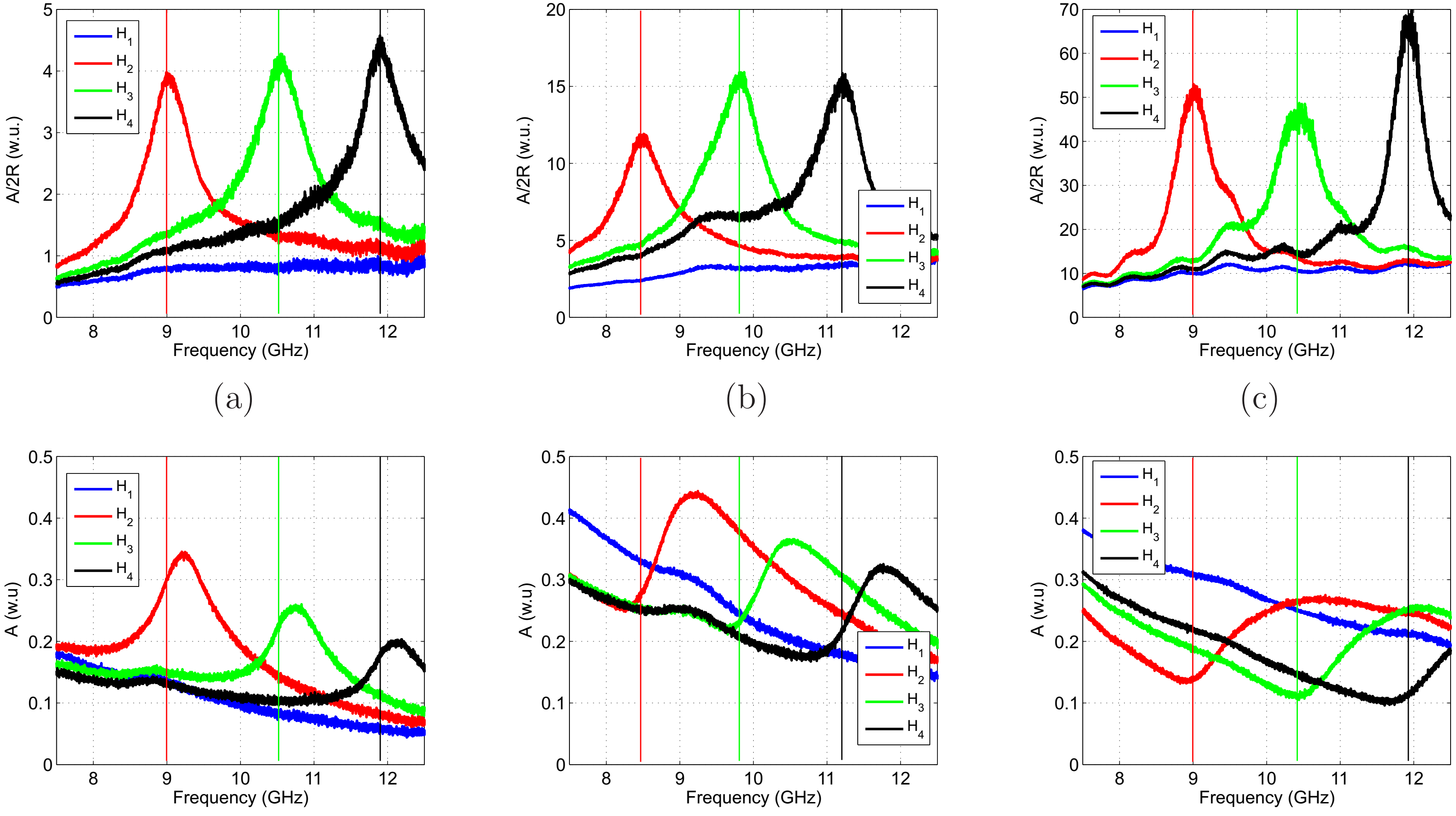

(a) (b) (c)

(d) (e) (f)

Figure 3.3 – Measured (a)-(c) absorbed to scattered power ratio and (d)-(f) absorption power coefficient for a Co-rich ferromagnetic wires of (a),(d) $a = 22.5\,\mu$m (b),(e) $a = 5\,\mu$m and (c),(f) $a = 2\,\mu$m radius, as a function of the applied DC magnetic field.

3.3.2 Absorption Spectrum of Short Wires

3.3.2.1 Theoretical Analysis

Axial resonances and non-uniform current distributions appear as the length of the wire decreases, which adds extra complexity to the absorption spectrum. For example, let us revisit Fig. 2.9, which depicted a comparison of the absorption spectrum predicted by the method of moments and circuit model for Co-rich wires with $22.5\,\mu$m, $5\,\mu$m and $2\,\mu$m radius and $2L = 9.8$ mm length. It is evident that the figure was already pointing out the strong correlation between the wire geometry and the absorption spectrum. However, the peculiarities of this set of absorption spectra can be clarified by means of the circuit model introduced in Section 2.4.2.

To this end, Fig. 3.4 represents the corresponding modified wire distributed impedance $Z_{\mathrm{w}}^{\mathrm{mod}} = R_{\mathrm{w}}^{\mathrm{mod}} + jX_{\mathrm{w}}^{\mathrm{mod}}$ of a wire with $2L = 9.8$ mm length and (a) $a = 22.5$ μm, (b) $a = 5$ μm, and (c) $a = 2$ μm radius, as well as the input impedance of the reciprocal transmitting PEC dipole antennas, $Z_{\mathrm{in}} = R_{\mathrm{in}} + jX_{\mathrm{in}}$. $Z_{\mathrm{w}}^{\mathrm{mod}}$ has been evaluated through (2.63), and Z_{in} has been calculated as in basic antenna textbooks (see e.g. [73], p. 918). The figure illustrates how $Z_{\mathrm{w}}^{\mathrm{mod}}$ is a scaled version of Z_{w} (see Fig. 3.2), as it could be inferred from its very definition, i.e., (2.63). By contrast, Z_{in} follows it the typical input impedance of a dipole antenna, i.e., the input impedance is dominated by a negative reactance at low frequencies, but the reactance grows along with frequency until it crosses zero at approximately 14.9 GHz ($L \simeq 0.485\lambda$). Similarly, the input resistance increases along with frequency, with a value of approximately 75 Ω at 15.3 GHz ($L \simeq 0.5\lambda$). In addition, the relative importance of $Z_{\mathrm{w}}^{\mathrm{mod}}$ with respect to Z_{in} increases as the wire radius decreases. In this manner, the capacitive impedance term X_{in} is the dominant term for the wire of $a = 22.5\,\mu$m radius, whereas the resistive $R_{\mathrm{w}}^{\mathrm{mod}}$ term is dominant for the wire of $a = 2\,\mu$m radius.

In view of the balance between the impedance terms, the two absorption peaks observed for the wire of $22.5\,\mu$m radius (see Fig. 2.9) can be explained as follows: the first peak is centered close to 9 GHz, where X_{in} dominates over the other impedance terms, and therefore the absorption is maximized due to an increase of losses at the FMR. This peak is slightly shifted below 9 GHz, due to the compensation of the capacitive X_{in} and inductive $X_{\mathrm{w}}^{\mathrm{mod}}$ impedance terms. On the contrary, the second peak is placed close to an axial resonance, i.e., the maximum is mostly

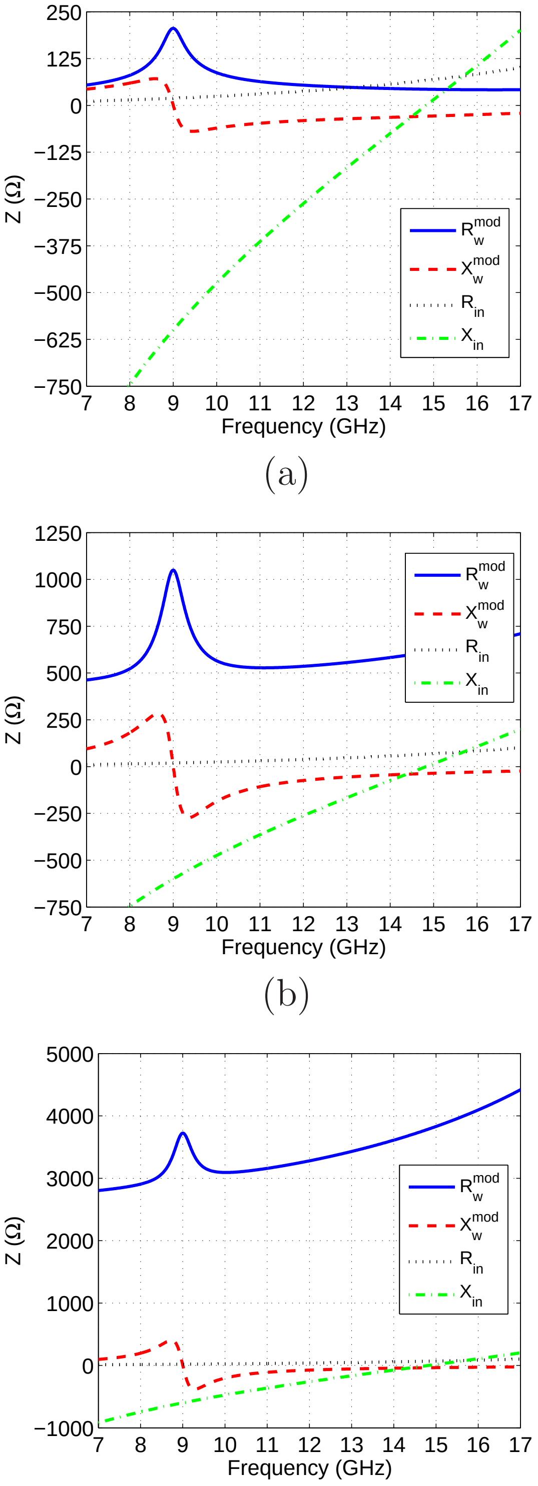

(a)

(b)

(c)

Figure 3.4 – Modified wire surface impedance $Z_\mathrm{w}^\mathrm{mod} = R_\mathrm{w}^\mathrm{mod} + jX_\mathrm{w}^\mathrm{mod}$ of a wire with $2L = 9.8$ mm length and (a) $a = 22.5\ \mu$m, (b) $a = 5\ \mu$m, and (c) $a = 2\ \mu$m radius, as well as the input impedance of the reciprocal transmitting antennas, $Z_\mathrm{in} = R_\mathrm{in} + jX_\mathrm{in}$.

produced by an enhancement of the current excited in wire when the overall impedance is minimized. In this manner, although $X_{\text{in}} \sim 0$ at approximately 14.9 GHz, the balance between X_{in}, $X_{\text{w}}^{\text{mod}}$, R_{in} and $R_{\text{w}}^{\text{mod}}$ results in a maximum of absorption at 14.5 GHz.

Similarly, the absorption spectrum for the wire of $a = 5$ μm radius is also characterized by two peaks corresponding to material and axial resonances (see Fig. 2.9). The differences with respect to the absorption spectrum of the wire of $a = 22.5\,\mu$m radius are a larger damping and broadening of the axial resonance, as well as a larger frequency shift in both, the material and the axial absorption peaks. Both differences correspond to an increased valued of $Z_{\text{w}}^{\text{mod}}$ as compared to X_{in}.

As for the wire of $2\,\mu$m radius, it is clear from Fig. 3.4 that the wire resistance $R_{\text{w}}^{\text{mod}}$ is dominant over the other impedance terms. In this manner, a minimum of absorption is centered at the FMR, and the axial resonance has been completely damped.

3.3.2.2 Experimental Verification

The experimental verification of the absorption spectrum of short ferromagnetic wires has been carried out with same Co-rich wires employed for the validation of the long wires spectrum. In fact, the experimental setup is also the same, with the only difference that rather than connecting the wires to the waveguide walls, they have been cut to a length of 9.8 mm, and are suspended within the waveguide on a Rohacell foam ($\epsilon_r \simeq 1.003$), with no contact with the metallic walls. Again, the measurements were carried out by A. Labrador.

Fig. 3.5 gathers all the experimental data, i.e., the measured absorbed to scattered power ratio and absorption power coefficient for the different wires as a function of the DC magnetic field. To begin with, Figs. 3.5(a) and (b) depict the spectra of absorbed to scattered power ratio and absorption, respectively, for the wire of $22.5\,\mu$m. As it is shown, the unbiased wire ($H_1 = 0$) presents a flat spectrum of absorbed to scattered power ratio while its absorption spectrum is characterized by a maxima, not present in the infinitely-long wire (see Fig. 3.3(d)). Therefore, this maximum is ascribed to an axial resonance in the wire. Note that this resonance appears significantly shifted from the half-wavelength point due to both, the impact of the Pyrex coating (described in Appendix B), and the loading of the waveguide.

When the wires are biased ($H_{DC} \neq 0$), a peak of absorbed to scattered power ratio can be observed in Fig. 3.5(a), which again allow us to identify the FMR frequency position. Moreover, an additional maximum appears on the absorption spectrum. As predicted by the theory, this maximum is produced by an increase of $R_{\mathrm{w}}^{\mathrm{mod}}$ at the FMR. However, it is located at frequencies below the resonance due to the compensation of the capacitive input impedance ($X_{\mathrm{in}} < 0$), with the inductive $X_{\mathrm{w}}^{\mathrm{mod}} > 0$ below the resonance. It is also observed that this frequency shift between the first absorption maxima and the FMR frequency increases along with the bias field. The reason is that as the FMR frequency approaches the half-wavelength resonance, the smaller X_{in} is in the vicinity of the resonance. Thus, the compensation of X_{in} with $X_{\mathrm{w}}^{\mathrm{mod}}$ gets stronger, and the shift of the absorption peak relative to the FMR increases along with the biasing field. Note also that changing the biasing shifts towards higher frequencies the peak produced by the axial resonance. This is is produced by the capacitive wire impedance ($X_{\mathrm{w}}^{\mathrm{mod}} < 0$) above the resonance.

The measurements corresponding to the wire of $5\,\mu$m radius are depicted in Figs. 3.5(b) and (e). Since electromagnetic fields penetrate more inside this wire, the strength of both absorption peaks, the one produced by the half-wavelength resonance and the one produced by the FMR resonance, become comparable. For the same reason, the shifts produced by the changes in the biasing fields are more pronounced.

By contrast, the wire of $2\,\mu$m radius features a completely different behavior. In correspondence with the theoretical model, Fig. 3.5(f) demonstrates that the axial resonance vanishes for very thin wires. In addition, the obserbed absorption spectra are characterized by a minimum. Unfortunately, the measurements of absorption to scattered power ratio were too noisy and cannot be interpreted (see Fig. 3.5(c)). The reason is the small reflection produced by a short wire of $2\,\mu$m radius ($6.67 \cdot 10^{-5}\lambda$ at 10 GHz).

3.4 Conclusions

A detailed analysis of the transition from surface to bulk phenomena in the scattering by ferromagnetic wires has been presented in this chapter. This effect (or collection of effects) takes place in GHz frequency range for conductive ferromagnetic wires with radius on the orders of microns, and has far-reaching implications in the scattering by ferromagnetic wires.

To begin with, it has been shown how the MI effect tends to disappear

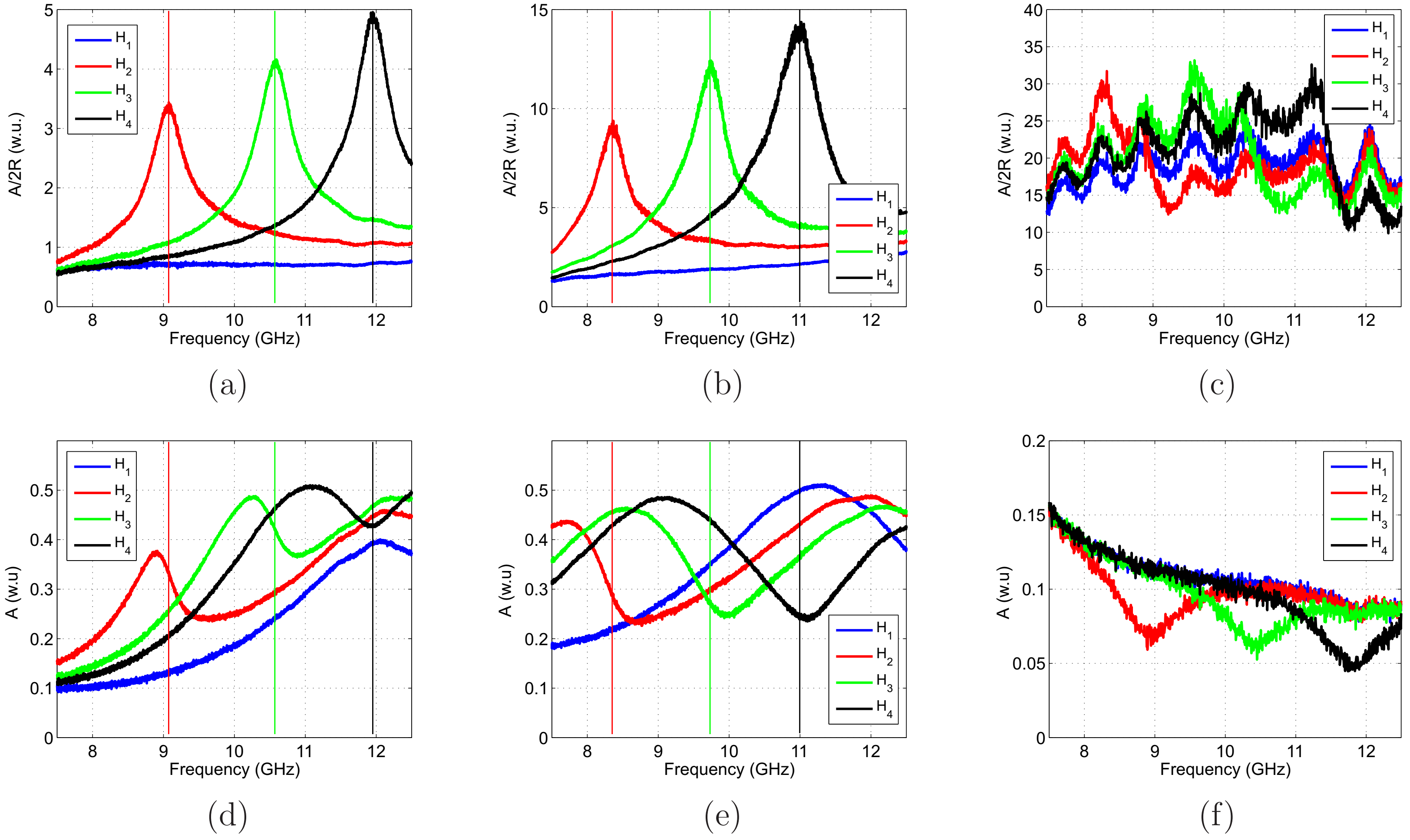

(a) (b) (c)

(d) (e) (f)

Figure 3.5 – Measured (a) absorbed to scattered power ratio and (b) absorption power coefficient, for a Co-rich ferromagnetic wire of $a = 22.5\,\mu$m radius and $2L = 9.8\,$mm length, as a function of the applied DC magnetic field.

in the SE and QS limits. Therefore, those wires with radii in the transition from surface to bulk effects result in the strongest FMR-based MI effect. Furthermore, it has been demonstrated that such wires can provide reconfigurable, resistive, inductive and capacitive loading. However, it has been also found that the wire distributed resistance is always larger than the wire distributed reactance, which limits the scope of ferromagnetic wires for applications where efficiency is critical.

Finally, it has been illustrated how this collection of effects leads to a complex size-dependent absorption spectrum. However, the peculiarities of the absorption spectrum can be clarified by means of the circuit models formulated in Chapter 2. Moreover, it has been found that the absorbed to scattered power ratio is a size-independent indicator that enables the identification of the FMR frequency.

Chapter 4

Fundamental Limits in the Scattering by Ferromagnetic Wires

4.1 Introduction

Controlling the balance between the extracted, absorbed, scattered and reactive powers excited in a scattering process is of natural interest for a wide range of applications. To mention some of them, maximizing the absorbed power is the design goal for communications links, power harvesting devices and sensors. For the specific case of low-observability sensors, the typical demand is to produce a high absorbed-to-scattered power ratio, though the absorbed power level must be kept over a certain sensitivity threshold. Furthermore, while anti-radar/cloaking systems are essentially focused on the minimization of the scattered power, resonant scatterers are also of interest, e.g., in the design of passive RFID tags and, in general, to enhance any kind of electromagnetic wave- (e.g., light-) matter interaction effects. For most of these applications, the optimal design usually involves a desire to eliminate the reactive power. On the other hand, the amount of reactive power could be employed to tailor the phase-shift (and therefore time delay) between the excitation and the response of the scatterer.

The balance of powers is restricted naturally by fundamental principles such as energy conservation and causality. For example, whenever a sensor captures power from an electromagnetic field, it also produces a disturbance in the field which is detectable by an external observer. Although this disturbance can be minimized (for example, by using cloaked [76] and forward-scattering [77] sensors), a residual amount of scattered field is produced even with the most careful design. The reason for this is that the power carried by the external field must be reduced by the amount of absorbed power. Therefore, the absorption and scattering processes are intimately correlated, which restricts the power captured by a sensor as a function of the disturbance created in the external field in association with the fields induced within the sensor.

Constrained to far-field (FF) interactions, the correlation between the absorption and scattering processes has been studied by means of the optical theorem [77], multipolar decomposition [78,79] and equivalent circuit model approaches [79]. All these studies agree that while the ratio of the absorbed to scattered power can be made as large as desired, it comes at the expense of losing absorbed power. In particular, maximization of the absorbed power imposes a constraint, i.e., the equality of the absorbed and scattered powers [78, 79]. In antenna terminology, as the re-radiation from a receiving antenna is diminished, its gain decreases with respect to the maximal antenna gain [59, 80]. This maximum point has been shown to occur when the absorbed and scattered powers are equal [79]. In other words, there is a tradeoff between the visibility and effective area of a receiving antenna.

Similar restrictions are bound to appear in ferromagnetic wires based systems. Therefore, this chapter is focused on deriving the limits of absorbed, scattered and extracted powers that arise from the correlation between absorption and scattering processes in the scattering by ferromagnetic wires. To this end, the problem is addressed from circuit model (Section 4.2) and multipolar (Section 4.3) approaches. The extrapolation of the presented results to arbitrary scatterers is also discussed. Finally, the technological implications of the derived limits are analyzed in Section 4.4.

4.2 Circuit Model Approach

Chapter 2 demonstrates that the scattering by a thin ferromagnetic wire is equivalent to that of an impedance loaded wire. In fact, if the load of the latter is set according to (2.40), both structures produce the same scattered fields, and an external observer will not find any difference. In addition, it was shown that the equivalent current can be computed following the circuit model depicted in Fig.4.1. Let us make use of such circuit model to analyze some fundamental limits in the scattering by ferromagnetic wires. To this end, note that, as it was shown in Chapter 2, (2.41)-(2.42), the absorbed and scattered powers per unit length can be written in circuital terms as follows

$$P_{\text{abs}}^{L} = \frac{1}{2} R_{\text{w}} \left| I_{\text{eq}} \right|^2 = \frac{1}{2} R_{\text{w}} \frac{\left| E_0 \right|^2}{\left| R_{\text{scat}} + R_{\text{w}} + j \left(\omega L + X_{\text{w}} \right) \right|^2} \tag{4.1}$$

$$P_{\text{scat}}^{L} = \frac{1}{2} R_{\text{scat}} \left| I_{\text{eq}} \right|^2 = \frac{1}{2} R_{\text{scat}} \frac{\left| E_0 \right|^2}{\left| R_{\text{scat}} + R_{\text{w}} + j \left(\omega L + X_{\text{w}} \right) \right|^2} \tag{4.2}$$

According to the optical theorem [81, 82], as the scatterer interacts with the incident field, it extracts a certain amount of power from it. In this manner, the extracted power is defined as the power depleted from the incident field, which then constitutes the addition of absorbed and scattered powers, i.e., $P_{\text{ext}} = P_{\text{scat}} + P_{\text{abs}}$. Aside from adding absorbed and scattered powers, the extracted power can be computed in virtue of Pointing's theorem as the surface integration of the cross-products of incident and scattered fields [82,83]. Furthermore, P_{ext} is also determined in virtue of the optical theorem as a function of the forward scattering amplitude [81]. In our case, the equivalent circuit model suggests that the extracted power per unit length P_{ext}^{L} can be written in circuital terms as follows

$$\begin{aligned} P_{\text{ext}}^{L} &= \frac{1}{2} \left(R_{\text{scat}} + R_{\text{w}} \right) \left| I_{\text{eq}} \right|^2 \\ &= \frac{1}{2} \left(R_{\text{scat}} + R_{\text{w}} \right) \frac{\left| E_0 \right|^2}{\left| R_{\text{scat}} + R_{\text{w}} + j \left(\omega L + X_{\text{w}} \right) \right|^2} \end{aligned} \tag{4.3}$$

Formulating power quantities in circuital terms as in (4.1)-(4.3) not only provides a straightforward way to compute the absorbed, scattered and extracted powers involved in the scattering by a ferromagnetic wire, but also reveals the intrinsic limits in the balance of powers. A key aspect is that the scattering resistance, $R_{\text{scat}} = \eta_0 k_0 / 4$, is real, positive and non-vanishing. More strikingly, it is independent of the wire and incident field properties. Therefore, it can be concluded that there is an inherent radiative component associated with the equivalent current distribution that forms the scattered field. Thus, when a given current is excited to create either absorption or reactive energy, a certain amount of power

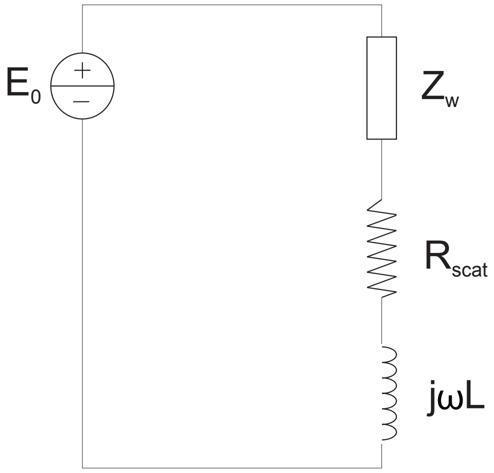

Figure 4.1 – Equivalent circuit model of the scattering by a ferromagnetic wire.

also must be scattered. Consistently, there cannot be absorption without scattering.

In circuital terms, if there is a certain amount of current I_{eq} flowing on the circuit, then there is also scattered power: $\frac{1}{2}\, R_{\text{scat}}\, |I_{\text{eq}}|^2$. Since R_{scat} cannot be controlled either by the wire geometry or its electromagnetic properties, the amount of scattered power can only be manipulated through the amount of current, which imposes some limitations on the reactive and absorbed powers. Therefore, this aspect of the circuit model also has implications in elucidating the maximal extracted power and its contributions from the scattered and absorbed powers.

For example, it is clear from (4.3) that the extracted power is maximized when $X_{\text{w}} + \omega L = 0$, and when the total resistance $R_{\text{scat}} + R_{\text{w}}$ is made as low as possible. Furthermore, since R_{scat} is a fixed quantity, the extracted power is maximized for $R_{\text{w}} = 0$, which only occurs for the lossless, zero absorption case. This maximum value is expressed in terms of the field quantities as:

$$P_{\text{ext}}^{L,MAX} = \frac{1}{2}\frac{|E_0|^2}{R_{\text{scat}}} = \frac{2\,|E_0|^2}{\eta_0 k_0} \tag{4.4}$$

For this case, $P_{\text{ext}}^{L} = P_{\text{scat}}^{L}$. This means (4.4) also corresponds to the maximal scattered power per unit length, i.e., $P_{\text{ext}}^{L,MAX} = P_{\text{scat}}^{L,MAX}$.

Consequently, the maximal extracted and scattered powers, given by (4.4), represent the maximal value that could ever be achieved by any wire placed in the presence of the same incident field. Therefore, since the maximal extracted power is obtained for the lossless case, it can be concluded, counter-intuitively, that the presence of absorption limits the ability of the wire to extract power from the incident field. Fundamentally, the wire, even though it is lossy, cannot absorb all the power which could be extracted from the incident field, i.e., the lossless case value $P_{\text{ext}}^{L,MAX}$. In particular, looking at (4.1) and recalling that $R_{\text{scat}} = 0$ must be discarded, it is clear that the absorbed power is maximized when $X_{\text{w}} + \omega L = 0$ and $R_{\text{scat}} = R_{\text{abs}}$. This leads to the maximum absorbed power per unit length expression:

$$P_{\text{abs}}^{L,MAX} = \frac{1}{2}\frac{|E_0|^2}{4R_{\text{scat}}} = \frac{|E_0|^2}{2\eta_0 k_0} \tag{4.5}$$

Moreover, with $R_{\text{scat}} = R_{\text{abs}}$, it then directly follows that $P_{\text{scat}} = P_{\text{abs}}$ for $P_{\text{abs}}^{L,MAX}$.

In addition, a simple comparison between (4.4) and (4.5) reveals that the maximal absorbed power is a quarter of the maximal extracted power, i.e., the wire cannot absorb more than 25% of the power that could ever be extracted from the incident field, the latter being defined by the lossless limit, $P_{\text{ext}}^{L,MAX}$. More specifically, the absorbed and scattered powers are equal *only* at the point of maximal absorption. Therefore, only 50% of the available power in this case can be extracted as the absorbed power. However, only 50% of $P_{\text{ext}}^{L,MAX}$ is available for this maximal absorption case.

On the other hand, this fact should not lead one to the wrong conclusion that the absorbed power can never exceed 50% of the power extracted from the incident field. As pointed out here, if one is willing to sacrifice the amount of power absorbed from the incident field, one can make the ratio of P_{abs}^{L} to P_{scat}^{L} as large as one wants. In terms of the circuit model, the absorbed to scattered power ratio is simply proportional to $R_{\text{w}}/R_{\text{scat}}$, and it can be forced as large as desired, at the cost of reducing P_{abs}^{L}.

Finally, note that one must be very careful when relating these limits of the extracted, scattered and absorbed powers with the power supplied by the sources of the incident field. The latter is defined simply as [62]

$$P_{\text{sup}} = -\frac{1}{2}\iiint_{V_i} \text{Re}\left[\left(\mathbf{E}^{\text{i}} + \mathbf{E}^{\text{s}}\right)\cdot\left(\mathbf{J}_{\text{i}}\right)^* + \left(\mathbf{H}^{\text{i}} + \mathbf{H}^{\text{s}}\right)\cdot\left(\mathbf{M}_{\text{i}}\right)^*\right] dV \tag{4.6}$$

where V_i is the volume contained in the surface S_i surrounding the free sources . From (4.6) it is concluded that, in general, the power supplied by the sources is not uniquely defined by the incident field, but also depends on the scattered field. Therefore, if the wire is close enough to significantly alter the supplied power, the aforementioned percentage limits cannot be directly related to it. On the contrary, the power supplied by sources in their far fields, which are of great interest in a wide range of technological applications, is independent of the scattered field and all the information about the power available for the wire is contained in the incident field. Therefore, for the far-field case treated here, in which the source and the scattered field currents are essentially decoupled, the maximal extracted power, $P_{\text{ext}}^{L,MAX}$, is a true estimation of the maximum power available for the scattering and absorption processes.

Consequently, the limits considered here, which are based strictly on the power that can be extracted from a given incident field, are only meaningful for the intended far-field interactions. In near-field scenarios, efficiencies defined in terms of power ratios to the supplies power $P_{\text{abs}}^{L}/P_{\text{sup}}^{L}$ and $P_{\text{scat}}^{L}/P_{\text{sup}}^{L}$ play a major role. Although near-field effects are outside the scope of this dissertation, it is worth noting that they have been addressed by the author of this dissertation and coworkers in [84].

4.3 Multipolar Approach

On might wonder up to which point the conclusions extracted in the previous section can be extrapolated to other structures. Admittedly, the equivalent circuit model has been derived for 2D thin wire structures. However, the limits seem so natural when a circuit model representation is considered, that it appears that similar conclusions could be drawn for the scattering by a large number of, if not all, objects.

However, one must be careful when dealing with circuit models. In fact, circuit models are formulated for many different purposes, and, therefore, the information provided by these models in terms of absorbed and scattered powers can be, in many cases, very limited. For example, popular Norton and Thevenin circuit models are useful to describe the voltage and current excited at an antenna port. However, such models only retrieve the scattered power produced by the re-radiation from the load; and thus they do not provide the complete picture as far as the scattered power is concerned (see, e.g., [85–88] and the references therein). As another example, the circuit model proposed by Engheta et al. for nanospheres [89] is useful to design complex optical and IR circuits. However, such a circuit is based on the QS approximation and disregards scattering losses. By contrast, circuit models can be explicitly formulated to determine the absorbed and scattered powers involved in a scattering problem. For example, the author of this dissertation and coworkers have derived circuit models for the scattering problem of spherical objects of arbitrary size [79]. The conclusions drawn in such study are fully consistent with those develop in the previous section.

A more generic, albeit more mathematical, derivation of the previously introduced limits can be done by following a purely multipolar approach. Let us consider first an arbitrary 2D problem. As demonstrated in Chapter 2, equations (2.13)-(2.14), the quantities: P^L_{abs}, P^L_{scat}, can be written explicitly as the multipole sums:

$$P^L_{\text{abs}} = -\frac{2}{\eta_0 k_0} \sum_{n=-\infty}^{\infty} \sum_{Z=E,M} \operatorname{Re}\left[\left(A_n^{TZ}\right)^* B_n^{TZ}\right] + \left|B_n^{TZ}\right|^2 \tag{4.7}$$

$$P^L_{\text{scat}} = \frac{2}{\eta_0 k_0} \sum_{n=-\infty}^{\infty} \sum_{Z=E,M} \left|B_n^{TZ}\right|^2 \tag{4.8}$$

Similarly, adding (4.7) and (4.8) it is found that the extracted power per unit length, $P^L_{\text{ext}} = P^L_{\text{abs}} + P^L_{\text{scat}}$, can be alternatively written as the multipolar sum

$$P^L_{\text{ext}} = -\frac{2}{\eta_0 k_0} \sum_{n=-\infty}^{\infty} \sum_{Z=E,M} \operatorname{Re}\left[\left(A_n^{TZ}\right)^* B_n^{TZ}\right] \tag{4.9}$$

Let us address the limits of the absorbed, scattered and extracted power on the basis of these multipolar sums. To begin with, inspecting (4.7) it is clear that P^L_{abs} depends on the scattering coefficients, B_n^{TZ}, as well as the source coefficients in the source region, i.e., A_n^{TZ}. To maximize the absorbed power for a given source, let us first separate the term inside the brackets into real and imaginary parts, and then take the derivatives with respect to $\operatorname{Re}\left[B_n^{TZ}\right]$ and $\operatorname{Im}\left[B_n^{TZ}\right]$. One finally finds that P^L_{abs} is maximized for the following condition between the source and scattering coefficients:

$$B_n^{TZ} = -\frac{1}{2} A_n^{TZ} \tag{4.10}$$

Substituting (4.10) into (4.7), one finds that the maximum absorbed power is given by

$$P^{L,MAX}_{\text{abs}} = \frac{1}{2\eta_0 k_0} \sum_{n=-\infty}^{\infty} \sum_{Z=E,M} \left|A_n^{TZ}\right|^2 \tag{4.11}$$

It is worth remarking that (4.11) is valid for 2D scatterers of arbitrary size, shape and constitutive parameters (e.g., non-reciprocal devices). Furthermore, introducing (4.10) into (4.8), one recovers the known result [77–79] that for maximal absorption to occur, the absorbed and scattered powers must be equal, i.e.,

$$P_{\text{abs}}^{L,MAX} = P_{\text{scat}}^{L}\Big|_{\max\left\{P_{\text{abs}}^{L}\right\}} \tag{4.12}$$

Note that $P_{\text{scat}}^{L}\big|_{\max\left\{P_{\text{abs}}^{L}\right\}}$ stands for the scattered power when the absorbed power is maximized. However, this does not correspond to the maximum scattered power.

Furthermore, as can be inferred from (4.8), minimizing the scattered power simply corresponds to minimizing the scattered field coefficients, $B_n^{TZ} \to 0$. Unfortunately, as it is also apparent from (4.7), the limit $B_n^{TZ} \to 0$ also implies zero absorption. Consequently, there can be no absorption without scattering. On the other hand, it also can be seen by inspecting (4.8) and (4.7) that P_{scat}^{L} decreases faster than P_{abs}^{L} as $B_n^{TZ} \to 0$. Therefore, the multipolar approach also ratifies that large absorbed to scattered power ratios are possible at the cost of losing absorbed power.

This analysis is valid for arbitrary incident fields, described by the coefficients A_n^{TZ}. Note that $P_{\text{abs}}^{L,MAX}$, as given by (4.11), is proportional to the magnitude squared of the source coefficients: $\left|A_n^{TZ}\right|^2$. Since (4.10) is defined in terms of them, this also means the maximum absorbed power intuitively grows as the source projects a larger field intensity onto the scatterer. As a particular example, let us take the coefficients of a plane wave with an electric field of magnitude E_0, polarized along the wire axis (z-axis), and propagating along the x-axis, i.e., $A_n^{TM} = j^n E_0$ and $A_n^{TE} = 0$ [62]. In such a case, the limit of absorbed power for this particular excitation is given by

$$P_{\text{abs}}^{L,MAX}\Big|_{\text{pw}} = \frac{1}{2\eta_0 k_0} \sum_{n=-\infty}^{\infty} |E_0|^2 \tag{4.13}$$

It can be readily checked that, under the thin wire approximation, i.e., considering the $n = 0$ mode only, (4.13) reduces to (4.5). In other words, the limit derived based on the multipolar approach is fully consistent with limit derived on basis of the equivalent circuit model.

Consider also a finite size scatterer able to efficiently couple with a number of multipoles up to $n = N$, the limit of absorbed power is given by $P_{\text{abs}}^{L,MAX}\Big|_{\text{pw}} = \frac{|E_0|^2}{2\eta_0 k_0}(2N+1)$. For electrically large scatterers, a rule of thumb employed for the truncation of this series is $N = k_0 a$ [59]. This rule leads to $P_{\text{abs}}^{L,MAX}\Big|_{\text{pw}} = \frac{|E_0|^2}{2\eta_0}2a$, which corresponds to the integration of the density of incident power over the diameter of the circumference circumscribing the scatterer. In other words, the derived limit consistently recovers geometrical optics for large structures.

Note that this limit diverges as $N \to \infty$, which is a consequence of the infinity energy artificially carried by the plane-wave. In practice, as the effective area of the scatterer grows, the assumption of uniform illumination over the scatterer effective area no longer holds; and the plane-wave model cannot be employed. As a matter of fact, within the range of applicability of the plane-wave excitation, the scatterer is typically extracting only a small fraction of the power produced by the sources.

Let us now focus on the limits of scattered and extracted powers. Inspecting (4.8) reveals that P_{scat}^{L} grows along with B_n^{TZ}, and thus it cannot be maximized through the same derivation approach that was used for P_{abs}^{L}. In fact, the generality of the scatterer will be restricted in our analysis from now on to enable the derivation of the limits for the scattered and extracted powers. Specifically, let us assume that the scatterer is passive, linear, and that their surfaces are such that the cylindrical harmonics interact independently. In such a case, the scattered field coefficients are proportional to the incident field coefficients in the region of the scatterer, i.e.,

$$B_n^{TZ} = b_n^{TZ} A_n^{TZ} \tag{4.14}$$

and passivity holds independently for each multipole, i.e.

$$P_{\text{abs},n}^{TZ} = -\left|A_n^{TZ}\right|^2 \left\{\text{Re}\left[b_n^{TZ}\right] + \left|b_n^{TZ}\right|^2\right\} > 0 \tag{4.15}$$

Thus, $P_{\text{abs},n}^{TZ} > 0$ imposes the conditions: $\text{Re}\left[b_n^{TZ}\right] < 0$ and $\left|\text{Re}\left[b_n^{TZ}\right]\right| \geq \left|b_n^{TZ}\right|^2$. Furthermore, since $\left|\text{Re}\left[b_n^{TZ}\right]\right| \leq \left|b_n^{TZ}\right|$, $P_{\text{abs},n}^{TZ} > 0$ also requires $\left|b_n^{TZ}\right| \leq 1$. Therefore, the condition on the b_n^{TZ} coefficients to get maximal scattered power can be written as

$$\left|b_n^{TZ}\right|^2 = 1 \longrightarrow b_n^{TZ} = -1 \tag{4.16}$$

Therefore, the maximal scattered power per unit length is given by

$$P_{\text{scat}}^{L,MAX} = \frac{2}{\eta_0 k_0} \sum_{n=-\infty}^{\infty} \sum_{Z=E,M} \left|A_n^{TZ}\right|^2 \tag{4.17}$$

Again, the maximum scattered power is found four times larger than the maximum absorbed power, i.e.

$$P_{\mathrm{scat}}^{L,MAX}=4P_{\mathrm{abs}}^{L,MAX} \tag{4.18}$$

Moreover, the assumption $B_n^{TZ}=b_n^{TZ}A_n^{TZ}$ also allows us to write the extracted power as

$$P_{\mathrm{ext},n}^{TZ}=-\frac{2}{\eta_0 k_0}\sum_{n=-\infty}^{\infty}\sum_{Z=E,M}\left|A_n^{TZ}\right|^2\mathrm{Re}\left[b_n^{TZ}\right] \tag{4.19}$$

Equation (4.19) reveals that $P_{\mathrm{ext},n}^{TZ}$ increases along with Re $\left[b_n^{TZ}\right]$. Therefore, their upper limit is reached when $b_n^{TZ}=-1$ and, in this manner, the multipolar approach generalizes the result that extracted and scattered powers share the same upper bound. Thus, it can be concluded that the extracted power per unit length is maximized for the ideal lossless case and, therefore, the presence of losses limits the amount of power that can be extracted from the incident field.

Throughout the multipolar discussion of the scattered and extracted powers, the balance of powers for each multipole has been considered independently, assuming $B_n^{TZ}=b_n^{TZ}A_n^{TZ}$. Such condition is rigorously satisfied for cylindrical objects, and it is approximately satisfied by objects with soft surfaces. However, the limit of absorbed power (4.11) has been derived for completely arbitrary scatterers and it was found that, according to (4.10), such power is maximized under a condition in which the balance of powers for each multipole is considered independently. This result encourages to believe that the results in terms of scattered and extracted powers can indeed be generalized to arbitrary scatterers.

Finally, it is worth noting that for an arbitrary 3D object, e.g., a finite length ferromagnetic wires, the fields can be decomposed as a basis of spherical, instead of cylindrical, harmonics [59]. In such a case, the total power quantities can be associated to the sum of the same power quantity associated with each mode [84]:

$$P_{\mathrm{abs}}=-\sum_{n=1}^{\infty}\sum_{m=0}^{n}\sum_{l=e,o}\sum_{Z=E,M}\left\{\mathrm{Re}\left[\left(A_{nm}^{lTZ<}\right)^{*}B_{nm}^{lTZ}\right]+\left|B_{nm}^{lTZ}\right|^2\right\} \tag{4.20}$$

$$P_{\mathrm{scat}}=\sum_{n=1}^{\infty}\sum_{m=0}^{n}\sum_{l=e,o}\sum_{Z=E,M}\left|B_{nm}^{lTZ}\right|^2 \tag{4.21}$$

$$P_{\text{ext}} = -\sum_{n=1}^{\infty}\sum_{m=0}^{n}\sum_{l=e,o}\sum_{Z=E,M} \text{Re}\left[\left(A_{nm}^{lTZ<}\right)^{*} B_{nm}^{lTZ}\right] \tag{4.22}$$

Due to the symmetry between the sums of cylindrical (4.7)-(4.9) and spherical (4.20)-(4.22) multipoles, it is clear that the conclusions drawn in this Section can be extrapolated to 3D objects. As a matter of fact, a parallel demonstration by using spherical multipoles has been included by the author of the thesis an coworkers in [84].

4.4 Technological Implications

Aside from being a matter of interest in the fundamentals of applied electromagnetics, the previously derived limits have direct implications on some of the most promising microwave applications of ferromagnetic wires. Following the conclusions drawn in Chapter 2, the attention is focused on the design of contact-less sensors and electromagnetic absorbers.

To begin with, it has been found that the upper bound of scattered power can only be achieved with ideal lossless scatterers. Since ferromagnetic wires are quite lossy, it must be concluded that they cannot approach such limit. This is a drawback for the design of contact-less sensors, where the magnitude of interest is tracked through variations of the scattered field, and therefore a large scattered power is convenient to increase the dynamic range of the sensing system.

Moreover, note that the sensing mechanism ultimately relies on changes of the magnetic properties of the wires. As studied in Chapter 2, the influence of the magnetic properties of the wire on the scattered field is maximized for wire radii in the transition from surface to bulk effects, i.e., for very lossy wires. Therefore, the design of contact-less sensors based on ferromagnetic wires involves solving a compromise between how sensitive the wires are with respect to variations of the magnitude of interest (e.g., mechanical stresses), and how much power do the wires re-radiate to the receiver that records such variations. The design of contact-less sensors based on ferromagnetic wires is resumed in Chapter 7.

Let us now revisit the upper bound of the absorbed power. As derived in Section 4.2, the properties that a ferromagnetic wire must met to reach the limit of maximal absorption can be written in terms of its distributed resistance and reactance as follows

$$R_{\mathrm{w}} = R_{\mathrm{scat}} = \frac{\eta_0 k_0}{4} \tag{4.23}$$

$$X_{\mathrm{w}} = -\omega L = -\frac{\eta_0 k_0}{4}\frac{2}{\pi}\left[\ln\left(\frac{2}{k_0 a}\right) - \gamma\right] \tag{4.24}$$

Therefore, it can be concluded that for $k_0 a \ll 1$ (condition implicit in the thin wire approximation), the absolute value of the wire distributed reactance must be much higher than the wire resistance, $|X_{\mathrm{w}}| \gg R_{\mathrm{w}}$. As argued in Section 3.2, this is not possible with ferromagnetic wires with conductive cores and, counter-intuitively, it is found that ferromagnetic wires are too lossy to reach the limit of maximal absorption. This results limits the scope of very diluted mixtures of wires (in the sense of wires separated by distances comparable/larger to the wavelength of operation) as electromagnetic absorbers. Despite this limitation, reasonable diluted mixtures of wires (in the sense of interwire separations smaller than the wavelength of operation, but still leading to small filling factors) can be potentially adopted in the design of electromagnetic absorbers designed to hide large objects. This aspect is emphasized in Chapters 5 and 6.

4.5 Conclusions

This chapter has dealt with the limits in the balance of powers involved in the scattering by ferromagnetic wires (and many other objects). Specifically, the study confirms (by using circuital and multipolar approaches) the known result that absorbed and scattered powers must be equal for maximal absorption. Furthermore, it has been shown how extracted and absorbed powers share the same upper bound, which is four times larger than that of the absorbed power. It is then found that the maximal extracted power can only be achieved by an ideal lossless scatterer, and therefore the presence of losses limits the amount of power that can be extracted from the incident field. This principle is bound to impose difficulties in the design of a wide range of systems. For example, the design of contact-less sensors based on ferromagnetic wires present a compromise between how sensitive the wires are with respect to variations of the magnitude of interest (e.g., mechanical stresses), and how much power do the wires re-radiate to the receiver that records such variations. It has also been argued how ferromagnetic are too lossy to reach the upper bound of absorbed power, which limits the scope of very diluted mixtures of wires as electromagnetic absorbers.

Chapter 5

Artificial Electromagnetic Materials based on Ferromagnetic Wires

5.1 Introduction

One of the major challenges in the design of ferromagnetic wire-based devices is the analysis and modeling of structures composed of large assemblies of wires. Such structures have an overall size of several wavelengths, while having fine details of the order of the wire radius, several orders of magnitude smaller than the wavelength of operation. Furthermore, the interior of the wires must be accurately meshed, since, as it was pointed out in Chapter 3, small changes in the wire radii lead to dramatic changes in the response of ferromagnetic wires. This fact imposes a prohibitively dense mesh for structures of several wavelengths size, which hinders the evaluation of ferromagnetic wire-based systems through commercial software tools.

A useful tool to reduce the complexity of the design of such systems is the homogenization approach, namely, substituting a complex group of inclusions by a simple, effectively homogeneous material. In this regard, the effective permittivity of composites made of ferromagnetic microwires exhibiting GMI [34, 90], and the effective permeability of dense arrays of ferromagnetic wires exhibiting FMR [91, 92], have been theoretically addressed. This chapter attempts to complete these previous works by studying the effective permittivity of arrays of ferromagnetic nanowires exhibiting FMR, including both ferromagnetic micro and nanowires, and dense and sparse arrays of wires.

Aside from being a tool to simplify the analysis of complex systems, the development of artificial materials with engineered constitutive parameters has also become a matter of interest by itself. The topic has bloomed during the last decade, and it is usually addressed to as the metamaterial paradigm [93, 94]. In this regard, artificial electromagnetic materials based on ferromagnetic wires have been experimentally investigated in a joint effort between the Physics and Electrical and Electronic Engineering Departments of the Public University of Navarra.

In principle, the electric and magnetic properties of the wires would allow tailoring the composite permittivity and permeability with a single inclusion, while offering several tuning mechanisms that have already been discussed along the dissertation. Several experimental studies carried out at the Public University of Navarra [31] (and also at other institutions [36, 52, 53]) have reported transmission windows in arrays of ferromagnetic wires, which, following a similar thought process than that of D.R. Smith's seminal paper [54], were identified as an evidence of double negative (DNG) metamaterials (in the sense of an artificial electromagnetic material simultaneously having negative permittivity and permeability). However, as discussed in Chapter 1, the conclusion extracted from the experimental data is controversial since the filling factor of the measured arrays of wires is too small to have a significant effective permeability. Moreover, there are multiple explanations for the appearance of a transmission window without recurring to the concept of DNG metamaterials. Therefore, the homogenization approach developed in this Chapter also aims to shed more light into those experiments.

5.2 From Cylindrical Harmonics to Effective Parameters

Expanding the scattered field over a basis of cylindrical harmonics (see Section 2.3.1) can also be exploited to estimate the constitutive parameters of a composite of ferromagnetic wires, provided that the contribution of each mode to the material parameters can be identified. This can be done in virtue of the equivalence theorem [62]. In essence, the wire can be replaced by surface electric and magnetic currents [62], which for the dominant polarization with the electric field directed along the wire axis can be written as

$$\mathbf{J}_{\mathrm{s}} = \hat{\mathbf{n}} \times \mathbf{H}^{int} = H_{\phi}^{int}\hat{\mathbf{z}} \tag{5.1}$$

$$\mathbf{M}_{\mathrm{s}} = -\hat{\mathbf{n}} \times \mathbf{E}^{int} = E_{z}^{int}\hat{\boldsymbol{\phi}} \tag{5.2}$$

where H_{ϕ}^{int} and E_{z}^{int} are the tangential components of the fields on the surface of the wire, $r = a$, which for a wire of uniform and static magnetization can be written as (see Section 2.3.1.2)

$$E_{z}^{int}(a,\phi) = E_0 \sum_{n=-\infty}^{\infty} j^n c_n^{TM} J_n(k_{\mathrm{w}}a) e^{-jn\phi} \tag{5.3}$$

$$H_{\phi}^{int}(a,\phi) = -\frac{jE_0}{\eta_{\mathrm{w}}} \sum_{n=-\infty}^{\infty} j^n c_n^{TM} \left[J_n'(k_{\mathrm{w}}a) - n\frac{\mu_t}{\mu}\frac{J_n(k_{\mathrm{w}}a)}{k_{\mathrm{w}}a} \right] e^{-jn\phi} \tag{5.4}$$

with

$$c_n^{TM} = \frac{2j}{\pi k_0 a} \frac{1}{D_n H_n^{(2)}(k_0 a) - H_n^{(2)\prime}(k_0 a) J_n(k_{\mathrm{w}}a)} \tag{5.5}$$

where D_n is defined as

$$D_n = \frac{\eta_0}{\eta_{\mathrm{w}}} \left[J_n'(k_{\mathrm{w}}a) - n\frac{\mu_t}{\mu k_{\mathrm{w}} a} J_n(k_{\mathrm{w}}a) \right] \tag{5.6}$$

Once the electric and magnetic currents are known, the electric and magnetic polarization densities of a composite made of ferromagnetic wires can be found by integration [95]

$$\mathbf{P} = \frac{1}{j\omega V} \int_{V'} \left(\mathbf{J}_{\mathrm{s}} - j\omega\frac{\varepsilon_0}{2} (\mathbf{r}' \times \mathbf{M}_{\mathrm{s}}) \right) dV' \tag{5.7}$$

$$\mathbf{M} = \frac{1}{j\omega V} \int_{V'} \left(\mathbf{M}_{\mathrm{s}} + j\omega\frac{\mu_0}{2} (\mathbf{r}' \times \mathbf{J}_{\mathrm{s}}) \right) dV' \tag{5.8}$$

For the particular currents of (5.1) and (5.2), the electric and magnetic polarizations densities reduce to

$$\mathbf{P} = \frac{1}{j\omega V} \int_{V'} \left(H_{\phi}^{int} - j\omega\frac{\varepsilon_0}{2} a E_z^{int} \right) \hat{\mathbf{z}} dV' \tag{5.9}$$

$$\mathbf{M} = \frac{1}{j\omega V} \int_{V'} \left(E_z^{int} - j\omega\frac{\mu_0}{2} a H_{\phi}^{int} \right) \hat{\boldsymbol{\phi}} dV' \tag{5.10}$$

It is worth noting that the terms inside the integrals of (5.9) and (5.10) are series of $e^{jn\phi}$ azimuthal harmonics, and that the volume integral is reduced to the wire surface integral, so that the electric and magnetic polarization densities can be rewritten as

$$\mathbf{P} = \frac{1}{j\omega V} \sum_{n=-\infty}^{\infty} P_n \int_0^{2\pi} e^{-jn\phi} \hat{\mathbf{z}} a d\phi \tag{5.11}$$

$$\mathbf{M} = \frac{1}{j\omega V} \sum_{n=-\infty}^{\infty} M_n \int_0^{2\pi} e^{-jn\phi} \left(-\sin\phi \hat{\mathbf{x}} + \cos\phi \hat{\mathbf{y}}\right) a d\phi \tag{5.12}$$

where

$$P_n = -j^{n+1} E_0 c_n^{TM} \left[\frac{D_n}{\eta_\mathrm{w}} + \omega a \frac{\varepsilon_0}{2} J_n\left(k_\mathrm{w} a\right)\right] \tag{5.13}$$

$$M_n = j^n E_0 c_n^{TM} \left[J_n\left(k_\mathrm{w} a\right) - \omega a \frac{\mu_0}{2} \frac{D_n}{\eta_\mathrm{w}}\right] \tag{5.14}$$

Note however that

$$\int_0^{2\pi} e^{-jn\phi} \hat{\mathbf{z}} d\phi = 2\pi \delta_\mathrm{0n} \hat{\mathbf{z}} \tag{5.15}$$

$$\int_0^{2\pi} e^{-jn\phi} \left(-\sin\phi \hat{\mathbf{x}} + \cos\phi \hat{\mathbf{y}}\right) d\phi = -j \left(\delta_\mathrm{1n} - \delta_\mathrm{-1n}\right) \pi \hat{\mathbf{x}} + \left(\delta_\mathrm{1n} + \delta_\mathrm{-1n}\right) \pi \hat{\mathbf{y}} \tag{5.16}$$

where δ_mn stands for the Kronecker delta. Thus, electric and magnetic polarization densities simplify to

$$\mathbf{P} = \frac{2\pi a}{j\omega V} P_0 \hat{\mathbf{z}} \tag{5.17}$$

$$\mathbf{M} = \frac{\pi a}{j\omega V} \left[-j \left(M_1 - M_{-1}\right) \hat{\mathbf{x}} + \left(M_1 + M_{-1}\right) \hat{\mathbf{y}}\right] \tag{5.18}$$

Therefore, the $n = 0$ mode determines the material permittivity, while the $n = \pm 1$ modes determine the material permeability. Note that higher order modes do not contribute to the electric and magnetic polarization densities, so more complex material parameters would be needed to include their contributions. Moreover, Eqs. (5.17) and (5.18) suggest that the electric polarization density is directed along the $\hat{\mathbf{z}}$ axis, while the direction of the magnetic polarization density is enclosed within the XY-plane. Therefore, neglecting the cross-polar components of the scattered field produced by a thin wire results in negligible polarization densities oriented along the directions of such cross-polar components. In this manner, the analysis based on cylindrical harmonics predicts a uniaxial permittivity tensor

$$\overline{\overline{\boldsymbol{\varepsilon}}}_{\mathrm{eff}} = \varepsilon_0 \overline{\overline{\mathbf{I}}}_t + \varepsilon_{\mathrm{eff}} \widehat{\mathbf{z}} \tag{5.19}$$

with

$$\overline{\overline{\mathbf{I}}}_t = \widehat{\mathbf{x}}\widehat{\mathbf{x}} + \widehat{\mathbf{y}}\widehat{\mathbf{y}} \tag{5.20}$$

as well as a gyrotropic permeability tensor

$$\overline{\overline{\boldsymbol{\mu}}}_{\mathrm{eff}} = \begin{bmatrix} \mu_{\mathrm{eff}} & j\mu_{\mathrm{eff},t} & 0 \\ -j\mu_{\mathrm{eff},t} & \mu_{\mathrm{eff}} & 0 \\ 0 & 0 & \mu_0 \end{bmatrix} \tag{5.21}$$

However, for $\mu_t = 0$ it can be found that $M_1 = M_{-1}$ recovering a uniaxial permeability tensor.

It was demonstrated in Chapter 2 that the $n = 0$ mode is sufficient to accurately describe the response of the ferromagnetic wires. Strikingly, such result leads to the conclusion that the permeability of composites of ferromagnetic wires is negligible. Therefore, composites of ferromagnetic wires belong to the class of artificial dielectrics. Note that this conclusion does not mean that the magnetic properties of the wires have no impact on the constitutive parameters of the artificial electromagnetic material. Conversely, the magnetic properties of the wires determine the frequency dispersion of the effective permittivity of the artificial electromagnetic material. That is to say, composites of ferromagnetic wires are artificial dielectrics with magnetically controlled permittivity.

5.3 Effective Permittivity of Arrays of Ferromagnetic Wires

It was shown in Chapter 2 that a ferromagnetic wire can be modeled as an impedance loaded wire, whose load is determined by the electric and magnetic properties of the ferromagnetic core. Such model has been so far exploited to help understanding the nuances of surface and bulk effects in the scattering by ferromagnetic wires, as well as to explore their fundamental limits. Since artificial electromagnetic materials made of impedance loaded wires have been intensively studied [63, 96–101], the

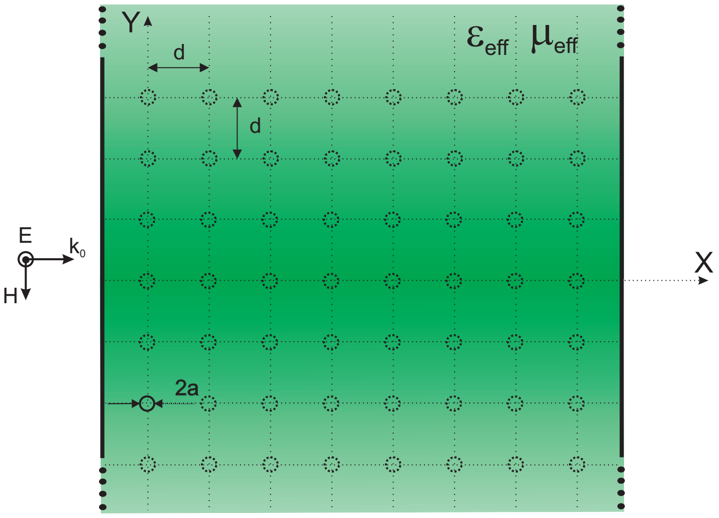

Figure 5.1 – Geometry of the wire array and equivalent material slab.

same model can be adopted to facilitate the homogenization of arrays of ferromagnetic wires. Previous works on the homogenization of arrays of impedance loaded wires concluded that such structures can be modeled with an uniaxial permittivity tensor (which is consistent with the analysis carried out in Section 5.2) and emphasize their spatially dispersive nature. To reduce complexity and to emphasize the role of the effects excited within the wires our analysis is restricted to normal incidence over the dominant polarization, so that spatial dispersion effects can be neglected. Therefore, a square array of parallel wires with interwire spacing d (see Fig. 5.1), is described by a scalar relative permittivity equal to [97]

$$\begin{aligned}\varepsilon_{\text{eff}}(\omega) &= 1 - \frac{1}{\omega\varepsilon_0 d^2}\frac{1}{\omega L - jZ_{\text{w}}} \\ &= 1 - \frac{1}{\omega\varepsilon_0 d^2}\frac{\omega L + X_{\text{w}} + jR_{\text{w}}}{(\omega L + X_{\text{w}})^2 + R_{\text{w}}^2}\end{aligned} \tag{5.22}$$

where

$$L_{\text{array}} = \frac{\mu_0}{2\pi}\ln\left\{\frac{d^2}{4a(d-a)}\right\} \tag{5.23}$$

stands for the quasistatic inductance of one wire per unit length, including the coupling with the other wires of the array [97].

This circuit formulation for the effective permittivity of the ferromagnetic wire is convenient for an intuitive description of the main electromagnetic phenomena. For example, since the wire radius plays a crucial role in the scattering by a single ferromagnetic wire (see Chapter 3), it is expected that it also greatly affects the constitutive parameters of a composite of ferromagnetic wires. Let us examine this fact analyzing the most relevant cases. To begin with, it was found in Chapter 3 that the wire inductance dominates over the other impedance terms for wires with radius much larger than the penetration depth. Similarly, the inductance of the wire within the array L_{array} is the dominant impedance term in (5.22) for such wires, $\omega L_{\text{array}} \gg R_{\text{w}}, |X_{\text{w}}|$. Therefore, the relative effective permittivity in the SE limit asymptotically approaches to

$$\varepsilon_{\text{eff}}(\omega) \simeq 1 - \frac{1}{\varepsilon_0 d^2} \frac{1}{\omega^2 L_{\text{array}}} \tag{5.24}$$

which corresponds to the real and negative permittivity of an array of PEC wires. In other words, there is a negligible penetration of the electromagnetic fields inside thick wires, and the composite approximately behaves as a conventional unloaded wire media. By contrast, the fields are able to penetrate inside the wire as the radius gets smaller, and thus the wire distributed impedance becomes significant, though still smaller than L_{array}. In such a case, and approximating $(\omega L_{\text{array}} + X_{\text{w}})^2 \gg R_{\text{w}}^2$, the relative effective permittivity reduces to

$$\varepsilon_{\text{eff}}(\omega) \simeq 1 - \frac{1}{\omega \varepsilon_0 d^2} \left(\frac{1}{\omega L_{\text{array}} + X_{\text{w}}} + j \frac{R_{\text{w}}}{(\omega L_{\text{array}} + X_{\text{w}})^2} \right) \tag{5.25}$$

Therefore, the magnetic properties of the wire influence the composite permittivity. Specifically, the wire distributed resistance increases the losses of the material, while the wire distributed reactance modulates the real part of the permittivity. In particular, a positive (negative) wire reactance decreases (increases) the negative value of the real part of the permittivity.

For even smaller radii, the wire resistance becomes dominant over the reactive impedance terms, $R_{\text{w}} \gg \omega L_{\text{array}}, |X_{\text{w}}|$, so that the relative effective permittivity is approximately given by

$$\varepsilon_{\text{eff}}(\omega) \simeq 1 - \frac{1}{\omega \varepsilon_0 d^2} \left(\frac{\omega L_{\text{array}} + X_{\text{w}}}{R_{\text{w}}^2} + j \frac{1}{R_{\text{w}}} \right) \tag{5.26}$$

In this case, although the magnetic properties of the wire also influence the composite permittivity, their impact on its dispersion profile is essentially different. Contrary to (5.25), (5.26) reveals that the medium losses are reduced as the wire resistance increases. Moreover, in this case a positive (negative) wire reactance increases (decreases) the negative value of the real part of the permittivity.

Finally, as the wire radii is reduced further and the QS limit is approached, all impedance terms become negligible as compared to the wire distributed resistance, and therefore the effective permittivity simplifies to

$$\varepsilon_{\text{eff}}\left(\omega\right) \simeq 1 - j\frac{1}{\omega\varepsilon_0 d^2}\frac{1}{R_{\text{w}}} \simeq 1 - j\frac{\pi a^2}{d^2}\frac{\sigma}{\omega\varepsilon_0} \tag{5.27}$$

Eq. (5.27) illustrates how in the QS limit the effective permittivity becomes independent of the magnetic properties of the wire, and it corresponds to the permittivity of a conductor with effective conductivity $\sigma_{\text{eff}} = \sigma\frac{\pi a^2}{d^2}$, corresponding the average of the wire conductivity.

In summary, the effective permittivity of an array of ferromagnetic wires exhibits a complex frequency dispersive behavior, which is determined by both the electromagnetic properties of the wires and the geometry of the array. As it happened with the scattering by a single ferromagnetic wire in Section 3.2, the correlation of the composite permittivity with the wire magnetic properties tend to vanish for SE and QS limits, i.e., the correlation is maximized at the radii corresponding to the transition from surface to bulk effects.

To illustrate this conclusion further, Fig. 5.2 represents the frequency domain behavior of the effective permittivity for square arrays of ferromagnetic wires of $50\,\mu$m, $10\,\mu$m, $1\,\mu$m and 100 nm radius. The wires have been modeled with typical Co-rich values [53]: conductivity $\sigma = 5\cdot 10^5\,$S/m, gyromagnetic ratio $\gamma = 2\cdot 10^{11}\,\text{T}^{-1}\text{s}^{-1}$, saturation magnetization $\mu_0 M_{\text{s}} = 0.55\,$T, and magnetic loss factor $\alpha = 0.02$. An effective DC magnetic field $H_{\text{eff}} = 113.45\,$kA/m is assumed, so that the FMR frequency is at 10 GHz and the AFMR frequency is located at approximately 22 GHz. Moreover, the lattice period is set to $d = 2$ mm. Since different radii are studied with the same lattice constant, the density of wires (i.e., number of wires per unit volume) is kept constant, but the filling factor (i.e., percentage of volume occupied by the wires) decrease along with the wire radius. From the standpoint of the effective permittivity, considering smaller lattice periods would only lead to smaller L_{array} values.

For the largest wire radius ($a = 50\,\mu$m, Fig. 5.2(a)) the effective permittivity is dominated by its negative real part, which is the typical response of conductive wire media, and only a small perturbation is observed close to the FMR frequency, i.e., at the frequency where the wire

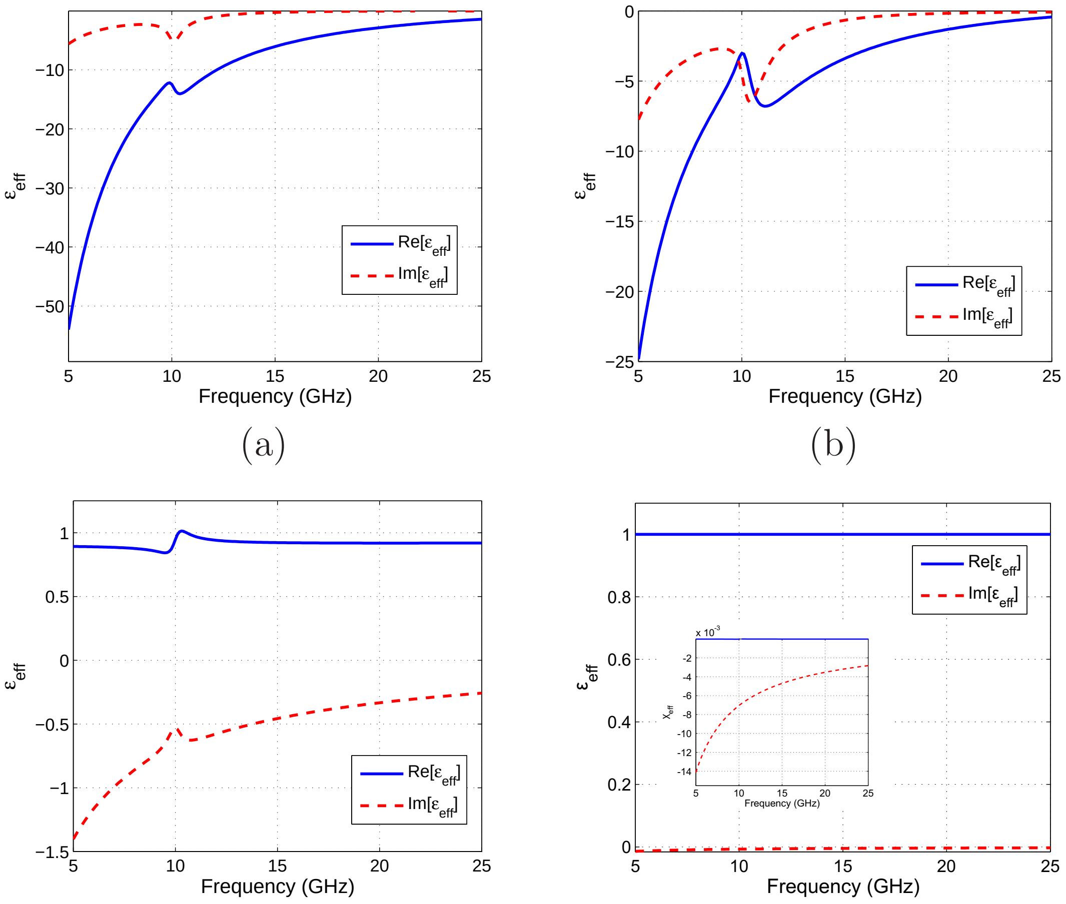

(a) (b)

(c) (d)

Figure 5.2 – Frequency behavior of the effective permittivity of an square array of ferromagnetic wires with lattice constant d = 2 mm and radius of (a) 50 μm, (b) 10 μm, (c) 1 μm and (d) 100 nm.

impedance is the largest. As the wire radius decreases, the influence of the magnetic parameters on the effective permittivity increases, and a resonance is clearly observed for the wire of 10 μm radius close to the FMR frequency (i.e., at 10 GHz). As it was anticipated by (5.25), the material losses increase close to the FMR frequency, and the real part of the effective permittivity oscillates around this point, following a maximum-minimum sequence.

If the radius is further reduced ($a = 1\,\mu$m, Fig. 5.2c), the wire resistance dominates over the array and wire inductances, and the influence of the wire magnetic properties on the frequency dispersion of the effective permittivity is significantly different. Ratifying (5.26), the material losses are minimized at the FMR frequency, and the real part of the permittivity follows a minimum-maximum sequence around this point. Although, the antiresonant behaviour of the real part of the effective permittivity might seem unphysical, recall that the presence of high losses enables this apparently anomalous frequency dispersive behavior.

Finally, the wires operate in the QS limit for radius as small as 100 nm (see Fig. 5.2d), and the composite behaves as an ordinary lossy dielectric, without additional dispersion properties. Due to the small filling factor, the effective permittivity approaches that of vacuum. Therefore, the characteristics of this artificial materials can be better appreciated on the inset of Fig. 5.2d, which represents the effective susceptibility of the array $\chi_{\mathrm{eff}} = \epsilon_{\mathrm{eff}} - 1$. It can be concluded that the effect of the wires in the composite material is dominated by the losses, with the smooth $1/\omega$ frequency dependence of conductive bodies.

5.4 Numerical Validation

While the homogenization approach by itself serves to describe the polarization processes excited within a composite material, it is often expected that it also serves to predict measurable quantities. This section makes use of numerical simulations to validate the homogenization approach as a simplified tool to predict the reflection, transmission and absorption power coefficients that would be measured when an array of ferromagnetic wires is illuminated by a plane wave. In this manner, if the numerical and homogenization approaches converge to the same results, the latter can be adopted to simplify the design of wire-based systems, for example, electromagnetic absorbers based on arrays of ferromagnetic wires.

To this end, the results retrieved by the homogenization approach for a slab of 8 parallel grids of ferromagnetic wires, represented in Fig. 5.1, have been tested against those of a full-wave simulation. As it has been discussed, the simulation of arrays of ferromagnetic wires with commercial softwares is a cumbersome task, due to the complex meshes produced by the extreme geometry of the wires. Therefore, the full-wave simulation has been carried out with a home-made code based on the local field method, following [63, 96]. In essence, the local field in the wires is equal to the addition of the incident field and the interaction field with the other wires of the array, namely, the coupling inside the grid and the coupling with the other grids. The array interactions have been computed by using a Floquet-mode decomposition, taking into account a large number of non-propagating modes ($N = 200$). Once the fields exciting the wires are known, the field in the far zone is a plane wave which can be readily computed as the sum of the plane waves produced by each grid. By doing so, the transmission and reflection power parameters are given by the power carried out by the propagating plane wave in the forward and backward directions, respectively. As for the homogenization approach, once the effective permittivity has been computed as in Section 5.3, the reflection and transmission power parameters for a homogeneous slab can be written in closed form as follows [102]

$$T_{\text{hom}} = \left| \frac{2\eta_{\text{eff}}\eta_0}{j\left(\eta_{\text{eff}}^2 + \eta_0^2\right)\sin\left(k_{\text{eff}}t\right) + 2\eta_{\text{eff}}\eta_0\cos\left(k_{\text{eff}}t\right)} \right|^2 \tag{5.28}$$

$$R_{\text{hom}} = \left| \frac{\eta_{\text{eff}}^2 - \eta_0^2}{\eta_{\text{eff}}^2 + \eta_0^2 - 2j\eta_{\text{eff}}\eta_0\cot\left(k_{\text{eff}}t\right)} \right|^2 \tag{5.29}$$

where t is the slab thickness, and $\eta_{\text{eff}} = \sqrt{\mu_0/\varepsilon_{\text{eff}}}$, $k_{\text{eff}} = \omega\sqrt{\mu_0\varepsilon_{\text{eff}}}$ are the medium impedance and propagation constant inside the material slab, respectively. For both, numerical and homogenization approaches, the absorption power coefficient is computed by enforcing energy conservation

$$A = 1 - T - R \tag{5.30}$$

Fig. 5.3 shows the comparison of the transmission, reflection and absorption power coefficients calculated with the full-wave method and those obtained for a homogeneous material slab with dielectric constant ε_{eff} and thickness $t = 8d$. Following the previous examples, the lattice constant equals 2 mm, and wire radii of 50 μm, 10 μm, 1 μm and 100 nm have been considered. It can be concluded that there is a good agreement between the results obtained with both methods for all the considered radii, validating the homogenization approach.

Let us also use this simulation to examine how the wire radius affects the transmission, reflection and absorption power parameters of the slab. For example, for slabs with composed of relatively thick wires (i.e., $a = 50\,\mu$m and $a = 10\,\mu$m, corresponding to Figs. 5.3(a) and 5.3(b), respectively) the absorption coefficient is characterized by a peak close to the FMR frequency and a minimum at the AFMR frequency, which corresponds with a minimum and a maximum of reflection, respectively. Conversely, the transmission coefficient is close to zero in the whole frequency range. In addition, the smaller the radius the higher the absorption peak. It is worth mentioning that this absorption peak can be activated, deactivated and shifted in frequency by applying a DC magnetic field, DC currents or mechanical stresses, and thus a potential application of these artificial materials is in the design of reconfigurable electromagnetic absorbers.

Below the SE limit, the power coefficients are characterized by broadband absorption coefficients, where the main contribution comes from the finite conductivity of the wires, and a pronounced transmission, due to smaller filling factor than with previous wires. Moreover, the slab with wires of $1\,\mu$m radius exhibits a minimal of absorption and reflection at the FMR frequency, corresponding with a maximum of transmission. Interestingly, the experiments reporting transmission windows in arrays of ferromagnetic wires [31, 36, 52, 53] make use of wires with radii ranging from $1.5\,\mu$m to $3.5\,\mu$m. Thus, our analysis suggests that those experimental data can be understood as the result of the frequency dispersion of the effective permittivity produced by the FMR excited in the wires, rather than a DNG metamaterial behavior.

Finally, the transmission, reflection and absorption power coefficients present a flat spectra for the slab of wires with 100 nm radius. Again, the magnetic properties of the wire do not affect the results in the QS limit. This case corresponds to the propagation through a very diluted, almost matched ($\varepsilon_{\mathrm{eff}} \simeq \varepsilon_0 - j\delta\varepsilon$ with small $\delta\varepsilon$) lossy medium, and therefore it is characterized by high transmission, weak absorption and almost negligible reflection. Note that the absorption power coefficient would increase monotonically along with the length of the slab, which suggests that composites made of diluted mixtures of metallic pieces with dimensions much smaller than the penetration depth can be engineered to create wideband

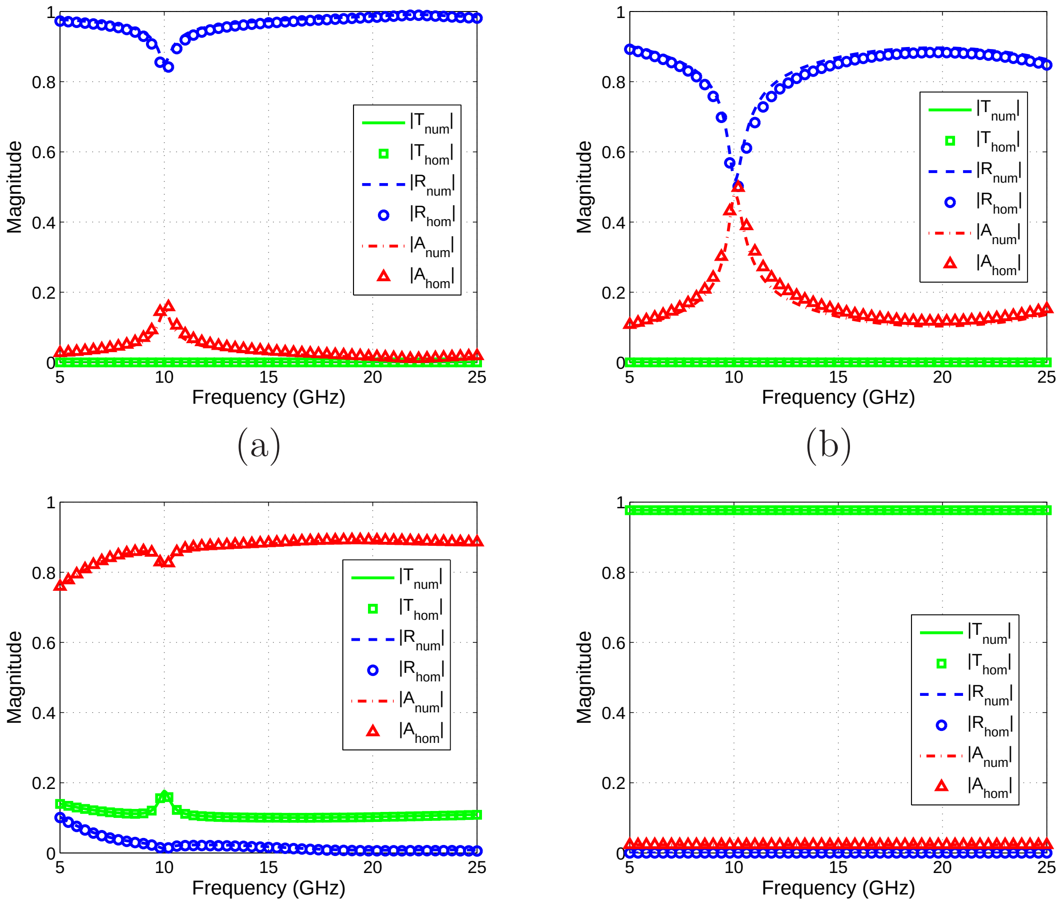

(a) (b) (c) (d)

Figure 5.3 – Comparison of the transmission, absorption and reflection power coefficients obtained for the equivalent material slab and the numerical simulation of the array of wires, for wire radius of (a) 50 μm, (b) 10 μm, (c) 1 μm and (d) 100 nm.

absorbers. However, they would require a electrically large thickness to extinguish the incoming wave, and no benefit would be extracted from the magnetic properties of the wires.

5.5 Conclusions

Artificial electromagnetic materials based on composite of ferromagnetic wires have been investigated in this chapter. In particular, wire media composed of ferromagnetic wires. First of all, the decomposition based on cylindrical harmonics has been employed to analyze the polarization densities excited within a composite of ferromagnetic wires. It has been concluded that such composites are characterized by an uniaxial permittivity tensor and a gyrotropic permeability tensor. However, it has also been found that the thin wire approximation, i.e., taking only the $n = 0$ cylindrical harmonic, is equivalent to neglecting the material permeability. Despite this fact, the magnetic properties of the wires are play a major role, since they influence the effective permittivity of these composites. Thus, composites of ferromagnetic wires belong to the class of artificial dielectric materials with magnetically controlled permittivity.

Moreover, the circuit model introduced in Chapter 2 has been used to link the studied composites to previous studies on wire media based on impedance loaded wires [63, 96–101]. It is then illustrated how the occurrence of the FMR adds extra complexity to the frequency dispersive behavior of wire media, and how different phenomena arise as a function of the relative values of the wire radius compared to the skin depth.

Finally, the homogenization procedure has been validated via numerical simulations, and good agreement is found between the results of numerical and homogenization approaches. This fact demonstrates the usefulness of the homogenization procedure for the design of ferromagnetic wires based systems. For example, the numerical results suggest the use of slabs of ferromagnetic wires as narrowband reconfigurable absorbers (exploiting FMR resonance effect) and/or wideband absorbers (exploiting the reduced conductivity of amorphous wires).

Chapter 6

Artificial Impedance Surfaces based on Ferromagnetic Wires

6.1 Introduction

As schematically depicted in Fig 6.1, the presence of a ferromagnetic wire alters the reflection from a ground plane when it is illuminated by a plane-wave. On the one hand, a single ferromagnetic wire disperses the incident plane-wave due to scattering and absorption processes. On the other hand, the response is bound to be an plane-wave for a sufficiently dense ensemble of wires. In such a case, the presence of ferromagnetic wires is transferred to changes on the magnitude and phase of the reflected wave, which can be regarded as an alteration of the boundary conditions on the ground plane surface.

Artificial impedance surfaces [103,104], i.e., artificial surfaces with engineered surface impedance, are of great practical interest, as they offer a lot of design freedom in antenna and other microwave applications. Although metallic structures are very convenient from a structural, mechanical and/or shielding point of view, the perfect electric boundary conditions are often a problem for the antenna engineer. The obvious reasons are that metallic surfaces reflect all incident electromagnetic power, thus, exhibit large radar cross sections (RCS), and that electric radiating sources close to the surface are cancelled out. Therefore, artificial surfaces are employed to produce more suitable boundary conditions. Applications of artificial impedance surfaces include low-profile antennas based on high-impedance

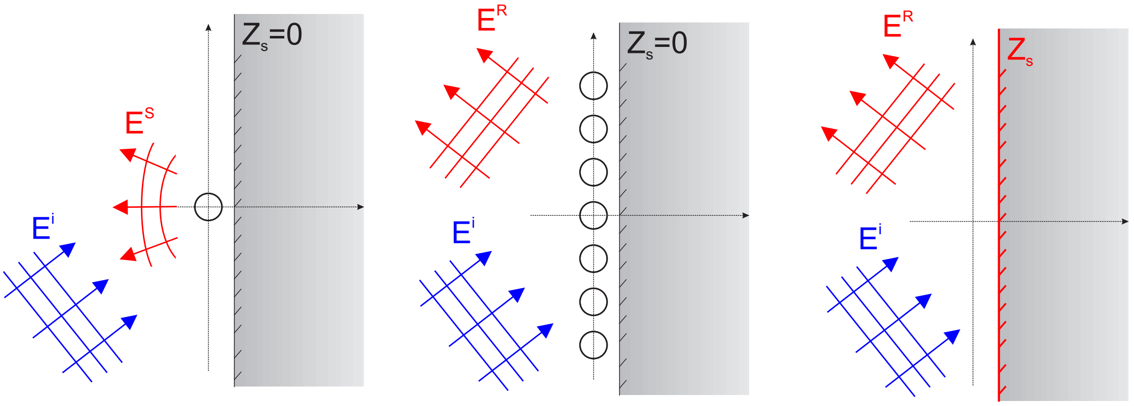

Figure 6.1 – Ferromagnetic wires in the proximity of the ground plane and equivalent plane with modified surface impedance.

surfaces [103,105,106] (HISs), electromagnetic absorbers [107,108], reflectarrays [109,110], frequency selective surfaces [111] and complex antiradar systems [112].

Most state-of-the-art artificial impedance surfaces are designed based on grids of conductive elements resonating in the proximity of a ground plane. Typically, a transmission line approach [104, 113] is employed to design arrays of conductive patches [107], dipoles [114] or more complex shapes in which a strong electric current is excited. This chapter investigates the development of artificial impedance surfaces based on ferromagnetic wires. Due to the losses inherent to ferromagnetic wires, the development of absorbers will be emphasized. In addition, it will be shown how the wire ferromagnetic properties and the strong reactive fields due to interactions of wires with the ground plane can be tuned to provide the necessary resonance to excite a strong current in the wires, even in the proximity of the ground plane.

Moreover, artificial impedance surfaces present stringent bandwidth-profile limits [115] due to their resonant nature. To overcome these limits, the designs usually include circuitry (e.g. varactor diodes) to produce reconfigurable bandwidths [116]. In addition, circuital elements are also employed for beam-steering reflectarrays [109, 110]. In this regard, the proposed ferromagnetic wire-based surfaces can be reconfigured through DC magnetic fields [34], DC electric currents [36] and/or mechanical stresses [40], thus avoiding the complexity of integrating circuital elements and their correspondent feeding networks.

6.2 Analytical Solution

The geometry of the problem is schematically depicted in Fig. 6.2: a grid of parallel wires of radius a, with constant separation between the wires d, is placed at a distance h from a metallic ground plane. Under the thin-wire approximation, the electric field produced by each wire when illuminated by a plane wave with the wave vector $\mathbf{k} = k_{\mathrm{x}}\widehat{\mathbf{x}} + k_{\mathrm{y}}\widehat{\mathbf{y}} + k_{\mathrm{z}}\widehat{\mathbf{z}}$ only has a z component equal to [63]

$$E_z^{\mathrm{w}} = \frac{-\eta_0 k_r^2}{4k_0}\frac{E_{\mathrm{z}}^{\mathrm{loc}}}{\alpha^{-1}} H_0^{(2)}\left(k_r r\right) e^{-jk_{\mathrm{z}}z} \tag{6.1}$$

where $k_0^2 = k_{\mathrm{x}}^2 + k_{\mathrm{y}}^2 + k_{\mathrm{z}}^2 = k_r^2 + k_{\mathrm{z}}^2$, $E_{\mathrm{z}}^{\mathrm{loc}}$ stands for the z component of the local electric field on the wire surface, and α^{-1} for the wire polarizability given by [63]

$$\alpha^{-1} = \frac{k_r^2}{k_0^2} Z_{\mathrm{w}} + \frac{\eta_0 k_r^2}{4k_0} H_0^{(2)}\left(k_r a\right) \tag{6.2}$$

Here Z_{w} is the wire distributed impedance and a is the wire radius. Thus, the field produced by the grid is found by adding the fields produced by

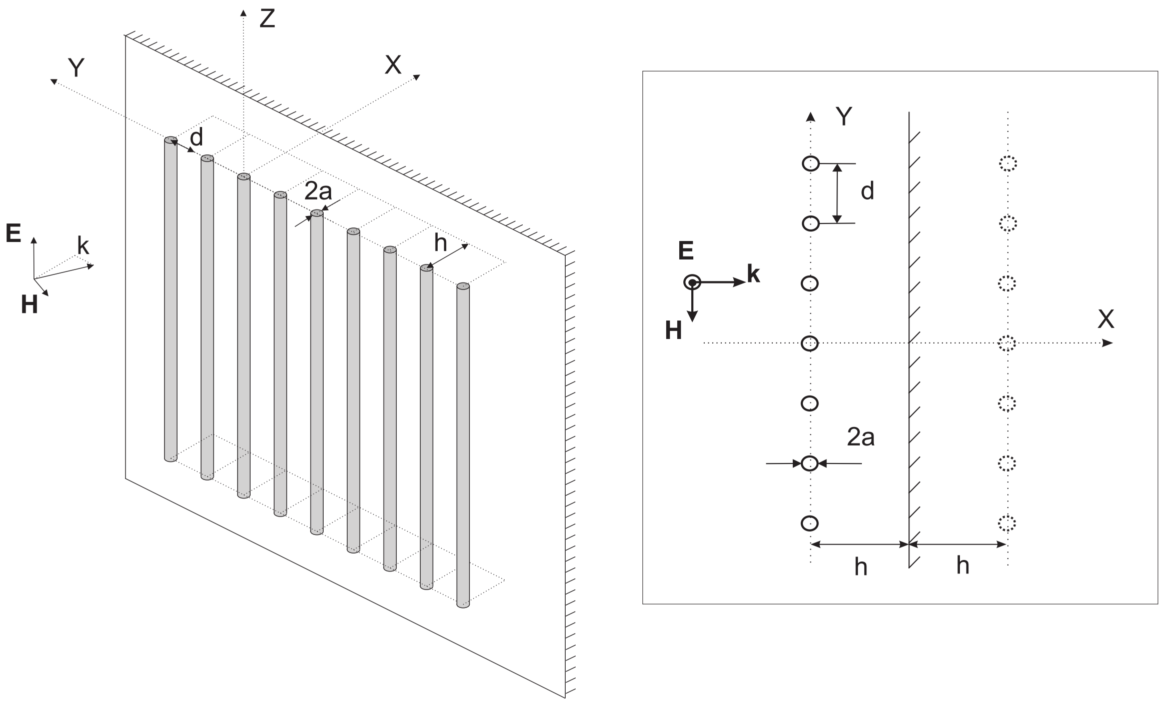

Figure 6.2 – Geometry of the problem: a grid of parallel wires of radius a, with constant separation between the wires d, is placed at a distance h from a metallic ground plane.

all the wires:

$$E_z^{\mathrm{grid}} = \frac{-\eta_0 k_r^2}{4k_0} \frac{E_{\mathrm{z}}^{\mathrm{loc}}}{\alpha^{-1}} \sum_{s=-\infty}^{\infty} H_0^{(2)}\left(k_r R_s\right) e^{-jk_{\mathrm{y}} sd} e^{-jk_{\mathrm{z}} z} \tag{6.3}$$

where $R_s^2 = x^2 + (y - sd)^2$. The Hankel summation can be simplified by using the Floquet mode representation [117]:

$$\sum_{s=-\infty}^{\infty} H_0^{(2)}\left(k_r R_s\right) e^{-jk_{\mathrm{y}} sd} e^{-jk_{\mathrm{z}} z} = \frac{2}{d} \sum_{m=-\infty}^{\infty} \frac{e^{-j\left(k_m |x| + \left(k_{\mathrm{y}} + \frac{2\pi m}{d}\right) y + k_{\mathrm{z}} z\right)}}{k_m} \tag{6.4}$$

where $k_m^2 = k_r^2 - \left(k_{\mathrm{y}} + \frac{2\pi m}{d}\right)^2$ stands for the propagation constant of the m-th Floquet mode.

The fields produced by the grid depend on the local field on the surface of the wires. By definition, the local field is equal to the addition of the incident field, the grid auto-interaction and the interaction with the ground plane:

$$E_{\mathrm{z}}^{\mathrm{loc}} = E_{\mathrm{z}}^{\mathrm{inc}} \left(1 - e^{-jk_{\mathrm{x}} 2h}\right) - \frac{\eta_0 k_r^2}{4k_0} \frac{E_{\mathrm{z}}^{\mathrm{loc}}}{\alpha^{-1}} \left(G_{\mathrm{grid}} + G_{\mathrm{imag}}\right) \tag{6.5}$$

and thus

$$E_{\mathrm{z}}^{\mathrm{loc}} = \frac{E_{\mathrm{z}}^{\mathrm{inc}} \left(1 - e^{-jk_{\mathrm{x}} 2h}\right)}{1 + \frac{\eta_0 k_r^2}{4k_0} \frac{1}{\alpha^{-1}} \left(G_{\mathrm{grid}} + G_{\mathrm{imag}}\right)} \tag{6.6}$$

where G_{grid} and G_{imag} stand for the grid auto-interaction constant and the interaction constant with the ground plane, respectively. The grid auto-interaction constant defines the influence of the rest of the grid wires:

$$G_{\mathrm{grid}} = \sum_{s \neq 0} H_0^{(2)}\left(k_r \left|sd\right|\right) \tag{6.7}$$

On the other hand, the interaction constant with the ground plane is given by the fields produced by the image of the grid in the ground plane:

$$G_{\mathrm{imag}} = - \sum_{s=-\infty}^{\infty} H_0^{(2)}\left(k_r \sqrt{(2h)^2 + (sd)^2}\right) \tag{6.8}$$

Due to the presence of the ground plane, all electromagnetic field is either absorbed or reflected. Furthermore, the reflected field is found as the addition of the reflection of the incident wave in the metallic plane, the field produced by the grid and the field produced by the image of the grid in the ground plane:

$$
\begin{gathered}
E_{\mathrm{z}}^{R} = -E_{\mathrm{z}}^{\mathrm{inc}} e^{j\boldsymbol{k}_r\mathbf{r}} e^{-jk_{\mathrm{x}}2h} - \frac{\eta_0 k_r^2}{2k_0 d}\frac{E_{\mathrm{z}}^{\mathrm{loc}}}{\alpha^{-1}} \times \\
\sum_{m=-\infty}^{\infty} \frac{e^{j\left(k_m x + \left(k_{\mathrm{y}} + \frac{2\pi m}{d}\right) y\right)}}{k_m} \left(1 - e^{-jk_m 2h}\right)
\end{gathered}
\tag{6.9}
$$

where $\boldsymbol{k}_r\mathbf{r} = k_{\mathrm{x}}\mathrm{x} + k_{\mathrm{y}}\mathrm{y}$. Note that a factor $\exp\left(-jk_{\mathrm{z}}\mathrm{z}\right)$ will be omitted hereafter. If the separation between the wires is much smaller than the wavelength ($d \ll \lambda$), only the $n = 0$ mode propagates, and the reflected field in the far zone simplifies to a plane wave. Thus, the reflection coefficient can be readily found to be equal to

$$
R = e^{jk_x 2h}\frac{E_{\mathrm{z}}^{\mathrm{R}}}{E_{\mathrm{z}}^{\mathrm{inc}}} = -1 + \frac{2\eta_0 k_r^2}{k_0 k_{\mathrm{x}} d} \cdot \frac{\sin^2\left(k_{\mathrm{x}} h\right)}{\alpha^{-1} + \frac{\eta_0 k_r^2}{4k_0}\left(G_{\mathrm{grid}} + G_{\mathrm{imag}}\right)}
\tag{6.10}
$$

Consistently, R is equal to -1 when no field is produced by the grid. Moreover, the wave produced by the grid tends to vanish with a $\sin^2\left(-\right)$ trend as the separation between the grid and the ground plane decreases.

6.3 Resonant Absorbers

Although (6.10) illustrates how the field produced by the wires is cancelled out as the grid becomes closer to the ground plane, under certain resonant conditions strong currents can be excited in the wires even for small h. In such a cases, ferromagnetic wires could be employed to design low-profile absorbers.

6.3.1 Resonant Condition

Let us first derive the conditions needed to create the resonance. For the sake of simplicity, consider the reflection coefficient under normal incidence ($\mathbf{k} = k_0\widehat{\mathbf{x}}$)

$$
R = -1 + \frac{2\eta_0}{d}\frac{\sin^2\left(k_0 h\right)}{\alpha^{-1} + \frac{\eta_0 k_0}{4}\left(G_{\mathrm{grid}} + G_{\mathrm{imag}}\right)}
\tag{6.11}
$$

Apparently, the resonant condition is met when the denominator approaches zero

$$\alpha^{-1} + \frac{\eta_0 k_0}{4}\left(G_{\text{grid}} + G_{\text{imag}}\right) \to 0 \tag{6.12}$$

Let us analyze (6.12) term by term. To begin with, under the thin-wire approximation ($k_0 a \ll 1$) the wire susceptibility (6.2) simplifies to

$$\alpha^{-1} \simeq Z_{\text{w}} + \frac{\eta_0 k_0}{4}\left\{1 + j\frac{2}{\pi}\left[\log\left(\frac{2}{k_0 a}\right) - \gamma\right]\right\} \tag{6.13}$$

where $\gamma = 0.5772$. The real part of the second term accounts for the scattering resistance, and the imaginary part is an inductive term that increases logarithmically as the wire radius, a, decreases. Secondly, the grid auto-interaction, $\eta_0 k_0/4 \cdot G_{\text{grid}}$, was introduced in eq. (6.7). It can be rewritten by means of the Poisson rule with singularity cancellation as [96]

$$\frac{\eta_0 k_0}{4} G_{\text{grid}} = \frac{\eta_0 k_0}{4}\left\{\frac{2}{k_0 d} - 1 + j\frac{2}{\pi}\left[\log\left(\frac{k_0 d}{4\pi}\right) + \gamma + \frac{\pi}{d}\sum_{m\neq 0}\left(\frac{1}{q_m} - \frac{d}{2\pi\left|m\right|}\right)\right]\right\} \tag{6.14}$$

with $q_m^2 = (2\pi m/d)^2 - k_0^2$, $q_m \epsilon \mathbb{R}^+$. The real part of the above expression is exact, being composed by a $1/k_0 d$ term which represents the plane-wave created by the grid, and a negative term that compensates the radiation resistance of a single wire. The imaginary part is negative. Physically, it is due to the mutual inductance with the other wires, which decreases the total inductance.

Finally, the wire-ground plane interaction is given by the field created by the images of the grid in the ground plane, as in eq. (6.8). Again, the Hankel series simplifies to a Floquet-mode representation

$$\frac{\eta_0 k_0}{4} G_{\text{imag}} = -\frac{\eta_0 k_0}{2}\sum_{m=-\infty}^{\infty}\frac{e^{-j2k_m h}}{k_m d} \tag{6.15}$$

Although this formulation might not seem convenient due to the large number of evanescent modes to be taken into account for a small h, it nevertheless gives a good insight to the contributions to the real and imaginary parts. In particular, for $k_0 d \ll 1$ only the $m = 0$ mode is propagating and the factor reduces to

$$\frac{\eta_0 k_0}{4} G_{\mathrm{imag}} = \frac{\eta_0 k_0}{2} \left[\frac{-\cos\left(2k_0 h\right)}{k_0 d} + j \left(\frac{\sin\left(2k_0 h\right)}{k_0 d} - 2 \sum_{m=1}^{\infty} \frac{e^{-2q_m h}}{q_m d} \right) \right] \tag{6.16}$$

On the one hand, the real part is a plane wave component that tends to cancel the wave produced by the grid as h decreases. On the other hand, the imaginary part has a positive contribution from a plane wave factor and a negative factor originated by the coupling with evanescent Floquet modes. The former vanishes as the grid becomes closer to the ground plane, while the latter is augmented along with the separation between wires and increases as the grid becomes closer to the ground plane.

Inserting (6.13), (6.14) and (6.16), into (6.12), and taking the real part, the real part of the resonant condition takes form

$$\mathrm{Re} \left[\alpha^{-1} + \frac{\eta_0 k_0}{4} \left(G_{\mathrm{grid}} + G_{\mathrm{imag}} \right) \right] = R_{\mathrm{w}} + \frac{\eta_0}{d} \sin^2\left(k_0 h\right) \tag{6.17}$$

Thus, even in the lossless case the real part of the denominator of eq. (6.11) is only zero at the points where the numerator also vanishes, which ensures $|R| = 1$ for the lossless case.

6.3.2 Reflection Coefficient at the Resonance

Let us assume that the wires are loaded with a reactance per unit length, X_{w}, that cancels out the imaginary part of the denominator of (6.11). Then, the reflection coefficient equals to

$$R = -1 + \frac{2\sin^2\left(k_0 h\right)}{\frac{d}{\eta_0} R_{\mathrm{w}} + \sin^2\left(k_0 h\right)} \tag{6.18}$$

This shows that the magnitude and phase of the reflection coefficient can be controlled by changing the wire resistance per unit length. For example, a high-impedance boundary ($R = 1$) is obtained with $R_{\mathrm{w}} = 0$, while a perfect absorber boundary ($R = 0$) is obtained with $R_{\mathrm{w}} = \eta_0 / d \cdot \sin^2\left(k_0 h\right)$, and the trivial case of a PEC boundary ($R = -1$) with $R_{\mathrm{w}} \to \infty$.

6.3.3 Reactance for the Resonant Condition

The wire reactance per unit length needed to satisfy the resonant condition is found by gathering the imaginary terms of (6.13), (6.14) and (6.16):

$$X_\mathrm{w} = \frac{-\omega\mu_0}{2}\left[\frac{1}{\pi}\log\left(\frac{d}{2\pi a}\right) + \sum_{m\neq 0}\left(\frac{1}{q_m d} - \frac{1}{2\pi\,|m|}\right)\right. \\ \left. + \frac{\sin(2k_0 h)}{k_0 d} - 2\sum_{m=1}^{\infty}\frac{e^{-2q_m h}}{q_m d}\right] \tag{6.19}$$

X_w is a complex function of the wire and grid geometry. In essence, the wire distributed reactance must compensate the grid inductance (plus its higher order interacting terms), as well as the inductance produced by ground plane (plus higher order terms coming from evanescent, reactive coupling). Therefore, it is negative (capacitive) and its magnitude decreases as the grid becomes sparser ($d\uparrow$) and closer to the ground plane ($h\downarrow$) due to the coupling with evanescent Floquet modes. This is illustrated in Fig. 6.3, which depicts the magnitude X_w/ω, for $a = 0.001\lambda$, with wire separations ranging from 0.01λ to 0.5λ and distances to the ground plane of 0.01λ, 0.02λ, 0.05λ and 0.1λ.

Moreover, (6.19) reveals that the frequency domain behavior of the required load approximately follows a linear progression with a negative slope, i.e., it is a negative inductor. Unfortunately, the implementation of such load requires from non-Foster elements [118], and any passive implementations will lead to a limited bandwidth. However, this approximately frequency linear progression can also be considered a great advantage: the system is robust against tolerances of the loads, and the design of reconfigurable loads, as those provided by ferromagnetic wires, is simple.

6.3.4 Feasibility of the Load

Let us analyze potential implementations of the required wire impedance. According to Fig. 6.3, the wire reactance must provide values of the order of $X_\mathrm{w}/\omega \sim \mu\Omega\mathrm{s/m}$. For example, if the resonance is placed at 10 GHz, the value of the wire reactance must be of the order of $X_\mathrm{w} \sim 2\pi\ \mathrm{k}\Omega/\mathrm{m}$. It can be concluded from Fig. 3.2 that ferromagnetic wires can easily provide the necessary reactive loading.

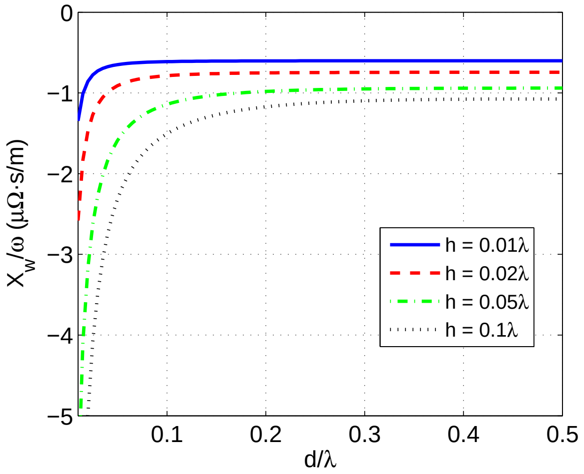

Figure 6.3 – Ratio of the reactance per unit length required to satisfy the resonant condition and angular frequency, for a grid of wires with $a = 0.001\lambda$ radius, distance to the ground plane of 0.01λ, 0.02λ, 0.05λ and 0.1λ, and separation between wires ranging from 0.01λ to 0.5λ.

However, the losses of the wires could be too high to sustain the resonance. In particular, Fig. 3.2 also reveals that $R_\mathrm{w} > X_\mathrm{w}$ for conductive ferromagnetic wires. Therefore, if the resistance required for a perfect absorbing boundary, i.e., $R_\mathrm{w} = \eta_0/d \cdot \sin^2(k_0 h)$, is smaller than the reactance required to enforce the resonance, i.e., (6.19), it should be concluded that the studied ferromagnetic wires are not suitable for the design of resonant absorbers. In fact, bearing in mind that the resistance required for a perfect absorbing boundary is $R_\mathrm{w} = \eta_0/d \cdot \sin^2(k_0 h)$ (i.e., it decays as h^2 for small h), it appears that the resistance must be smaller than the reactance. This intuition can be tested numerically. To this end, Fig. 6.4 depicts the comparison between the required resistance and reactance to achieve perfect absorption for all the cases studied in Fig. 6.3. The figures illustrates how the resistance required for maximal absorption is indeed smaller than the reactance required to enforce the resonance. Regretfully, it must be concluded that although ferromagnetic wires can provide the necessary reactive loads to enforce the resonance, the resistance associated to such reactive loads are too high to produce a perfect absorbing boundary.

On the bright side, other wire-based implementations could lead to more successful designs. For example, Fig. 6.5 gathers two alternatives: conductive wires lumped elements, and conductive wires with a non-conductive magnetic coatings.

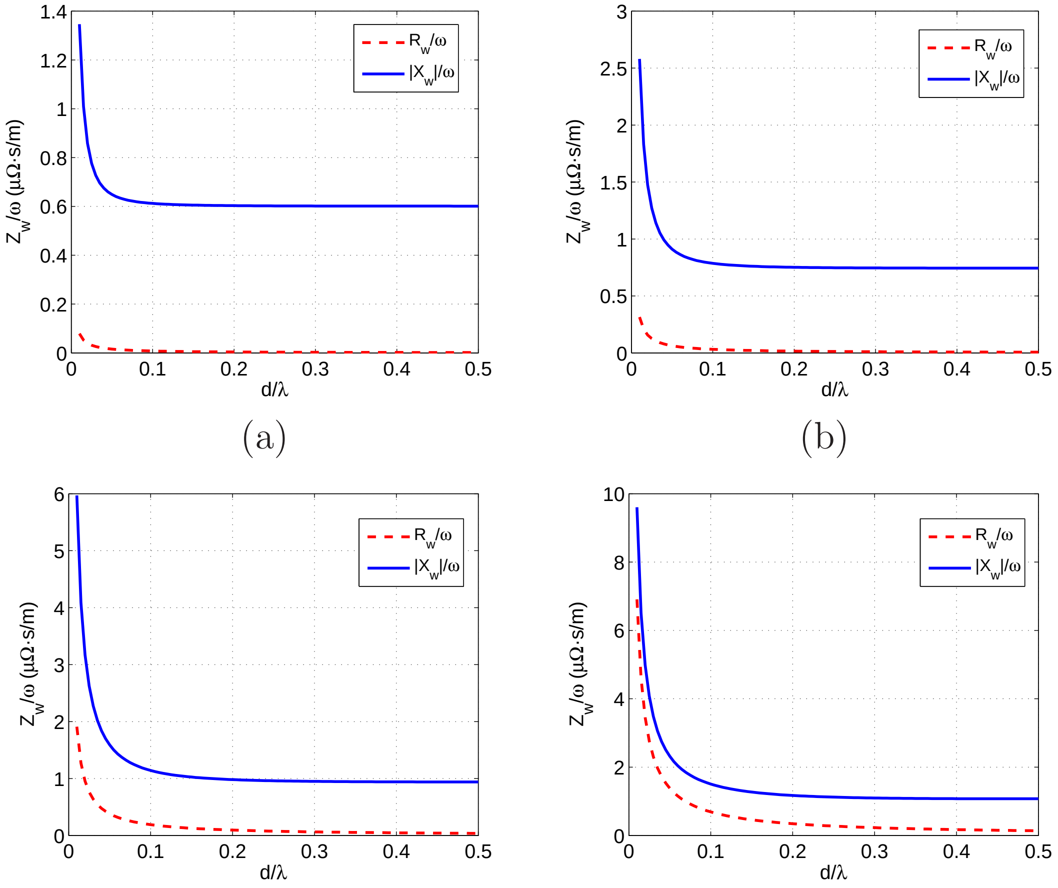

(a) (b)

(c) (d)

Figure 6.4 – Reactance and resistance per unit length required to satisfy the resonant condition divided by angular frequency, for a grid of wires with $a = 0.001\lambda$ radius, distance to the ground plane of (a) 0.01λ, (b) 0.02λ, (c) 0.05λ and (d) 0.1λ, and separation between wires ranging from 0.01λ to 0.5λ.

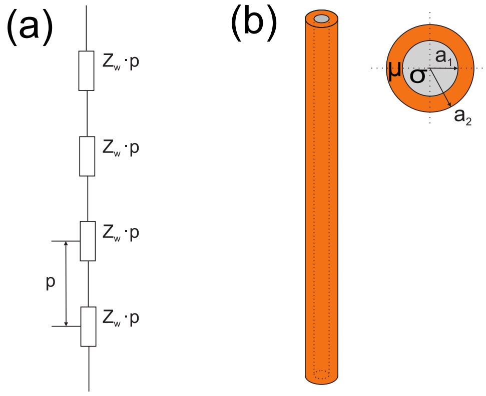

Figure 6.5 – Potential implementations of impedance loaded wires: (a) lumped elements, (b) conductive wires with magnetic coating.

In the first place, impedance loaded wires can be implemented by periodically arranging lumped elements in conductive wires (see Fig. 6.5(a)). Note that this does not necessarily imply the use of circuit elements, since small variations on the wire geometry might be sufficient (i.e. small cuts on the wires instead of capacitors). In particular, a capacitance C, distributed with the period p, provides a distributed impedance $Z_C = -j/(\omega C p)$, so that the required capacitance C is also directly proportional to the frequency of operation. As an example, the required capacitance for a periodicity of $p = \lambda/10$, $a = 0.001\lambda$, $h = 0.01\lambda$ and $d = 0.1\lambda$ is of 1.38 pF at 1 GHz, 0.138 pF at 10 GHz... Therefore, it is possible to satisfy the resonant condition with realistic loads.

Secondly, note that the excess of losses in ferromagnetic wires comes from the fact that magnetic material loading and conduction currents are embedded on the same physical space. In other words, permeability and conductivity are gathered in the same medium. Therefore, if the field inside the wire is augmented to increase the influence of its permeability, ohmic losses increase at the same time. This situation can be solved by placing the electric and magnetic materials of the wires in different layers, for example, covering a conductive wire with a magnetic coating (see Fig. 6.5(b)).

In such a case, the wire distributed impedance can be found by including the scattering coefficients of a coated cylinder [119], into (2.40), which leads to the closed form expression

$$Z_{\mathrm{w}} = \frac{j\eta_2}{2\pi a_2} \frac{J_0(k_2 a_2) + T_1 \cdot H_0^{(2)}(k_2 a_2)}{J_0'(k_2 a_2) + T_1 \cdot H_0'^{(2)}(k_2 a_2)} \tag{6.20}$$

with

$$T_1 = \frac{\eta_1 J_0(k_1 a_1) J_0'(k_2 a_1) - \eta_2 J_0'(k_1 a_1) J_0(k_2 a_1)}{\eta_2 J_0'(k_1 a_1) H_0^{(2)}(k_2 a_1) - \eta_1 J_0(k_1 a_1) H_0'^{(2)}(k_2 a_1)} \tag{6.21}$$

where a_1 and a_2 are the internal and external radius, respectively, while k_1 and η_1, and k_2 and η_2, stand for the propagation constant and medium impedance inside the conductive wire and magnetic coating, respectively. More interestingly, if we take asymptotic limits for a thin wire $k_0 a_2 \ll 1$, composed by an electrically small coating $k_2 a_2 \ll 1$, $k_2 a_1 \ll 1$ and a good conductor core $k_1 a_1 \gg 1$ (with $k_1'' a_1 \gg 1$), the wire distributed impedance can be written as follows

$$Z_{\mathrm{w}} = j\omega\frac{\mu_2}{2\pi}\ln\left(\frac{a_2}{a_1}\right) + \frac{1}{2\pi a_1}\frac{1+j}{\sqrt{2}}\sqrt{\frac{\omega\mu_1}{\sigma}} \tag{6.22}$$

Intuitively, (6.22) is composed by two addends corresponding to the loading produced by the magnetic coating and the conducting core, respectively. The former addend is a function of the coating permeability, and it can be either inductive ($\mathrm{Re}\left[\mu_2\right] > 0$) or capacitive ($\mathrm{Re}\left[\mu_2\right] < 0$), while the magnetic losses of the coating increase the distributed resistance of the wire. The latter addend is produced by the finite conductivity of the metallic core. Naturally, this results in an increase of the wire distributed resistance, and, more surprisingly, in additional inductive loading. This behavior can be ascribed to the electromagnetic energy stored within the metallic core, not present in a PEC wire.

As an example, let us consider a wire consisting of a copper core ($\sigma = 6.7{\cdot}10^7\,\mathrm{S/m}$, $\mu_1 \simeq \mu_0$), coated by an insulating YIG (Yttrium Iron Garnet) magnetic layer, characterized by [92]: $\mu_0 M_s = 0.176\,\mathrm{T}$, $\alpha = 0.005$, $H_k \simeq 0\,\mathrm{kA/m}$, $\gamma = 2.088 \times 10^{11}\,\mathrm{T^{-1}s^{-1}}$, and $\varepsilon_2 = 15\,(1 - j0.001)\,\varepsilon_0$. Fig. 6.6 represents the wire distributed impedance at a frequency of 10 GHz as a function of the DC magnetic field acting on the wire. The radius of the copper core has been set to $a_1 = 0.001\lambda$, and thicknesses of the magnetic layer equal to $0.05a_1$ (Fig. 6.6(a)) and $0.1a_1$ (Fig. 6.6(b)) have been represented. Recall that, at 10 GHz, the reactance required to satisfy the resonant condition is of the order of $X_{\mathrm{w}} \sim 2\pi\,\mathrm{k\Omega/m}$. Therefore, it is apparent from Fig 6.6 that coatings as thin as $0.05a_1$ and $0.1a_1$ are sufficient to provide the required reactance and, at the same time, feature a significantly smaller resistance.

In summary, it has been found that the ferromagnetic wires considered in the dissertation are able to provide the necessary reactive loads to excite the resonance of a grid of wires in the proximity of a ground plane. However, the losses associated to such reactives loads have been found too high to develop perfect absorbing boundaries. Nevertheless, alternative technologies such as conductive wires with lumped elements and conductive wires with magnetic coatings can overcome such difficulty. The performance of these implementations is considered in more detail in Appendix C. Hybrid implementations of all the aforementioned options could also be considered.

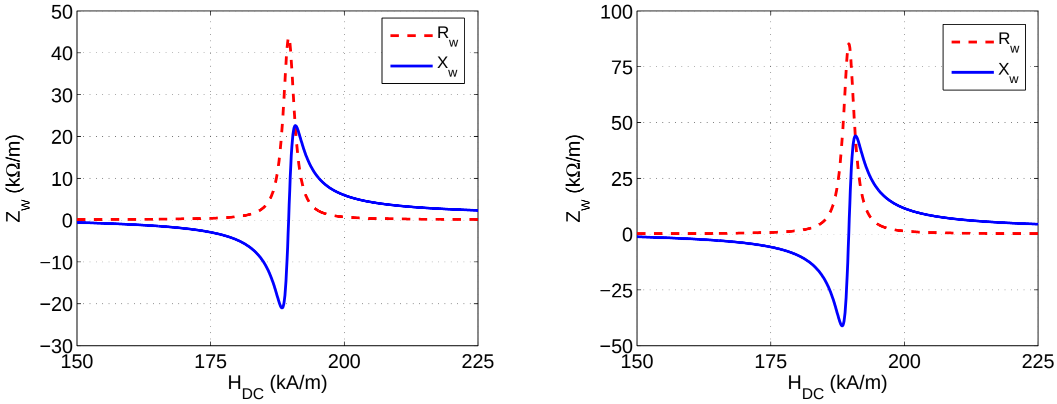

(a) (b)

Figure 6.6 – Real and imaginary parts of the distributed wire impedance as a function of the normalized DC magnetic field for a copper wire of radius $a_1 = 0.001\lambda$, covered by a YIG layer of thickness (a) $t = 0.05a_1$ and (b) $t = 0.1a_1$.

6.4 Reconfigurable Absorbers based on Resistive Sheets

Bearing in mind the dominant role of the wire resistance, the logical alternative is to investigate the use of grid of wires as resistive sheets incorporated in multi-layered electromagnetic absorbers. Moreover, since the resistance of the wires is a function of their magnetic properties, such resistive sheets can be reconfigured through DC magnetic fields, mechanical stresses, or, more interestingly, DC currents flowing along the wires [36, 37].

Such property can be exploited at least in the design of two different reconfigurable absorbers: wideband absorbers with reconfigurable notches, and narrowband absorbers with a reconfigurable absorbing band. The former are useful to track objects that are hidden to external observers. For example, consider an object covered by a wideband absorber with a narrow non-absorbing notch, whose frequency position dynamically changes with time. In such a case, only those radar stations aware of the time-frequency position sequence of the notch would have a reasonable probability to track the object. Contrarily, narrowband absorbers with a reconfigurable absorbing band could be useful to mitigate the effect of interferences in wireless communication systems, suppressing a given frequency channel without affecting the other ones.

Let us implement a classic absorber, the Salisbury screen [48, 120], as a proof-of-concept example of absorbers incorporating resistive sheets. This absorber consists of a resistive layer placed at a $\lambda/4$ distance of a ground plane, i.e., at the distance where the local electric field acting on the resistive layer is maximized. From a transmission line standpoint, the short-circuit produced at the ground plane is transformed into an open-circuit at the specific distance of $\lambda/4$ [22]. Therefore, the input impedance seen by an incident plane wave propagating in free space is given by the grid impedance connected in parallel with an open-circuit, trivially reducing to the grid impedance. In this manner, if the grid impedance equals to that of free-space, the propagation in free-space is matched to the Salisbury screen, there is no reflection, and all of the incident power is dissipated within the absorber.

Consider first the design of a Salisbury screen with a reconfigurable notch, i.e., a reconfigurable narrow non-absorbing band within a wider absorbing band. The design of the absorber is simple if the resistive sheet is composed of wires whose resistance is dominant over the other impedance terms. In such a case, the grid impedance is given by the product of the wire resistance by the separation between wires, $Z_{\mathrm{grid}} \simeq d \cdot R_{\mathrm{w}}$ (i.e., the current flowing in the wire is averaged over the grid period, and therefore the impedance must be multiplied by the same factor). Moreover, if the wire resistance can be approximated by its QS value, $R_{\mathrm{w}} \simeq 1/\left(\pi a^2 \sigma\right)$, a simple design rule to select the radius, conductivity, and separation between the wires can be written as

$$\frac{d}{\pi a^2 \sigma} = \eta_0 \tag{6.23}$$

Following the analysis carried out in Chapter 3 and, in particular, Fig. 3.2, it can be concluded that wire radii on the order of one micron are optimal for such purpose in the GHz frequency range. For such wires, the wire distributed resistance is dominant over the other impedance terms (see Fig. 3.2(c)), and it has in general converged to its QS value $R_{\mathrm{w}} \simeq 1/\left(\pi a^2 \sigma\right)$. However, the latter does not hold at the specific FMR frequency, at which the magnetic losses result in a minimum of the penetration depth. Thus, the QS limit has not been reached, and the wire resistance is significantly larger. Therefore, a notch in the absorbing band is bound to appear at the FMR frequency.

Among the wires reported in the literature, the Fe-rich wire experimentally characterized in [25] has been identified as the most suitable candidate. Such wire has a nominal composition $Fe_{76}Si_9B_{10}P_5$, a metallic core of $a = 0.75\,\mu$m radius, and total diameter (including the Pyrex coating) of $28\,\mu$m. The magnetic properties of the wire have been retrieved by the authors of [25] by fitting theoretical models to the measured absorption spectra, and are given by: $\mu_0 M_s = 1.422\,\mathrm{T}$, $\alpha = 0.00135$, $H_k = 47.75\,\mathrm{kA/m}$, $\gamma = 2.088 \times 10^{11}\,\mathrm{T^{-1}s^{-1}}$, and $\sigma = 1.31 \times 10^5\,\mathrm{S/m}$.

Assuming such material parameters, the wire features the NFMR (FMR in the absence of DC biasing) at a frequency

$$f_{\mathrm{NFMR}} = \frac{\mu_0\gamma}{2\pi}\sqrt{H_k\left(H_k + M_s\right)} \simeq 9.91\,\mathrm{GHz} \tag{6.24}$$

which is the frequency at which the notch in the absorbing band is centered in the absence of any external DC biasing. Furthermore, the frequency position of the notch can be tuned by an electric DC current circulating along the wires. In essence, the field induced by the DC current produces a torque on the axial magnetization that shifts the FMR resonance frequency towards lower frequencies. This effect can be macroscopically modeled by associating an effective DC magnetic field, $H_{\mathrm{I_{DC}}}$, to the applied DC electric current I_{DC}. The effective field can be retrieved experimentally by examining the position of the FMR frequency as a function of I_{DC} and, following the experimental data presented in [36], it has been assumed as follows

I_{DC} (mA)	$H_{\mathrm{I_{DC}}}$ (kA/m)
0	0
5.75	-10
8	-17
10	-29

Note that the wires studied in [36] have a different composition than the selected Fe-rich wire. Therefore, the effective fields acting on the wire might differ from the ones assumed in our analysis. However, since wires with larger content in iron are affected by larger effective fields per current unit [36], the values assumed in our analysis can be considered a pessimistic estimation of the reconfigurable capabilities.

Finally, the absorber design is completed by setting the separation between the resistive sheet and ground plane as $h = 7.5\,\mathrm{mm}$ ($\lambda/4$ at $10\,\mathrm{GHz}$), and selecting the separation between the wires according to the design rule (6.23), i.e., $d = \eta_0 \pi a^2 \sigma = 67\,\mu$m. The performance of the resultant absorber has been analytically and numerically assessed: the

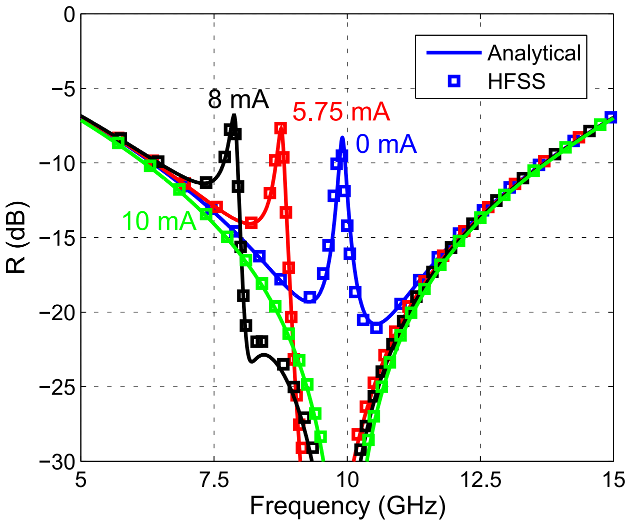

Figure 6.7 – Comparison of numerical and analytical reflection power coefficients for a Salisbury screen composed of a grid of Fe-rich wires of $a = 0.75\,\mu$m radius, separation between the wires of $d = 67\,\mu$m, and distance to the ground plane of $h = 7.5$ mm ($\lambda/4$ at 10 GHz). Each line corresponds to a different DC current circulating along the wires.

analytical solution corresponds to the evaluation of (6.11), and the numerical solution has been computed with the commercial full-wave simulator HFSS. In order to obtain an accurate response from the numerical solver, the maximum mesh step within the ferromagnetic wire has been set to 25 nm.

Fig. 6.7 depicts the comparison of the numerical and analytical reflection power coefficients. There is an excellent agreement between analytical and numerical predictions. Moreover, it is apparent that simple design rule (6.23) leads to a good absorbing performance, i.e., the reflection power coefficient is minimized at 10 GHz, with a value below -30 dB, and its value is below -10 dB for frequencies ranging from 6.25 GHz to 17.75 GHz (i.e., a 115% fractional bandwidth). In addition, the reflection power coefficient is characterized by the presence of a narrow non-absorbing band, whose width and maximum peak is determined by the strength of the FMR. As predicted by the theory, the frequency position of the notch is centered at 9.9 GHz when there is no DC current circulating along the wire, $I_{DC} = 0$. Moreover, the frequency position of the notch decreases as I_{DC} increases, and a current of I_{DC}=10 mA is sufficient to move the notch from the center of to completely outside the absorbing band.

Secondly, consider the design of an electromagnetic absorber with a narrow reconfigurable absorbing band. To this end, the separation between wires must be selected significantly sparser, so that the condition $d \cdot R_{\mathrm{w}} = \eta_0$ is only satisfied at the FMR resonance frequency. By doing so, the absorption is maximized at the FMR frequency, while it should be negligible at other frequencies. Since the SE limit holds at the specific FMR frequency, the wire resistance can be written as $Z_{\mathrm{w}} \simeq \eta_{\mathrm{w}}/\,(2\pi a)$ (see equation (3.4)), and a simple design rule to select the radius, conductivity, and separation between the wires can be written as

$$\frac{d}{2\pi a}\sqrt{\frac{\omega \mu_{\mathrm{w}}''}{\sigma}} = \eta_0 \tag{6.25}$$

where μ_{w}'' is the negative of the imaginary part of the wire permeability (2.21), evaluated at the resonant frequency, (2.22). To finalize the design, the wire radius has been increased up to $a = 5\,\mu\mathrm{m}$ to reduce losses outside the absorbing band, assuming the same electromagnetic properties for the wires. Thus, according to the design rule (6.25), the interwire spacing must be set to $d = 230\,\mu\mathrm{m}$, while the distance to the ground plane has been fixed to $h = 7.5\,\mathrm{mm}$ ($\lambda/4$ at 10 GHz). Fig. 6.8 depicts the comparison of the numerical and analytical reflection power coefficients. Again, a good agreement is found between numerical and analytical data. Moreover, the reflection power coefficient is characterized by a narrow absorbing band, whose frequency position decreases as the DC current is increased. Outside the absorbing band, the reflection power coefficient is above -1.5 dB. Note that the bandwidth of this absorbing band is mostly determined by the resonant linewidth, and therefore it is significantly narrower than other absorber designs with the same height, for example, the previous example. Far from being a disadvantage, this behavior can be exploited to avoid interferences in wireless communications, where only one interfering channel, and not the whole transmission, must be suppressed.

Therefore, it can be concluded that this class of ferromagnetic wires can be adopted in the design of reconfigurable absorbers, e.g., wideband absorbers with a reconfigurable non-absorbing notch, and narrowband absorbers with a reconfigurable absorbing band. It is worth remarking again that the Salisbury screen must be considered as a proof-of-concept example, and that resistive sheets based on ferromagnetic wires could be included in state-of-the-art multi-layered ultra-wideband absorbers. [121].

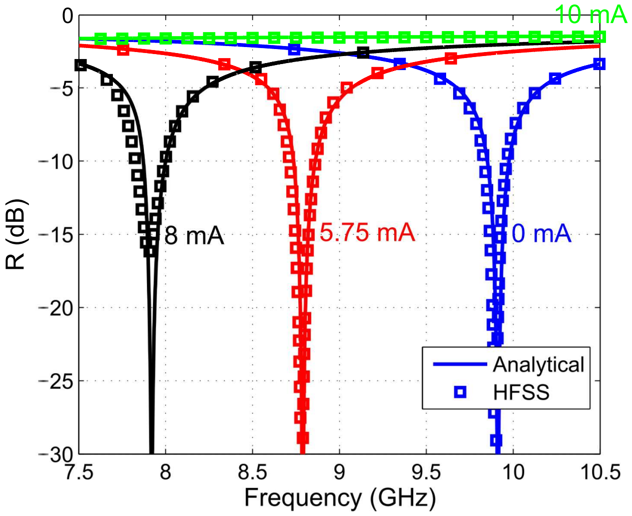

Figure 6.8 – Comparison of numerical and analytical reflection power coefficients for a Salisbury screen composed of a grid of Fe-rich wires of $a = 5\,\mu$m radius, separation between the wires of $d = 230\,\mu$m, and distance to the ground plane of $h = 7.5$ mm ($\lambda/4$ at 10 GHz). Each line corresponds to a different DC current circulating along the wires.

6.5 Conclusions

The focus of this chapter has been artificial impedance surfaces realized as grids of ferromagnetic wires close to a ground plane. To this end, the analytical solution to the problem has been formulated, resulting in a general expression for the reflection coefficient as a function of frequency and angle of arrival.

This model has been employed to derive the resonant condition under which strong currents are excited along the wires, even when the grid is located in the proximity of the ground plane. Moreover, an explicit expression for the reactive load required to satisfy this resonant condition has been introduced. In particular, the required reactive load is capacitive and follows a soft and linear frequency dependence. This non-resonant behavior is an advantage for the design of reconfigurable systems. It has also been demonstrated that the values for the required load are realistic, and that it can be implemented with ferromagnetic wires. Unfortunately, although ferromagnetic wires can provide the necessary reactive loads, the resistance associated to such reactive loads is to high to sustain the resonance, even for their operation as electromagnetic absorbers. However, alternative implementations, such as conductive wires loaded with lumped elements and/or non-conductive magnetic coatings, could be more successful, and are analyzed in Appendix C.

The dominant role of the losses has motivated the study of electromagnetic absorbers based on resistive sheets composed of ferromagnetic wires. In this regard, it is demonstrated that ferromagnetic wires can be adopted in the design of wideband absorbers with a reconfigurable non-absorbing notch, of interest, for example, in the tracking of objects hidden to other observers. This concept has been pushed forward with a proof-of-concept design consisting of a notched Salisbury screen. The design has been constructed by using wires available in the literature, and reconfigurable capabilities based on DC electric currents flowing along the wire are analyzed.

Chapter 7

Ferromagnetic Wires for Contact-Less Sensing

7.1 Introduction

Technological applications of ferromagnetic wires have been traditionally related to the field of sensing devices in the low-frequency range (up to MHz) [6]. As a matter of fact, MI based sensors in which the ferromagnetic wire is integrated in an electronic circuit have been popular for applications not only including very sensitive magnetic field sensors, but also mechanical stress, temperature, position, chemical and multi-functional sensors [32].

More recently, sensing applications of ferromagnetic wires in the GHz frequency range have been proposed under the paradigm of self-sensing materials [122]. Instead of integrating the wires within an electronic circuit, an ensemble of wires is distributed within the sample under study, and the variations in the magnitude of interest are recorded as alterations in the reflected/transmitted fields when the sample is illuminated by an antenna.

A sketch of this paradigm is depicted on Fig. 7.1. Consider an imaging system in which an antenna illuminates an object and records the scattered/reflected field, which is a function of its electromagnetic properties. Processing the recorded field by means of inverse scattering techniques makes it possible to estimate the electromagnetic properties of the object, or even to create a 3D map of its electromagnetically heterogeneous structure. Unfortunately, this process is intrinsically restricted to magnitudes that affect the electromagnetic properties of the solid at the frequency band of operation. Thus, many useful magnitudes (mechanical stress,

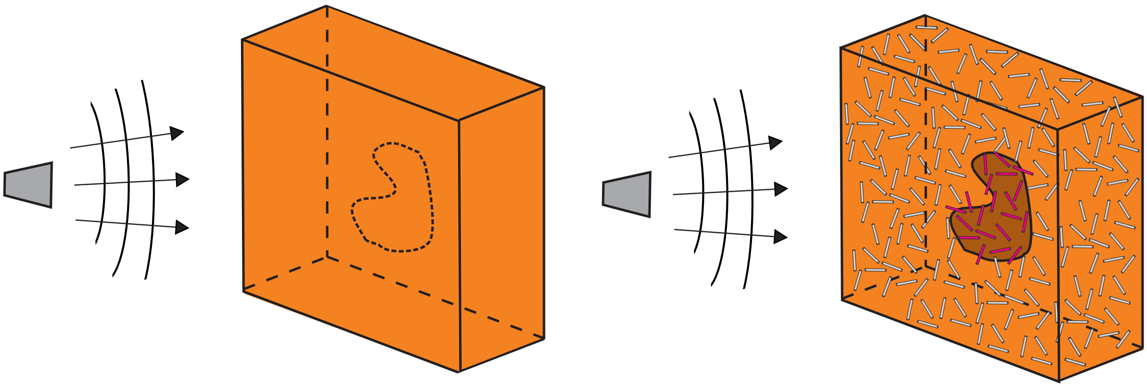

Figure 7.1 – Sketch of ferromagnetic materials as self-sensing materials.

temperature, chemical activity...) might be lost to such sensing mechanism. One way to overcome this restriction is to introduce contrast particles whose electromagnetic properties are a function of the magnitudes of interest. Specifically, ferromagnetic wires featuring magnetostrictive effect can be adopted as contrast particles for mechanical-stress sensing, of great interest for architectural and health monitoring. An additional advantage of ferromagnetic wires is that, being conductive particles, they scatter a significant amount of power.

State-of-the-art experiments treat ensembles of ferromagnetic wires as artificial electromagnetic materials [45–47], and the sensing process consist of estimating the effective constitutive parameters of the material as a function of the applied mechanical stresses, giving rise to the concept of self-sensing materials. Notwithstanding the success of such material-oriented systems, this dissertation would also like to emphasize the use of a single wire for contact-less sensing. In fact, a single wire can be placed where the mechanical action is bound to happen, enabling the sensing at such specific location. This technique can be of great interest for circuit-less battery-less monitoring of implants.

Previous experiments on ferromagnetic wires for self-sensing materials have been focused on Co-rich wires [38, 39, 42, 45–47]. Most probably, this is due to the heritage of low-frequency MI sensors, in which the largest impedance variations are achieved with negative but near-zero magnetostriction constants. However, Fe-rich wires, which have not been investigated yet in this context, could be advantageous in the design of radar-based contact-less sensors. Note that Fe-rich wires feature positive and large magnetostriction constants, which results in a dominant axial magnetization and in the presence of the natural ferromagnetic resonance

(NFMR) at GHz frequencies [3, 5]. Therefore, Fe-rich wires are advantageous for high-frequency sensors, since no biasing field is required to produce the ferromagnetic resonance (FMR). Even in the presence of a biasing field, Fe-rich wires provide a stronger and higher-frequency FMR due to their higher magnetization at saturation, thus leading to higher spatial resolutions and smaller antennas. Moreover, a high magnetostriction constant ensures a strong response to external mechanical stresses.

This chapter investigates the possibility of using Fe-rich wires for mechanical stress self-sensing materials, including the characterization of magnetostrictive effect at GHz frequencies, as well as the estimation of their performance as self-sensing materials and single-wire contact-less sensors.

7.2 Characterization of the Magnetostrictive Effect at GHz Frequencies

The magnetostrive effect can be understood as the variation of the wire impedance as a function of applied mechanical stresses. Unfortunately, the characterization of the wire impedance under mechanical stresses at high-frequencies can be a cumbersome task. As a matter of fact, while the wire impedance can be easily measured at the low-frequency limit with an oscilloscope by means of the two/four probe method [123], as frequency increases the probe effect becomes dramatic and the wires tend to radiate. Therefore, high-frequency MI measurements are based on the integration of ferromagnetic wires in transmission lines, such as microstrip lines [38, 39, 42], coaxial cables [43, 44] and waveguides [45].

It is worth remarking that these experiments measure *the impedance of the transmission line formed by the wire*, and an additional retrieval technique is required to recover the actual *wire impedance.* Although this might seem a subtle difference, it must be considered for contact-less sensing, since the wires are not integrated in any circuit/tranmission line, and thus the actual wire impedance is required to estimate the magnitudes of interest. A retrieval procedure for coaxial lines was presented in [43]. However, both ends of the ferromagnetic wire must be connected to the coaxial line, which hinders the application of mechanical stresses within such experimental setup. To go further in the state of the art and overcome this problem, a retrieval procedure using metallic rectangular waveguides is presented here.

7.2.1 Retrieval Procedure

Fig. 7.2 represents the setup for the characterization of ferromagnetic wires in a metallic rectangular waveguide: a wire of radius a is positioned in the middle of a waveguide of width d, height h and length $2l$. The wire ends are short-circuited to the waveguide walls to emulate an analytically tractable infinitely-long wire, and the incident electric field is parallel to the wire so that its magnetic response is excited. The goal of the retrieval procedure is to recover the wire impedance, Z_w, from the S_{11} and S_{21} scattering parameters measured at the input and output of the waveguide.

This experimental setup has been analytically solved in Chapter 2, and closed form expressions for the S_{11} and S_{21} scattering parameters have been introduced in (2.49) and (2.50), respectively. Those equations must be rewritten in terms of Z_w to serve our experimental purposes. To this end, note that the scattered field coefficient, b_0^{TM}, is given by $\left(b_0^{TM}\right)^{-1} = -\frac{4}{k_0 d}\left(Z_\mathrm{w} + \alpha_0^{-1}\right)$. By doing so, the S_{11} and S_{21} scattering parameters can be written as

$$S_{11} = -\frac{\eta_0 k_0}{k_g d}\frac{1}{Z_\mathrm{w} + \alpha_0^{-1} + \frac{\eta_0 k_0}{4}G_\mathrm{int}^\mathrm{wg}}e^{-j2k_g l} \tag{7.1}$$

$$S_{21} = \left[1 - \frac{\eta_0 k_0}{k_g d}\frac{1}{Z_\mathrm{w} + \alpha_0^{-1} + \frac{\eta_0 k_0}{4}G_\mathrm{int}^\mathrm{wg}}\right]e^{-j2k_g l} \tag{7.2}$$

In view of (7.1) and (7.2), it is straightforward to compute Z_w from either S_{11} or S_{21} as follows

$$Z_\mathrm{w}^R = -\frac{\eta_0 k_0}{k_g d}\frac{1}{S_{11}e^{j2k_g l}} - \alpha_0^{-1} - \frac{\eta_0 k_0}{4}G_\mathrm{int}^\mathrm{wg} \tag{7.3}$$

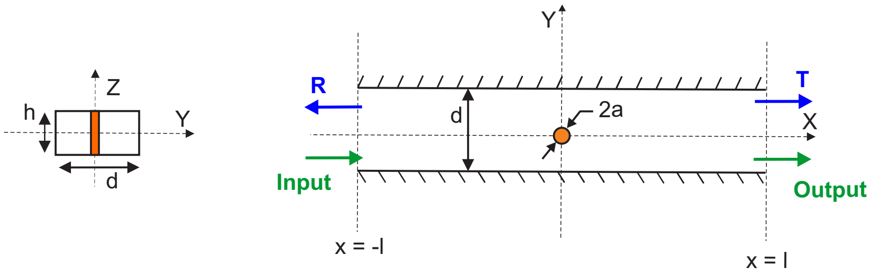

Figure 7.2 – Sketch of a ferromagnetic wire of radius a inside a rectangular waveguide of width d, height h and length $2l$.

$$Z_{\mathrm{w}}^{T} = -\frac{\eta_0 k_0}{k_g d}\frac{1}{S_{21}e^{j2k_g l}-1} - \alpha_0^{-1} - \frac{\eta_0 k_0}{4}G_{\mathrm{int}}^{\mathrm{wg}} \tag{7.4}$$

The first term of (7.3) and (7.4) must be understood as the impedance of a wire inside the waveguide. The second and third terms subtract from this impedance the loading produced by the waveguide walls ($\eta_0 k_0/4\cdot G_{\mathrm{wg}}$) and the impedance of a PEC wire (α_0^{-1}), so that the final result is the actual wire impedance, Z_{w}. In theory, $Z_{\mathrm{w}}^{R} = Z_{\mathrm{w}}^{T} = Z_{\mathrm{w}}$, so that Z_{w} can be indifferently computed from S_{11} or S_{21}. From a practical standpoint, S_{11} is significantly smaller than S_{21} due to the reduced cross-section of the wire as compared to the waveguide width, and therefore Z_{w}^{R} is much more sensitive to noise, reflections produced by mismatched junctions and other experimental artifacts than Z_{w}^{T}.

7.2.2 Numerical Validation

In order to check the accuracy of the analytical model employed for the retrieval technique, the results have been tested with a well-established full-wave electromagnetic solver: CST Microwave Studio [124].

The model of the numerical simulation is depicted in Fig. 7.3(a) and consists of a WR-90 metallic rectangular waveguide ($d = 22.86$ mm, $h = 11$ mm, $2l = 15$ cm) and a wire placed in the middle of the waveguide. The inset in the figure represents the wire geometry. Note that the simulation of a rectangular waveguide (of a few wavelengths size) with a ferromagnetic wire (of $10^{-4} \sim 10^{-5}$ wavelengths size) with finite conductivity and gyrotropic magnetic susceptibility is a cumbersome task for current numerical solvers, and therefore the numerical simulations have been performed with a simpler, two layer wire. Such a wire is composed of an inner PEC wire of radius a_1, covered by a magnetic coating of permeability $\mu = \mu_r\mu_0$, and total radius a_2. The distributed impedance of this type of wires can be written as in (6.22)

$$Z_{\mathrm{w}} = j\frac{\omega\mu}{2\pi}\ln\left(\frac{a_2}{a_1}\right) \tag{7.5}$$

In essence, the magnetic coating loads the PEC wire with a given reactance (for lossless μ), which increases with μ and the ratio between the external and internal radii, a_2/a_1.

For illustrative purposes, three different values of the magnetic coating $\mu_r = 5,\ 10$ and 15, with dimensions $a_2 = 0.1$ mm and $a_1 = 0.05$ mm,

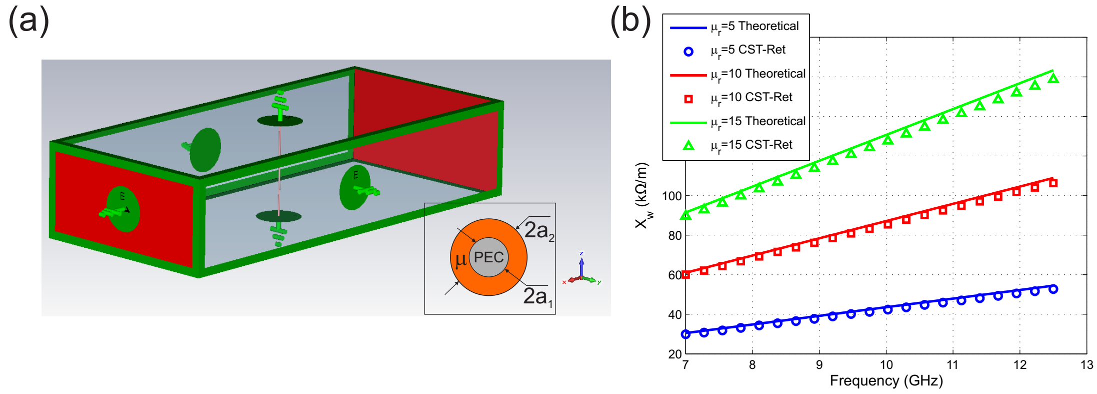

Figure 7.3 – (a) CST Model of the WR-90 waveguide with connected wire. The inset in the figure represents the structure of the simulated wire. (b) Comparison of the theoretical wire reactance and the reactance retrieved from the R, T coefficients simulated with CST.

have been employed in the numerical simulations. Once the S_{11} and S_{21} scattering parameters have been computed with CST, Z_{w} has been determined by means of the proposed retrieval technique and compared to the theoretical solution (i.e., equation (7.5)), as it is shown in Fig. 7.3(b). In this numerical example, Z_{w}^{R} and Z_{w}^{T} converged perfectly, and therefore a single Z_{w} line has been represented. It can be concluded that there is a good agreement between the retrieved and theoretical results. Small differences can be ascribed to numerical errors in the simulator (mesh and truncation), the truncation of the $G_{\mathrm{int}}^{\mathrm{wg}}$ interaction constant (2.47)-(2.48), and the small argument bessel function approximations intrinsically assumed in the theoretical Z_{w}, (7.5).

7.2.3 Experimental Validation

Recall that in Chapter 3, three different $(\mathrm{Co}_{0.94}\mathrm{Fe}_{0.06})_{75}\mathrm{Si}_{12.5}\mathrm{B}_{12.5}$ wires of 22.5 μm, 5 μm and 2 μm metallic radius were measured in a metallic rectangular waveguide in order to investigate the correlation between the wire geometry and absorption spectrum. Such wires were trapped between two WR-90 waveguides so that the experimental setup adjusts to that of the retrieval technique (see Fig. 7.2). Therefore, those experimental data can be used to test the consistency of the retrieval technique.

The Z_{w} values retrieved from the S_{21} scattering parameter are depicted in Fig. 7.4, where each color line corresponds to a different biasing magnetic field as specified in the caption. The retrieved impedances are consistent with the study of Z_{w} with FMR effect in saturated wires (see Fig. 3.2): On the one hand, a peak of resistance appears at the FMR, whose frequency position increases along with the biasing field. In addition, the resistance increases as the wire radius decreases, due to the higher penetration of the electromagnetic field in the wires. On the other hand, the retrieved reactance presents the expected maximum-minimum sequence. However, the reactance is asymmetric with respect to the resonant point due to parasitic reactive loading. This effect is an artifact of the experimental setup, produced by the small separation between the waveguides where wires are positioned. Note that the measurements were originally carried out to evaluate the absorption spectrum, in which this effect has a minor impact, and that it can be mitigated with the correct setup/calibration procedure.

7.3 Fe-rich Wires for Contact-Less Sensing

7.3.1 Characterization of the Wires

In order to assess the performance of Fe-rich wires as mechanical stress self-sensing materials, a $Fe_{77.5}Si_{12.5}B_{10}$ wire was fabricated by means of the Taylor-Ulitovsky technique [7, 8] in collaboration with Prof. M. Vázquez at the Material Science Institute of Madrid (ICMM). A SEM image of the wire was taken at the Foundation for the Research and Development of Nanotechnology in Navarra (Fidena) with the assistance of J. Bravo, and it is represented in Fig. 7.5. As it is shown, the wire consists of a metallic core of 5.25 μm radius and total radius (metallic core and pyrex coating) of 12.5 μm.

A photograph of the experimental setup employed to characterize the wires is depicted in Fig. 7.6. To further clarify the setup, the figure includes schematic views of the setup in the XY-, XZ-, and YZ-planes. The experimental setup consists of a WR-112 rectangular waveguide ($d = 28.6$ mm, $h = 12.8$ mm, $2l = 10$ cm), where both waveguide ends are connected to SMA adaptors and the scattering parameters are recorded with an Agilent PNA-X N5242A network analyzer. The WR-112 rectangular waveguide was selected so that the NFMR of the wires lies within the frequency range of the experiment. Note how a small hole has been drilled in the center of the broad wall of the waveguide. By doing so, the wires can entirely cross the waveguide while being parallel

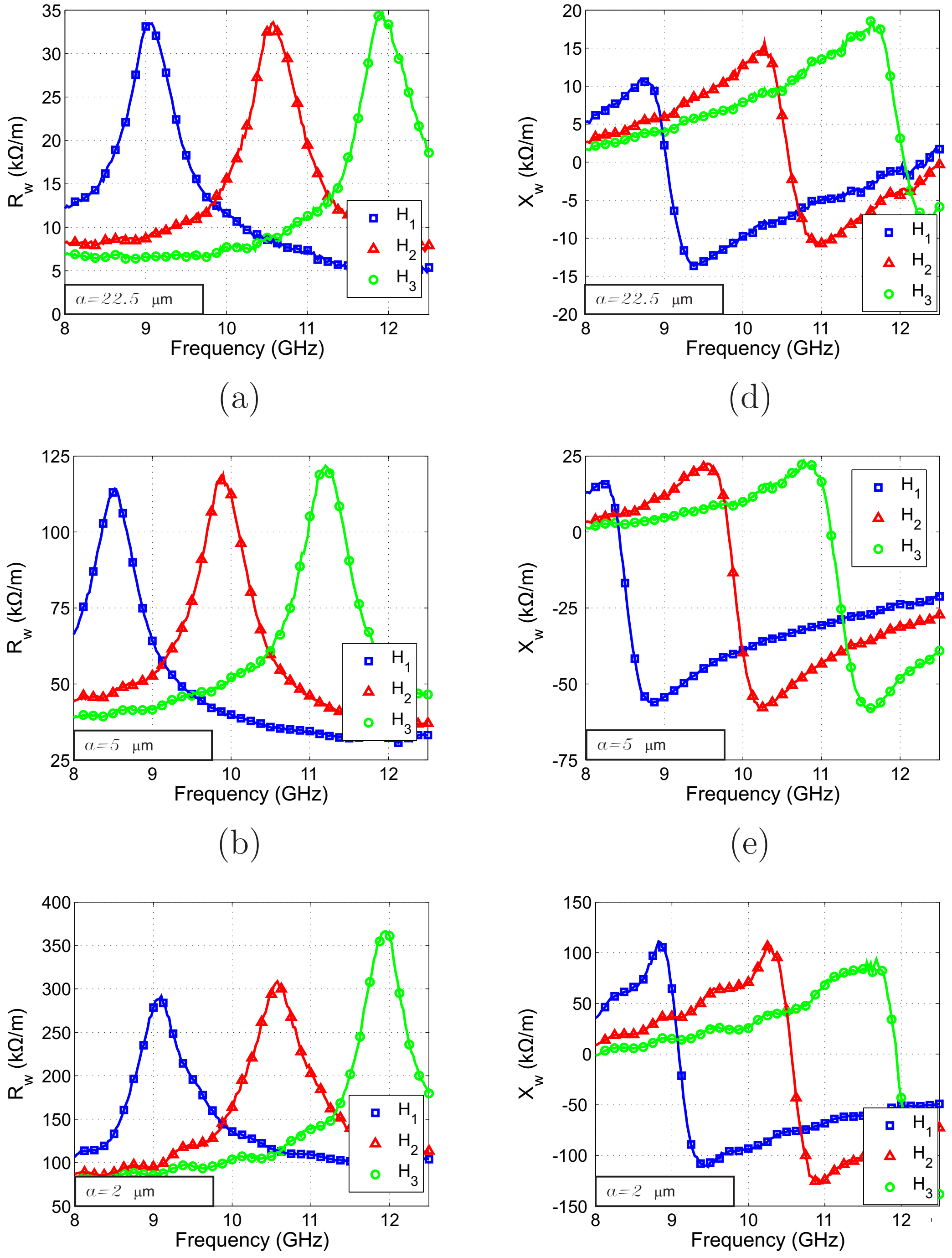

(a) (d)

(b) (e)

(c) (d)

Figure 7.4 – Retrieved resistance (a)-(c) and reactance (d)-(f) for Co-rich wires of 22.5 μm, 5 μm and 2 μm metallic radius, respectively. Each line corresponds with a different biasing field $H_1 = 89.4\,\text{kA/m}$, $H_2 = 117.7\,\text{kA/m}$ and $H_3 = 146.0\,\text{kA/m}$, directed along the wire axis.

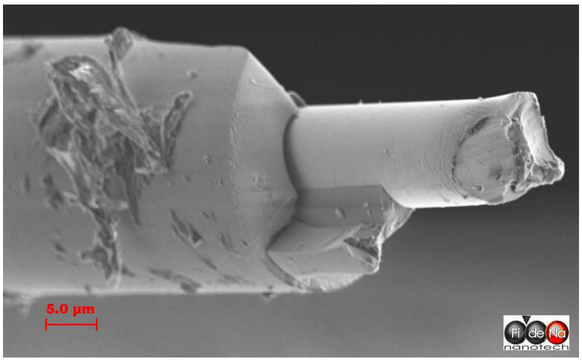

Figure 7.5 – SEM image of the Fe-rich wire under test.

to the incident electric field, i.e., the wires are positioned along the Y-axis according to Fig. 7.6. Due to the orientation of the waveguide, no holder or insulating platform is required. Outside the waveguide, both wire ends have been fixed to micropositioners. In this way, when one of the micropositioners is shifted mechanical stresses are produced along the wires axis, resulting in an elongation dL. Due to the magnetostrictive behavior of the wires, such mechanical stresses produce variations of measured scattering parameters and, as a consequence of it, of the retrieved distributed impedance. It is worth remarking that no external DC magnetic field has been employed to polarize the ferromagnetic wires. The parasitic loading produced by the waveguide holes was estimated and calibrated by measuring copper wires of different sections. Furthermore, it was checked that no variation in the reflection and transmission coefficients was observed when the copper wires were subjected to mechanical stresses.

The retrieved distributed impedance Z_w as a function of the wire elongation for the Fe-rich wire is represented in Fig. 7.7. It can be concluded that the wires feature the typical resonant behavior produced by the NFMR within a homogeneous core, consistent with the theoretical analysis of Chapter 3. Namely, a maximum of resistance and an inductive-to-capacitive transition of the reactance around the resonance. In addition, the elongation of the wires from 0 to 60 μm produces a shift of the NFMR frequency, f_NFMR, from 7 GHz to 8.25 GHz.

This behavior is ascribed to an increase in the anisotropy field, H_k. When no mechanical forces are applied to the wire, H_k is defined by the mechanical stresses produced during the fabrication process. Due to the positive magnetostriction constant of the wires, these stresses result in a positive H_k and the occurrence of the NFMR. Therefore, additional mechanical stresses increase H_k, with the consequent increase in f_NFMR.

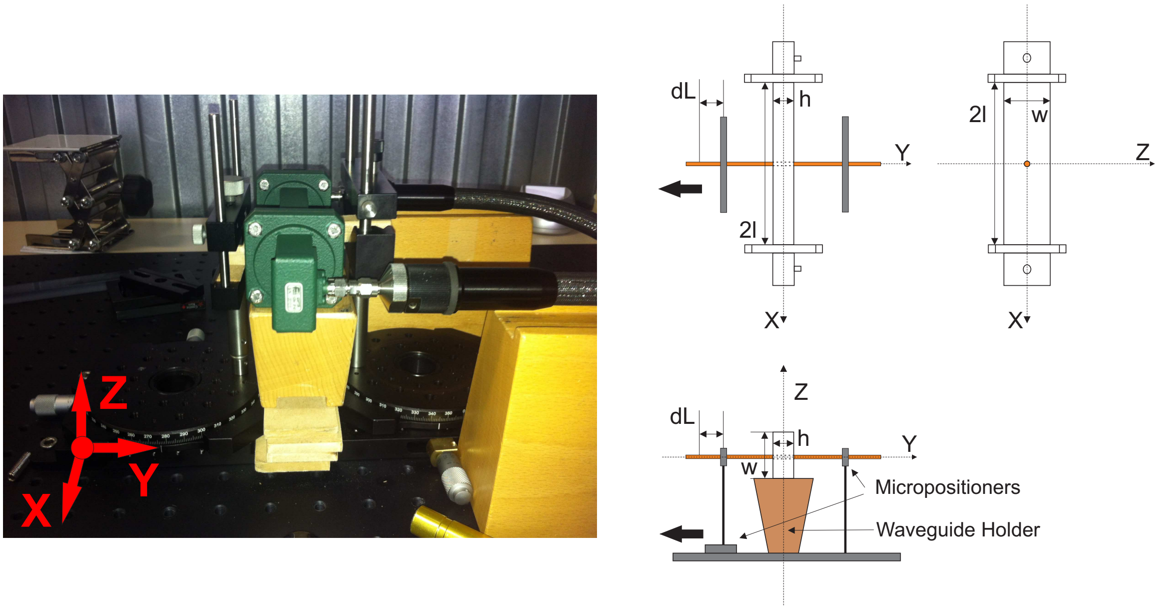

Figure 7.6 – Photograph of the experimental setup and schematic views in the XY-, XZ-, and YZ-planes. The black arrows indicate the direction of the shift.

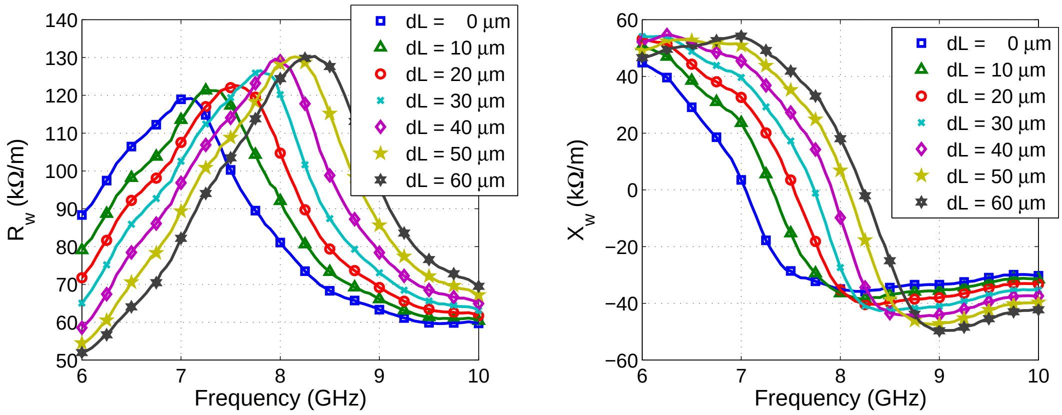

(a) (b)

Figure 7.7 – Experimentally retrieved (a) resistance and (b) reactance of a $Fe_{77.5}Si_{12.5}B_{10}$ wire of metallic radius $a = 5.25$ μm as a function of the wire elongation dL.

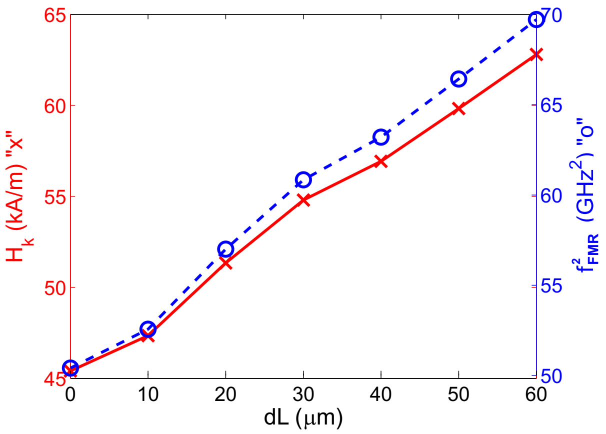

Figure 7.8 – Anisotropy field H_k and square of the FMR frequency f^2_{FMR} as a function of the wire elongation, dL.

To further clarify this fact, note that f_{NFMR} is given by the well-known Kittel relationship [23]

$$f_{\mathrm{NFMR}} = \frac{\mu_0\gamma}{2\pi}\sqrt{H_k\left(H_k + M_s\right)} \tag{7.6}$$

Inversely, for $M_s \gg H_k$ the anisotropy field can be determined as follows

$$H_k = \left(\frac{2\pi}{\mu_0\gamma}\right)^2 \frac{f^2_{\mathrm{NFMR}}}{M_s} \tag{7.7}$$

Fig. 7.8 depicts H_k and f^2_{NFMR} as a function of the elongation in the wires. To this end, f_{FMR} has been fixed to the frequency of maximal resistance, and typical parameters of Fe-rich wires [3] $\mu_0 M_s = 1.60\ T$ and $\gamma = 2.088 \cdot 10^{11} T^{-1} s^{-1}$ have been assumed. The retrieved values of H_k, approximately ranging from 20 kA/m to 30 kA/m, are in accordance to those of wires with high magnetostriction constant [24]. Furthermore, both H_k and f^2_{FMR} increase linearly along with the elongation.

7.3.2 Estimation of the Sensing Performance

Once the wire impedance Z_{w} has been experimentally characterized, it is possible to estimate the sensing performance of both, a single wire system and an artificial electromagnetic material composed of a random ensemble of wires.

7.3.2.1 Single Wire Contact-Less Sensing

Consider first a single ferromagnetic wire sensing system. The goal is to retrieve the mechanical stresses at which the wire is subjected from variations of the scattering from the wire. In general, the environment of the wire also scatters the incident field, which must be included in the analysis. However, the environment is bound to vary as a function of the specific application, and free-space scattering will be considered here for the sake of simplicity.

Typical radar techniques figures of how much the incident field is disturbed by the presence of the wire are the backscattering, scattering, absorption and extinction cross-sections. The former is also called monostatic cross-section or simply radar cross section, and it is given by [77]

$$\sigma_{\text{back}} = 4\pi r^2 \frac{\widehat{\mathbf{r}} \cdot \mathbf{S}_{\text{scat}} \left(\phi = 0, \theta = \frac{\pi}{2}\right)}{\widehat{\mathbf{n}}_{\text{inc}} \cdot \mathbf{S}_{\text{inc}}} \tag{7.8}$$

σ_{back} has area units and represents the effective area of an ideally isotropic scatterer that provides the same power density in the back direction than the scatterer under consideration. Thus, this figure is a measure of the power scattered at an specific direction. Additional figures corresponding to the overall scattered and absorbed powers are the scattering and absorption cross-sections, given by [77]

$$\sigma_{\text{scat}} = \frac{P_{\text{scat}}}{\widehat{\mathbf{n}}_{\text{inc}} \cdot \mathbf{S}_{\text{inc}}} \tag{7.9}$$

$$\sigma_{\text{abs}} = \frac{P_{\text{abs}}}{\widehat{\mathbf{n}}_{\text{inc}} \cdot \mathbf{S}_{\text{inc}}} \tag{7.10}$$

which also have area units, and represent the areas that, projected on to the incident power density, contain the scattered and absorbed powers, respectively. The addition of the total scattering and absorption cross-sections is defined as the extinction cross-section, $\sigma_{\text{ext}} = \sigma_{\text{scat}} + \sigma_{\text{abs}}$. According to the optical theorem [81], σ_{ext} is related to the imaginary part of the forward scattering amplitude, and represents the reduction in the power carried by the incident field produced by the presence of the scatterer.

Fig. 7.9 represents the backscattering, scattering, absorption and extinction cross-sections as a function of the wire elongation for the studied Fe-rich ferromagnetic wire of $a = 5.25\ \mu$m radius and length $L = 7.5$ mm.

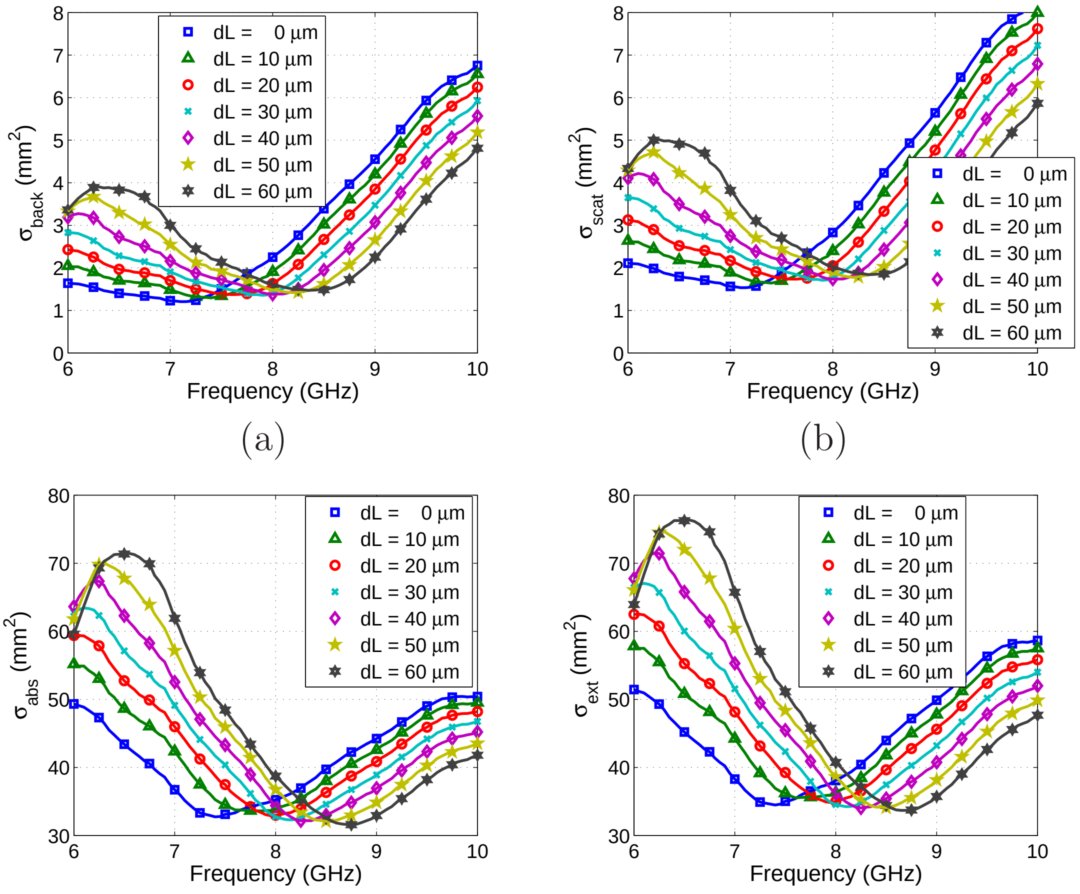

(a) (b) (c) (d)

Figure 7.9 – (a) Backscattering, (b) scattering, (c) absorption and (d) extinction cross-sections as a function of the wire elongation for a Fe-rich ferromagnetic wire of $a = 5.25\ \mu$m radius and 7.5 mm length

Such length has been selected so that $2L = \lambda/2$ at 10 GHz, and therefore enabling large scattered powers at the frequency band of interest. Based on the experimental values of Z_{w} reported in the previous section, the scattering cross-sections have been computed modeling the wire as introduced in Chapter 2, Section 2.4.1.

It is apparent from Fig. 7.9 that all cross-section spectra shift towards higher frequencies along with the elongation. Moreover, the peculiarities of the frequency dispersion behavior of the cros-section spectra can be explained in accordance to Chapter 3 analysis. In particular, both absorption and scattering processes are a function of the current in the wire, which is maximized close to the half-wavelength resonance, thus producing a peak of scattering and absorption close to 10 GHz. In addition, the inductive loading produced by the short-wire below the resonance also increases the current of the wire, producing a second peak of both, absorption and scattering, below the resonance. Finally, the absorption cross-section is much larger than the scattering cross-section for this lossy wire, which is in accordance with Chapter 4 results.

7.3.2.2 Self-Sensing Materials

Consider now a cloud of short ferromagnetic wires that can be modeled as an artificial electromagnetic material. As a first approximation, the constitutive parameters of such artificial material can be estimated via classical electromagnetic mixing formulas such as Clausius-Mossotti/Maxwell-Garnett [126].

Due to practical reasons, these composite materials typically consist of ensembles of short-wires, which result in artificial dielectric materials whose effective permittivity is defined by the electric dipole moments excited in the short-wires. Solving the current excited in the wires as in Chapter 2, the wire electric polarizability α_{ee} can be found as [75]

$$\alpha_{ee} = \frac{1}{j\omega} \int_{-L}^{L} \frac{I\left(z\right)}{E_0} dz \tag{7.11}$$

Knowing the polarizability of a given inclusion, it is straightforward to apply mixing rules to estimate the effective permittivity. For the sake of simplicity, let us start with a mixture of wires aligned along the z axis. Under a Clausius-Mossotti/Maxwell-Garnett formalism, an aligned mixture of ellipsoids is characterized by an effective uniaxial permittivity given by [126]

$$\overline{\overline{\epsilon_{\text{eff}}}} = \epsilon_x \hat{\mathbf{x}}\hat{\mathbf{x}} + \epsilon_y \hat{\mathbf{y}}\hat{\mathbf{y}} + \epsilon_z \hat{\mathbf{z}}\hat{\mathbf{z}} \tag{7.12}$$

where each of its elements is given by

$$\epsilon_i = \epsilon_h + \frac{p\alpha_{ee}^i}{1 - N_i \frac{p\alpha_{ee}^i}{\epsilon_h}} \quad i = x, y, z \tag{7.13}$$

ϵ_h is the polarizability of the host medium, p is the number of wires per unit of volume, and N_i and α_{ee}^i are the depolarization factor and the polarizability of the ellipsoid along the i direction.

Due to the high aspect ratio of the wires the “needle” depolarization factors $N_x = N_y = \frac{1}{2}$, $N_z = 0$ are the natural choice, and it is sufficient to consider the polarizability along the wires (i.e. $\alpha_{ee}^x = \alpha_{ee}^y \simeq 0$, $\alpha_{ee}^z = \alpha_{ee}$). Therefore, the effective permittivity simplifies to

$$\overline{\overline{\epsilon_{\text{eff}}}} = \epsilon_h \left(\hat{\mathbf{x}}\hat{\mathbf{x}} + \hat{\mathbf{y}}\hat{\mathbf{y}} \right) + \epsilon_z \hat{\mathbf{z}}\hat{\mathbf{z}} \tag{7.14}$$

with

$$\epsilon_z = \epsilon_h + p\alpha_{ee} \tag{7.15}$$

Fig. 7.10(a)-(b) represents the computed real and imaginary parts of the z-component of the effective permittivity ϵ_z/ϵ_0 for wires of length $L = 1$ mm and density $p = 5$ wires/cm^3. It can be appreciated that the real part of the effective permittivity is positive as in mixtures of conductive short wires, although its dipersion profile is defined by the occurrence of the NFMR.

As expected, external stresses shift the permittivity dispersion profile towards higher frequencies, which can be measured through variations in the reflection/transmission from the sample, or directly from the retrieval of its constitutive parameters. If only a part of the sample is subjected to mechanical stresses, it must be treated as an heterogeneous solid, where the shape and size of the volume affected by the mechanical stresses can be determined through inverse scattering techniques.

In most practical applications the mixture will be a random ensemble of wires. In such a case, the directionality of the mixtures vanishes, the sample behaves as an isotropic mixture, and the effective permittivity can be written as

$$\overline{\overline{\epsilon_{\text{eff}}}} = \epsilon_m \left(\hat{\mathbf{x}}\hat{\mathbf{x}} + \hat{\mathbf{y}}\hat{\mathbf{y}} + \hat{\mathbf{z}}\hat{\mathbf{z}} \right) \tag{7.16}$$

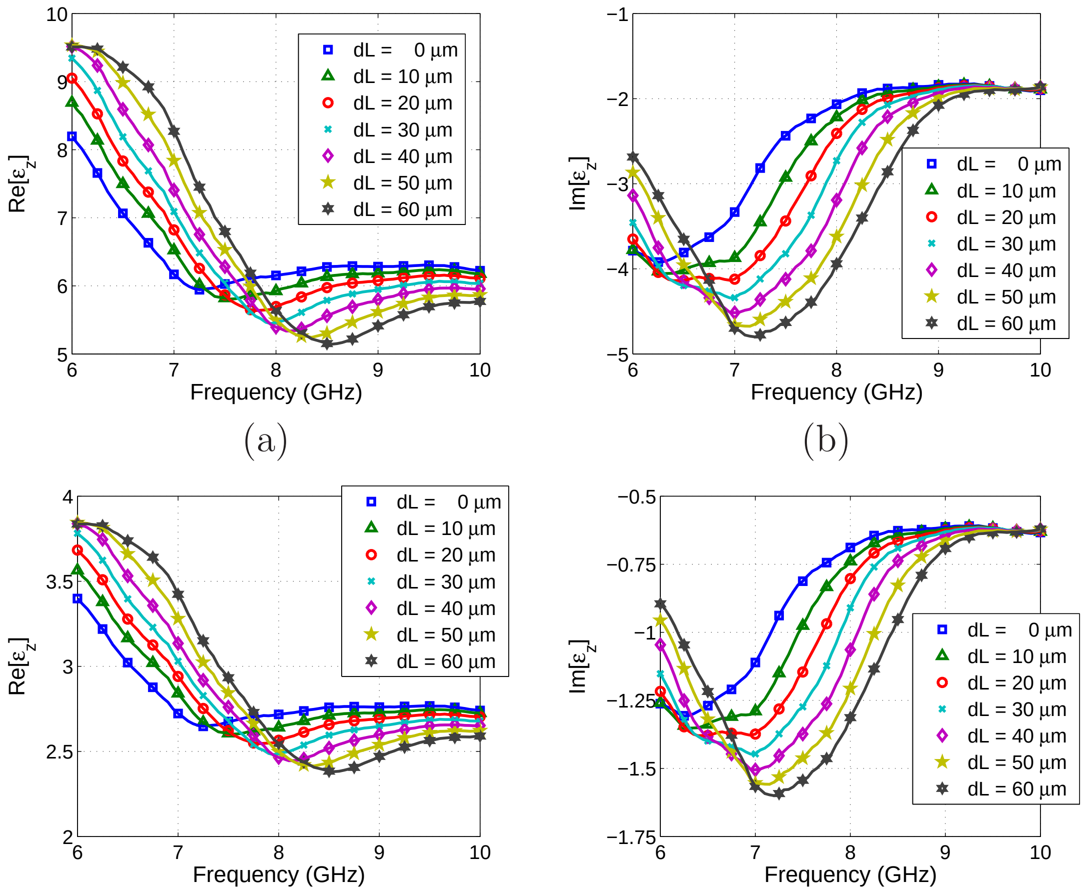

(a) (b)

(c) (d)

Figure 7.10 – Real and imaginary parts of the effective permittivity for aligned (a)-(b) and random (c)-(d) mixtures of short ($L = 1$ mm) Fe-rich wires with density $p = 5$ wires/cm^3 as a function of the wire elongation, dL.

where the electric polarization results from the averaging of each direction susceptibility [126]. For wires with high aspect ratio only one susceptibility component is relevant and therefore

$$\epsilon_m = \epsilon_h + p\alpha_{ee}/3 \tag{7.17}$$

Fig. 7.10(c)-(d) shows the effective permittivity of the same mixture of wires than in Fig. 7.10(a)-(b), but with random orientation of the wires. The results confirm that the response of a random mixture is a diluted version of the aligned one, in the sense that the aligned mixture results in larger permittivity values than the random one, for the same density of wires.

Both random and aligned mixtures are subjected to the limitations of homogenization models. Therefore, their predictions will be accurate as long as the wires and the separation between wires is small enough, and as long as a sufficiently large number of wires is affected by the mechanical stresses. If the former condition is not fulfilled, the structure must be inevitability modeled with complex theory of groups of individual scatterers. If the latter condition is not fulfilled, the structure can still be modeled as an homogeneous mixture, but multiphase mixing rules must be applied. In general, the Pyrex coating of the wires prevents the appearance of percolation processes in the mixtures. However, one must recall this effect when dealing with wires after glass-removal processes. In those cases, more generalized mixing formulas must be adopted [127].

To sum up, multiple models can be adopted to predict the performance of a self-sensing material, where the selection of the model depends on the properties of the mixture. In any case, all applicable models rely on the characterization of the wires through retrieval techniques, as discussed in previous sections.

7.4 Conclusions

This chapter has investigated the possibility of using Fe-rich wires as mechanical stress self-sensing materials. To this end, a retrieval technique aimed to evaluate the wire distributed impedance under mechanical-stresses has been introduced. A Fe-rich $Fe_{77.5}Si_{12.5}B_{10}$ wire of $a = 5.25$ μm metallic radius has been characterized with the proposed retrieval technique. The wire main feature is the presence of the FMR at 7 GHz with no magnetic biasing. Moreover, the magnetostrictive behaviour of the wires leads to shifts in the FMR frequency from 7 GHz to 8.25 GHz for elongations ranging from 0 to 60 μm. This result demonstrates the potential of Fe-rich ferromangetic wires as contact-less mechanical-stress sensors. Furthermore, it proves that no external DC biasing is required for the sensing system. To finalize, it has been pointed out how to estimate the performance of both artificial materials and single-wire sensing systems.

Chapter 8

Conclusions and Guidelines for Future Research

This chapter provides a summary of the main results presented along this dissertation, as well as some guidelines for future research.

8.1 Conclusions

This dissertation has introduced diverse results concerning (amorphous glass-coated) ferromagnetic wires and their use in microwave engineering. While most previous works have been experimentally driven and/or were focused on describing the electromagnetic properties of the wires, this dissertation provides a step forward by introducing modeling tools for the theoretical investigation and design of ferromagnetic wire-based devices. Moreover, these modeling tools have been employed to systematically analyze the main phenomena related to the scattering by ferromagnetic wires, to identify their main potentialities and limitations, and to formulate simple design rules.

First, the analytical modeling of the scattering by ferromagnetic wires has been addressed in Chapter 2. Interestingly, it has been found that, within the thin wire approximation, the scattering by a ferromagnetic wire can be accurately modeled by means of very simple circuit models.

By using those models, a detailed analysis of the transition from surface to bulk phenomena in the scattering by ferromagnetic wires has been presented in Chapter 3. The analysis has revealed that the MI effect tends to disappear in the SE and QS limits. Therefore, wires with radius in the transition from surface to bulk effects lead to the strongest FMR-based MI effect. Such wires are able to provide reconfigurable resistive, inductive and capacitive loading. However, the distributed resistance is always larger than the distributed reactance, which suggests electromagnetic absorbers and contact-less sensors as their most promising applications. Moreover, the complex size-dependent absorption spectrum of the wires has been clarified, and the absorbed to scattered power ratio has been proposed as a size-independent indicator of the FMR resonance frequency.

The limits in the balance of powers involved in the scattering by ferromagnetic wires have been analyzed in Chapter 4. Upper bounds for the maximal absorbed, scattered and extracted powers have been formulated, and the implications of these bounds on ferromagnetic-wire based systems have been discussed. In particular, contact-less sensors based on ferromagnetic wires present a compromise between sensitivity against external agents and the amount of power scattered by the wire. In addition, and counter-intuitively, ferromagnetic wires are found too lossy to reach the upper bound of absorbed power, which limits the scope of very diluted mixtures of wires as electromagnetic absorbers.

Artificial electromagnetic materials based on ferromagnetic wires are addressed in Chapter 5. In contrast with previous experimental studies suggesting that composites of ferromagnetic wires belong to the class of DNG media, the homogenization approach reveals that such composites belong to the class of artificial dielectrics with magnetically controlled permeability. Furthermore, numerical simulations suggest the use of slabs of ferromagnetic wires as narrowband reconfigurable absorbers (exploiting FMR resonance effect) and/or wideband absorbers (exploiting the reduced conductivity of amorphous wires).

Artificial impedance surfaces realized as grids of ferromagnetic wires close to a ground plane have been investigated Chapter 6. Unfortunately, although ferromagnetic wires can provide the necessary reactive loading to create resonant low-profile absorbers, they associated losses are to high to sustain the resonance. However, alternative implementations, such as conductive wires loaded with lumped elements and/or non-conductive magnetic coatings, have been found to be more successful. By contrast, ferromagnetic wires can be adopted in the design of reconfigurable electromagnetic absorbers based on resistive sheets. This paradigm can be applied to at least two different reconfigurable absorbers: wideband absorbers with a reconfigurable non-absorbing notch, and narrowband absorbers with a reconfigurable absorbing band. The former are of interest to track of objects hidden to external observers, and the latter are of interest to mitigate interferences in wireless communications. This concept has been further explored with proof-of-concept designs based on a Salisbury screen tuned through DC electric currents flowing along the wires.

Finally, the use of Fe-rich wires in contact-less sensing has been studied in Chapter 7. To this end, a retrieval technique aimed to evaluate the wire distributed impedance under mechanical-stresses has been introduced. The wire main feature is the presence of the FMR at 7 GHz with no magnetic biasing, whose frequency position shifts from 7 GHz to 8.25 GHz for elongations ranging from 0 to 60 μm. This result demonstrates the potential of Fe-rich ferromagnetic wires as contact-less mechanical-stress sensors. To finalize, several methods to estimate the performance of both artificial materials and single-wire sensing systems have been given.

8.2 Guidelines for Future Research

The focus of this dissertation has been the use of ferromagnetic wires in microwave engineering, where reconfigurable electromagnetic absorbers and contact-less sensors have been identified as some of the most promising applications. The development of reconfigurable electromagnetic absorbers might continue with the integration of ferromagnetic wires in state-of-the-art multilayered absorbers, as well as carrying out an analysis of their power handling capabilities. As for their use as contact-less sensors, the next logical step could be the study of the stress-dependent scattering within a realistic environment.

Moreover, many antenna applications of ferromagnetic wires have been ruled out due to the presence of excessive losses. To overcome this limitation, the fabrication by means of the Taylor-Ulitovski technique of wires composed by a conductive core with a non-conductive magnetic coating could be investigated. If successful, one could benefit from the mass-production of wires with an acceptable level of losses.

Finally, the approximation of a uniform axial magnetization has been adopted along the dissertation. While the present experimental studies support the use of this approximation, many interesting phenomena could be discovered studying more complex, dynamic, magnetizations.

Appendices

Universidad Pública de Navarra
Nafarroako Unibertsitate Publikoa

Appendix A

Series of Hankel Functions

The aim of this Appendix is to derive the methods needed to compute the series of Hankel functions that arise along the dissertation. Although the series of Hankel functions can be computed numerically, alternative representations are required to accelerate the convergence of such series and to rewrite the series in a more intuitive manner. A fundamental tool to accelerate the convergence of such series is the Poisson summation formula, which is introduced in Section A.1, and it is systematically applied to transform series in Section A.2.

A.1 Poisson Summation Formula

The Poisson summation formula is named after Siméon Denis Poisson, and it is also labeled as Poisson resummation or Poisson summation rule. It is a common and powerful tool in applied electromagnetics [104], and it is usually adopted to accelerate the convergence of series that arise in periodic structures. Physically speaking, the formula transforms a series that illustrates how the field produced by a periodic structure is constructed from the individual contributions of the elements composing the structure, into a series in which the field is constructed from a set of structural modes, usually referred to as Floquet modes. From a mathematical standpoint, the Poisson summation formula relates the periodic sampling of a function to a sampling of the function's Fourier transform, and it can be stated as [128]

$$\sum_{n=-\infty}^{\infty} f\left(nd\right) = \frac{1}{d} \sum_{m=-\infty}^{\infty} \widehat{f}\left(\frac{m}{d}\right) \tag{A.1}$$

where $\widehat{f}(\xi)$ is the Fourier transform of $f(t)$, given by (see, e.g., (1.14.1) [129,130])

$$\widehat{f}(\xi) = \mathcal{F}\{f(t)\}(\xi) = \int_{-\infty}^{\infty} f(t)\, e^{-j2\pi\xi t} dt \tag{A.2}$$

The Poisson summation formula can be readily demonstrated by applying the Fourier transform definition

$$\sum_{m=-\infty}^{\infty} \widehat{f}(m) = \sum_{m=-\infty}^{\infty} \int_{-\infty}^{\infty} f(t)\, e^{-j2\pi mt} dt = \int_{-\infty}^{\infty} f(t) \left(\sum_{m=-\infty}^{\infty} e^{-j2\pi mt} \right) dt \tag{A.3}$$

and by identifying the Fourier series representation of the Dirac comb

$$\sum_{n=-\infty}^{\infty} \delta(t-n) = \sum_{m=-\infty}^{\infty} e^{-j2\pi mt} \tag{A.4}$$

so that the series reduces to

$$\sum_{m=-\infty}^{\infty} \widehat{f}(m) = \int_{-\infty}^{\infty} f(t) \left(\sum_{n=-\infty}^{\infty} \delta(t-n) \right) dt = \sum_{n=-\infty}^{\infty} f(n) \tag{A.5}$$

Finally, (A.1) is fully constructed by introducing the Fourier transform property

$$\mathcal{F}\{f(td)\}(\xi) = \frac{1}{d}\widehat{f}\left(\frac{\xi}{d}\right) \tag{A.6}$$

into (A.5).

A.2 Series of Hankel Functions

A.2.1 Series: S_{grid}

Let us define S_{grid} as the series

$$S_{\text{grid}} = \sum_{n=-\infty}^{\infty} H_0^{(2)}\left(k_0\sqrt{x^2+(y-nd)^2}\right) \tag{A.7}$$

Recall the Fourier transform of the Hankel function (see, e.g., [104] p. 72)

$$\int_{-\infty}^{\infty} H_0^{(2)}\left(k_0\sqrt{x^2+t^2}\right)e^{-j2\pi\xi t} = 2\frac{e^{-j\sqrt{k_0^2-(2\pi\xi)^2}|x|}}{\sqrt{k_0^2-(2\pi\xi)^2}} \tag{A.8}$$

with $\operatorname{Im}\left[k_0^2-(2\pi\xi)^2\right] < 0$. Invoking the Poisson summation formula, i.e., (A.1), with (A.8), S_{grid} can be rewritten as

$$S_{\text{grid}} = \frac{2}{d}\sum_{m=-\infty}^{\infty}\frac{e^{-jk_x^{(m)}|x|}e^{j\frac{2\pi m}{d}y}}{k_x^{(m)}} \tag{A.9}$$

where $k_x^{(m)} = \sqrt{k_0^2-\left(\frac{2\pi m}{d}\right)^2}$, with $\operatorname{Im}\left[k_x^{(m)}\right] < 0$. Taking the zero-term separately, it can also be written as

$$S_{\text{grid}} = \frac{2}{k_0 d}e^{-jk_0|x|} + \frac{4}{d}\sum_{m=1}^{\infty}\cos\left(\frac{2\pi m}{d}y\right)\frac{e^{-jk_x^{(m)}|x|}}{k_x^{(m)}} \tag{A.10}$$

A.2.2 Series: $S_{\text{int}}^{\text{grid}}$

Let us define $S_{\text{int}}^{\text{grid}}$ as the series

$$S_{\text{int}}^{\text{grid}} = \sum_{n\neq 0} H_0^{(2)}\left(k_0\,|nd|\right) \tag{A.11}$$

First of, note that (A.11) can be rewritten as the $x \to 0$ limit of (A.7) minus its $n=0$ term

$$S_{\text{int}}^{\text{grid}} = \lim_{x\to 0}\left\{\sum_{n=-\infty}^{\infty} H_0^{(2)}\left(k_0\sqrt{x^2+(nd)^2}\right) - H_0^{(2)}\left(k_0\,|x|\right)\right\} \tag{A.12}$$

Although both addends within the curly brackets are divergent, their singularity can be analytically cancelled out. To begin with, the second addend can be evaluated through small arguments of Bessel functions as

$$\lim_{x \to 0} \left\{ H_0^{(2)} \left(k_0 \left| x \right| \right) \right\} = 1 - j \frac{2}{\pi} \lim_{x \to 0} \left\{ \ln \left(\frac{k_0 \left| x \right|}{2} \right) + \gamma \right\} \tag{A.13}$$

Secondly, the series of Hankel functions can be rewritten by using the Poisson summation formula as in (A.10). Moreover, note that $k_x^{(m)} \to -j\frac{2\pi m}{d}$ for large n, so that (A.10) can be split into dominant and correction parts

$$\sum_{m=1}^{\infty} \frac{e^{-jk_x^{(m)}|x|}}{k_x^{(m)}} = \sum_{m=1}^{\infty} \left\{ \frac{e^{-jk_x^{(m)}|x|}}{k_x^{(m)}} - \frac{e^{-\frac{2\pi m}{d}|x|}}{-j\frac{2\pi m}{d}} \right\} + \sum_{m=1}^{\infty} \frac{e^{-\frac{2\pi m}{d}|x|}}{-j\frac{2\pi m}{d}} \tag{A.14}$$

Taking the $x \to 0$ limit on the right hand side (r.h.s.) of (A.14), the first added becomes a rapidly convergent series, so that the singularity is confined in to the second addend, which can be written in closed form by applying

$$\sum_{m=1}^{\infty} \frac{e^{-\frac{2\pi m}{d}|x|}}{m} = -\ln \left(1 - e^{-\frac{2\pi|x|}{d}} \right) \tag{A.15}$$

In this manner, the series $S_{\text{int}}^{\text{grid}}$ can be evaluated by introducing (A.15) into (A.14), and (A.14) into (A.10). Next, taking the $x \to 0$ limit of (A.10) and subtracting (A.13), which leads to

$$\begin{aligned} S_{\text{int}}^{\text{grid}} = & \frac{2}{k_0 d} - 1 + j\frac{4}{d} \sum_{m=1}^{\infty} \left(\frac{1}{jk_x^{(m)}} - \frac{1}{\frac{2\pi m}{d}} \right) \\ & + j\frac{2}{\pi} \lim_{x \to 0} \left\{ \ln \left(\frac{k_0 \left| x \right|}{2} \right) - \ln \left(1 - e^{-\frac{2\pi|x|}{d}} \right) + \gamma \right\} \end{aligned} \tag{A.16}$$

The singularity is removed by taking the Taylor series expansion of the exponential function $e^{-\frac{2\pi|x|}{d}} = 1 - \frac{2\pi|x|}{d} + \ldots$ so that $S_{\text{int}}^{\text{grid}}$ is finally written as

$$S_{\text{int}}^{\text{grid}} = \frac{2}{k_0 d} - 1 + j\frac{2}{\pi} \left[\ln \left(\frac{k_0 d}{4\pi} \right) + \gamma \right] + j\frac{4}{d} \sum_{m=1}^{\infty} \left(\frac{1}{jk_x^{(m)}} - \frac{1}{\frac{2\pi m}{d}} \right) \tag{A.17}$$

A.2.3 Series: S_{wg}

Let us define S_{wg} as the series

$$S_{\mathrm{wg}} = \sum_{n=-\infty}^{\infty} (-1)^n H_0^{(2)}\left(k_0\sqrt{x^2 + (y - nd)^2}\right) \tag{A.18}$$

Note that S_{wg} can be divided into two series gathering the even $(2n)$ and odd $(2n+1)$ elements, corresponding to positive and negative signs of $(-1)^n$, respectively

$$S_{\mathrm{wg}} = \sum_{n=-\infty}^{\infty} H_0^{(2)}\left(k_0\sqrt{x^2 + [y - (2n)\,d]^2}\right) - H_0^{(2)}\left(k_0\sqrt{x^2 + [y - (2n+1)\,d]^2}\right) \tag{A.19}$$

Decomposing both series as in (A.10) and adding the result, S_{wg} can be rewritten as

$$S_{\mathrm{wg}} = \frac{2}{d}\sum_{m=1}^{\infty} \frac{e^{-jk_{\mathrm{wg},x}^{(m)}|x|}}{k_{\mathrm{wg},x}^{(m)}}\left[\cos\left(\frac{\pi m}{d}y\right) - \cos\left(\frac{\pi m}{d}(y-d)\right)\right] \tag{A.20}$$

with $k_{\mathrm{wg},x}^{(m)} = \sqrt{k_0^2 - \left(\frac{\pi m}{d}\right)^2}$, $\mathrm{Im}\left[k_{\mathrm{wg},x}^{(m)}\right] < 0$. Finally, let us make use of the following trigonometric identities

$$\cos A - \cos B = -2\sin\left(\frac{A+B}{2}\right)\sin\left(\frac{A-B}{2}\right) \tag{A.21}$$

$$\sin(A \pm B) = \sin(A)\cos(B) \pm \cos(A)\sin(B) \tag{A.22}$$

to write S_{wg} in the form of the modes of a rectangular waveguide

$$S_{\mathrm{wg}} = \frac{4}{d}\sum_{m=1,3\ldots} \cos\left(\frac{\pi m}{d}y\right)\frac{e^{-jk_{\mathrm{wg},x}^{(m)}|x|}}{k_{\mathrm{wg},x}^{(m)}} \tag{A.23}$$

A.2.4 Series: $S_{\mathrm{int}}^{\mathrm{wg}}$

Let us define $S_{\mathrm{int}}^{\mathrm{wg}}$ as the series

$$S_{\mathrm{int}}^{\mathrm{wg}} = \sum_{n\neq 0} (-1)^n H_0^{(2)}(k_0|nd|) \tag{A.24}$$

Let us follow the singularity cancellation procedure develop in Section A.2.2. First of, note that (A.24) can be rewritten as the $x \to 0$ limit of (A.18) minus its $n = 0$ term

$$S_{\text{int}}^{\text{wg}} = \lim_{x \to 0} \left\{ \sum_{n=-\infty}^{\infty} (-1)^n \, H_0^{(2)} \left(k_0 \sqrt{x^2 + (nd)^2} \right) - H_0^{(2)} \left(k_0 \left| x \right| \right) \right\} \tag{A.25}$$

Again, both addends within the curly brackets are divergent. The second addend can be evaluated as in (A.13). The first addend can be expressed as in (A.23), and then written in terms of dominant and correction series by noting $k_{\text{wg},x}^{(m)} \to -j\frac{\pi m}{d}$ for large n

$$\sum_{m=1,3...} \frac{e^{-jk_{\text{wg},x}^{(m)}|x|}}{k_{\text{wg},x}^{(m)}} = \sum_{m=1,3...} \left(\frac{e^{-jk_{\text{wg},x}^{(m)}|x|}}{k_{\text{wg},x}^{(m)}} - \frac{e^{-\frac{\pi m}{d}|x|}}{-j\frac{\pi m}{d}} \right) + \sum_{m=1,3...} \frac{e^{-\frac{\pi m}{d}|x|}}{-j\frac{\pi m}{d}} \tag{A.26}$$

The first addend on the r.h.s. of (A.26) becomes a rapidly convergent series when taking the $x \to 0$ limit. In this manner, the singularity is confined in to the second addend, which can be written in closed form by applying (see, e.g. [59] p. 409)

$$\sum_{m=1,3...} \frac{e^{-\frac{\pi m}{d}|x|}}{m} = \frac{1}{2} \ln \left(\frac{1 + e^{-\frac{\pi}{d}|x|}}{1 - e^{-\frac{\pi}{d}|x|}} \right) \tag{A.27}$$

Therefore, the series $S_{\text{int}}^{\text{wg}}$ can be evaluated by introducing (A.27) into (A.26), and (A.26) into (A.10). Next, taking the $x \to 0$ limit of (A.10) and subtracting (A.13), which leads to

$$\begin{aligned} S_{\text{int}}^{\text{wg}} &= -1 + j\frac{4}{d} \sum_{m=1,3...} \left(\frac{1}{jk_{\text{wg},x}^{(m)}} - \frac{1}{\frac{\pi m}{d}} \right) \\ &+ j\frac{2}{\pi} \lim_{x \to 0} \left\{ \ln \left(\frac{1 + e^{-\frac{\pi}{d}|x|}}{1 - e^{-\frac{\pi}{d}|x|}} \right) + \ln \left(\frac{k_0 \left| x \right|}{2} \right) + \gamma \right\} \end{aligned} \tag{A.28}$$

Again, The singularity is removed by taking the Taylor series expansion of the exponential function $e^{-\frac{\pi|x|}{d}} = 1 - \frac{\pi|x|}{d} + \ldots$ so that $S_{\text{int}}^{\text{wg}}$ is finally written as

$$S_{\text{int}}^{\text{wg}} = -1 + j\frac{2}{\pi} \left[\ln \left(\frac{k_0 d}{\pi} \right) + \gamma \right] + j\frac{4}{d} \sum_{m=1,3...} \left(\frac{1}{jk_{\text{wg},x}^{(m)}} - \frac{1}{\frac{\pi m}{d}} \right) \tag{A.29}$$

Appendix B

Impact of the Pyrex Coating

The impact of the Pyrex coating on the wire response is neglected along the dissertation. In fact, the same assumption is implicit in previous theoretical studies on the electromagnetic response of the wires both for infinitely-long [17, 58] and finite-length [34] wires. This Appendix tries to further justify such assumption with some numerical simulations and discussion of the results.

Initially, the assumption can be based on the weak dielectric response of Pyrex ($\epsilon_p \simeq 4.9$) as compared to that of the conductive ferromagnetic core ($\sigma \sim 10^5\,\mathrm{S/m}$). Additionally, this dielectric coating is placed in a minimum of electric field for wires behaving as good conductors.

Let us run a numerical simulation to test this intuition. To this end, the scattering problem addressed in Refs. [17, 58] must be completed with an additional cylindrical region. The result is a new wire with radius $a_\mathrm{c} = a + t$, where t is the thickness of the coating, and with a new distributed impedance, Z_w^c, which is found to be equal to

$$Z_\mathrm{w}^\mathrm{c} = \frac{j\eta_\mathrm{c}}{2\pi a_\mathrm{c}} \frac{J_0\left(k_\mathrm{c} a_\mathrm{c}\right) + T_1 \cdot H_0^{(2)}\left(k_\mathrm{c} a_\mathrm{c}\right)}{J_0'\left(k_\mathrm{c} a_\mathrm{c}\right) + T_1 \cdot H_0'^{(2)}\left(k_\mathrm{c} a_\mathrm{c}\right)} \tag{B.1}$$

with

$$T_1 = \frac{Z_\mathrm{w} J_0'\left(k_\mathrm{c} a\right) - \frac{j\eta_\mathrm{c}}{2\pi a} J_0\left(k_\mathrm{c} a\right)}{\frac{j\eta_\mathrm{c}}{2\pi a} H_0^{(2)}\left(k_\mathrm{c} a\right) - Z_\mathrm{w} H_0'^{(2)}\left(k_\mathrm{c} a\right)} \tag{B.2}$$

where η_c and k_c stand for the medium impedance and propagation constant inside the coating, and Z_w is the wire distributed impedance of the uncoated wire, given by (2.40).

Fig. B.1 represents the absorption spectrum of both, an infinitely-long, and a $2L = 9.8$ mm long ferromagnetic wire of $a = 22.5$ μm radius,

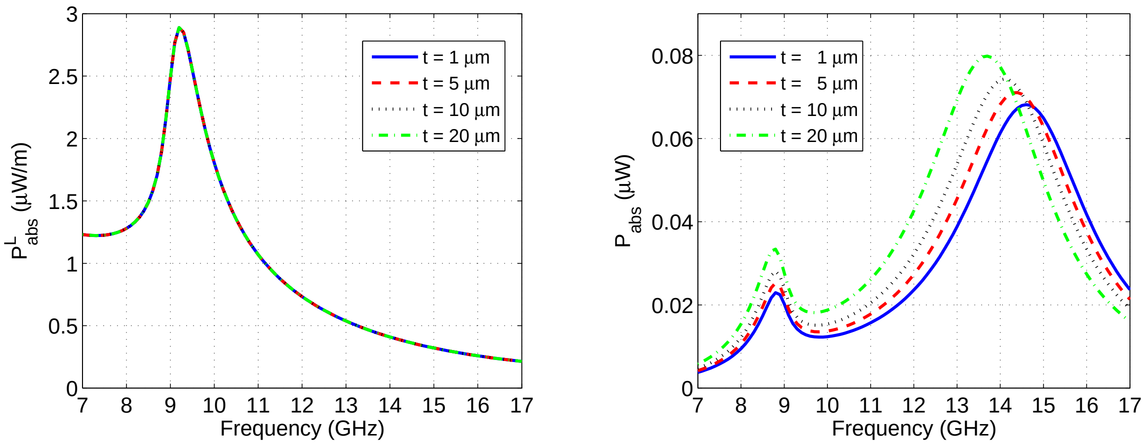

(a) (b)

Figure B.1 – Absorption spectrum of (a) an infinitely-long and (b) a $2L = 9.8$ mm long Co-rich ferromagnetic wire of $a = 22.5\,\mu$m radius, and covered by with different Pyrex coatings of thickness 1 μm, 5 μm, 10 μm and 20 μm

.

covered by different Pyrex coatings of thickness 1 μm, 5 μm, 10 μm and 20 μm. It can be concluded that the Pyrex coating has a negligible impact on the absorption spectrum of infinitely-long ferromagnetic wires. On the contrary, the coating is shown to shift down in frequency absorption peak corresponding to an axial resonance in finite-length wires. This behavior can be justified at a field level. To this end, note that the electric field excited by an infinitely long wire is perfectly tangential to the surface of the wire. Thus, if the uncoated wire is a good conductor, there is almost no electric field within the coating, and the impact of the coating is negligible. By contrast, radial electric fields are excited by finite size dipoles, leading to non-vanishing electric fields perpendicular to the wire even in the surface of the good conductor, i.e., within the coating. Therefore, the impact of the coating is larger in finite-size wires than in infinitely-long wires. Moreover, it is found that the main effect of the coating is to shift down in frequency the absorption peak produced by an axial resonance. However, it is worth remarking, that this effect is still much smaller than the one that would be produced by a magnetic coating.

Appendix C

Alternative Implementations of Artificial Impedance Surfaces

Chapter 6 reveals that the ferromagnetic wires considered in this dissertation are too lossy to sustain the necessary resonance to develop low-profile artificial impedance surfaces. However, it is also pointed out that alternative implementations, e.g., conductive wires loaded with lumped elements, and/or conductive wires coated with a non-conductive magnetic layer, could be able to overcome this problem. This Appendix gathers a more exhaustive analysis of the performance of such alternative implementations, including the numerical validation of the analytical model, bandwidth considerations, and a study of the robustness of the system against variations in the angle-of-arrival of the incoming plane wave.

C.1 Numerical Validation

The results presented in Chapter 6 are based on an analytical treatment of the problem. In such a treatment, the theory is derived from the well-known scattering from impedance loaded wires and the local field method, with the only approximation that the wires are electrically thin, condition which is easily satisfied. Therefore, although the solutions are presented in simple, analytically-closed forms, they are indeed the complete solution to the problem and thus more accurate than solutions provided by numerical solvers. This is particularly true for systems based on magnetic wires, since the simulation of such wires requires the discretization of very small

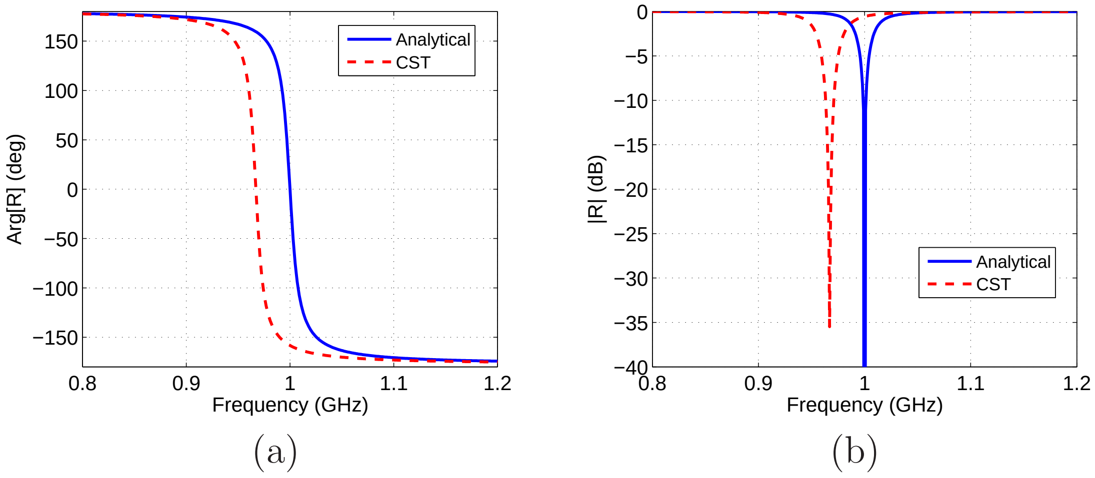

(a) (b)

Figure C.1 – Comparison between numerical (CST) and analytical solutions. The geometry is composed of a grid of parallel conductive wires of $a = 0.001\lambda_0$ radius, periodically loaded ($p = \lambda_0/10$) with a lumped capacitance $C = 1.38$ pF. The separation between wires is of $d = 0.1\lambda_0$ and grid is placed at $h = 0.01\lambda_0$ to the ground plane. The frequency of operation is set at 1 GHz. (a) Phase of the reflection coefficient for lossless wires. (b) Magnitude of the reflection coefficient for wires loaded with lumped resistors of 1.5 Ω.

details (i.e., the wire radius) compared to the wavelength of operation, complex constitutive parameters (i. e., finite conductivity and gyrotropic permeability tensor), and rapid variations of the electromagnetic fields inside the wires.

Despite this, it is always desirable to test the theory against full-wave simulations. To this end, an example has been simulated using CST commercial software [124]. To avoid the complexity arising from ferromagnetic wires, the geometry corresponds to a conductive wire loaded with lumped elements. In addition, the geometry has been scaled with respect to a central frequency of operation equal to 1 GHz. Namely, a grid of parallel conductive wires of $a = 0.001\lambda_0$ radius, periodically loaded ($p = \lambda_0/10$) with a lumped capacitance $C = 1.38$ pF. The separation between the wires of $d = 0.1\lambda_0$ and the grid is placed at the distance $h = 0.01\lambda_0$ to the ground plane. In the CST model, a period of the wire is placed parallel to magnetic walls to simulate the grid of wires, and cut by electrical walls to simulate infinitely long wires. The capacitor has been introduced in a gap of 0.01 λ_0 width. In order to ensure the convergence of the results, the structure has been meshed on a Cartesian grid with the minimum spatial increment $\Delta h = \lambda_{\mathrm{up}}/45$, where λ_{up} is the wavelength at the highest frequency of operation. Moreover, the simulation has been run until the energy limit of -80 dB inside the calculation domain.

The phase of the reflection coefficient for this structure with lossless wires is shown in Fig. C.1(a). Both CST and the analytical approach predict the resonance with similar bandwidth. However, the frequency at which the phase of the reflection coefficient is zero for the CST solution is 3.3% shifted from 1 GHz. At the first sight, this deviation might be caused by the additional capacitance produced by the gap between the wires, though this explanation is discarded since the same result is reproduced with different numerical simulations for distinct gap lengths.

As anticipated, an absorbing boundary is obtained by loading the wires with a certain resistance. This is evidenced in Fig. C.1(b), which represents the magnitude of the reflection coefficient for the same structure but wires with an additional resistive load of 1.5 Ω. As expected, the analytical reflection coefficient completely vanishes at the resonance frequency (1 GHz). The numerical results cannot exactly equal zero, but the reflection coefficient is reduced up to -35.5 dB, which demonstrates an excellent agreement between analytical theory and full-wave simulation.

C.2 Bandwidth Considerations

Eq. (6.19) reveals that the reactance required to satisfy the resonant condition, X_w, is a function of frequency. Although a frequency independent reflection coefficient is in theory possible with a load designed to follow such specific frequency dependence, the implementation of such load would require non-Foster elements [118], and in practice the operational bandwidth is finite.

Fig. C.2 represents the frequency behavior of the required reactance, as well as the reactance implemented with a capacitor and with a conductive wire covered by a magnetic coating. The dimensions have been selected so that the magnetically coated wire satisfies the absorber condition ($R_\mathrm{w} = \eta/d \cdot \sin^2(k_0 h)$) which will be employed in another example. It can be concluded that the required load follows a soft and almost linear progression with a negative slope. The implementation of this negative slope would require non-Foster elements [118], in contrast to the passive implementations represented in Fig. C.2, which produce reactances that increases with frequency. However, the non-resonant behavior of X_w could be considered a great advantage: the system is robust against tolerances of the loads, and the design of reconfigurable loads is simple.

Consider first an implementation with distributed capacitive load with frequency dependence $X_\mathrm{w} = -j/\omega C_\mathrm{w}$, so that C_w satisfies the resonant condition at a certain frequency ω_0. On the contrary, the distributed resistance, R_w, is supposed to be frequency independent. In order to illustrate the influence of the system geometry on the bandwidth, Fig. C.3 represents the frequency behavior of the reflection coefficient phase for lossless wires with different distances to the ground plane and separation between wires. As expected, the phase of the reflection coefficient is zero at the resonant frequency, and the operational bandwidth is enhanced by increasing the distance to the ground plane and grid density. This appears intuitive since the closer the grid is to the ground plane, the stronger must be the resonance to compensate the null of electric field, and typically, the stronger the resonance the smaller the bandwidth. As usual, the result is a trade-off between the bandwidth, profile and complexity of the geometry.

A similar result is obtained for the system operating as an absorber, as shown in Fig. C.4, which represents the frequency behaviour of the reflection coefficient magnitude for the same configuration but with the wires having resistance per unit length $R_\mathrm{w} = \eta/d \cdot \sin^2(k_0 h)$, where k_0 is the propagation constant at the resonant frequency.

For systems based on magnetic wires, the frequency behavior is not

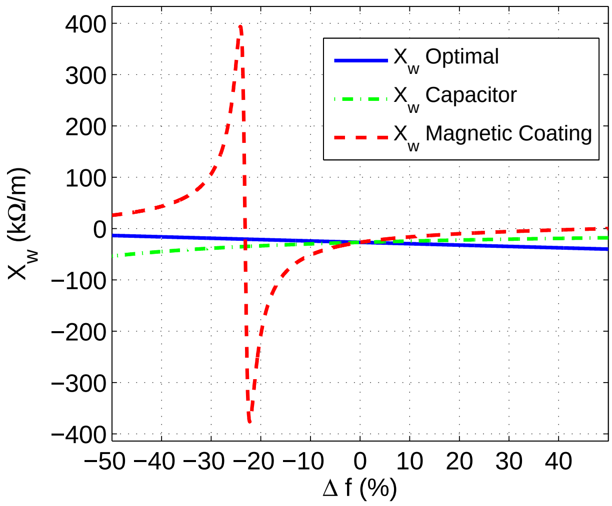

Figure C.2 – Frequency behavior of the required reactance, reactance implemented with a capacitor and reactance implemented with a conductive wire covered by a magnetic coating. The grid is placed at a distance $h = 0.02\lambda_0$ to the ground plane, and with $d = 0.1\lambda_0$ separation between the wires of the grid. The wire radius is of $a = 0.006\lambda_0$, and, in the case of magnetically coated wires, the coating has a thickness $t = a/2$.

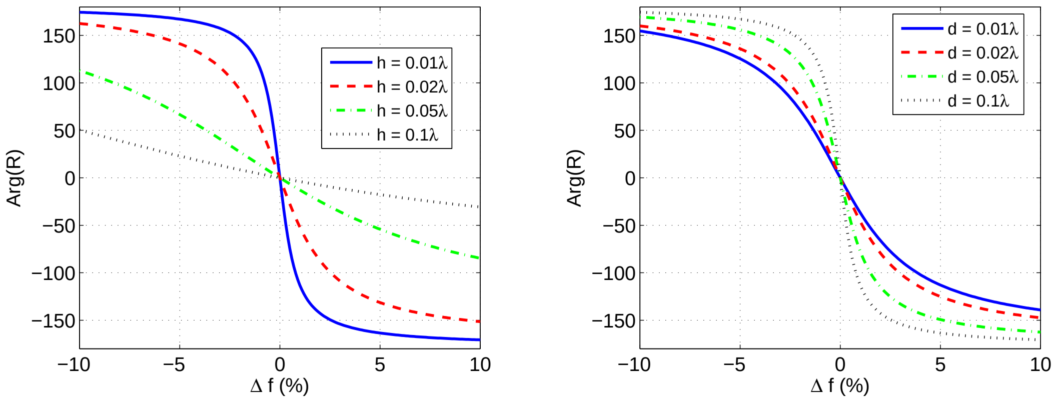

(a) (b)

Figure C.3 – Frequency behavior of the reflection coefficient phase for lossless ($R_\text{w} = 0$) wires with (a) different distances to the ground plane and $d = 0.1\lambda$ and (b) different separation between wires and $h = 0.01\lambda$.

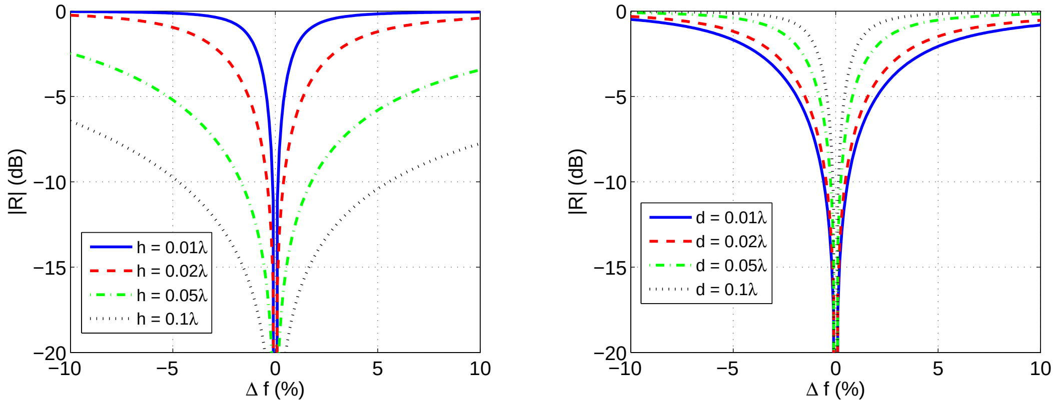

(a) (b)

Figure C.4 – Frequency of the reflection coefficient magnitude for lossy ($R_\text{w} = \eta/d \cdot \sin^2(k_0 h)$) wires with (a) different distances to the ground plane and $d = 0.1\lambda$ and (b) different separation between wires and $h = 0.01\lambda$.

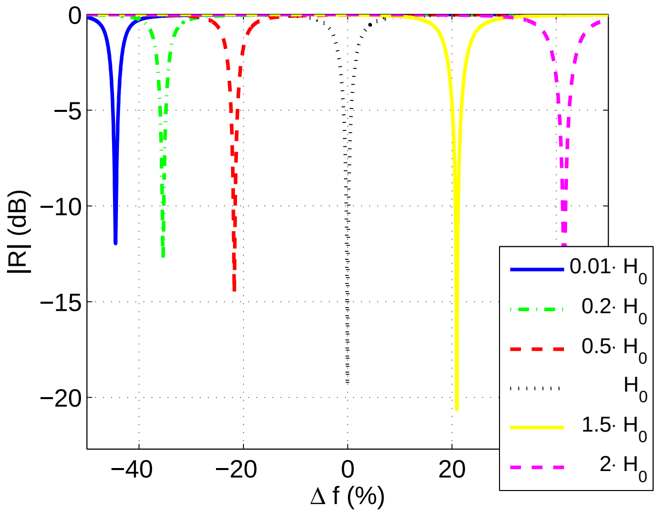

Figure C.5 – Magnitude for the reflection coefficient for a grid of magnetically coated wires as a function of frequency and with different DC magnetic fields. The grid is placed at a distance $h = 0.02\lambda_0$ to the ground plane, and with $d = 0.1\lambda_0$ separation between the wires of the grid. The wire radius is of $a = 0.006\lambda_0$ and the coating has a thickness $t = a/2$.

so simple due to the frequency dispersive behavior of the distributed impedance. Loosely speaking, the bandwidth should be smaller than in the capacitive load case for wires operating close to the FMR, while it should be comparable or larger for wires operating far away from the FMR. Furthermore, the correlation between the grid geometry and the bandwidth is the same as in the capacitor case. Moreover, due to the Lorentzian frequency dispersion of the wire distributed impedance, there are in general two frequencies where the required reactance is met (see Fig. C.2). Although this makes in theory possible a dual-frequency operation, the first frequency corresponds to a very lossy and highly dispersive load.

The main advantage of using magnetic wires is the tunability. To illustrate this point, Fig. C.5 represents the magnitude of the reflection coefficient as a function of the frequency for the scenario described in Fig. C.2 for different magnetic fields of $0.01 \cdot H_0$, $0.2 \cdot H_0$, $0.5 \cdot H_0$, H_0, $1.2 \cdot H_0$, $1.5 \cdot H_0$, where H_0 is the DC magnetic field which satisfies the resonant absorber condition at ω_0. It can be concluded that the system can be tuned over a wide frequency range with a minor impact on the performance.

C.3 Angle-Of-Arrival Dependency

In order to illustrate the influence of the Angle-Of-Arrival (AOA) on the system performance, let us rewrite the reflection coefficient, (6.10), as

$$R = -1 + \frac{2\sin^2\left(k_{\mathrm{x}}h\right)}{\frac{k_{\mathrm{x}}}{k_0}\frac{dR_{\mathrm{w}}}{\eta_0} + \sin^2\left(k_{\mathrm{x}}h\right) + j\frac{k_{\mathrm{x}}}{2}\zeta} \tag{C.1}$$

with

$$\begin{aligned}\zeta = \left[\frac{\sin\left(2k_{\mathrm{x}}h\right)}{k_{\mathrm{x}}} - \frac{\sin\left(2k_0h\right)}{k_0}\right] - \sum_{m\neq 0}\left[\frac{e^{-2q_m^{\mathrm{a}}h}}{q_m^{\mathrm{a}}} - \frac{e^{-2q_m h}}{q_m}\right]& \\ + \sum_{m\neq 0}\left[\frac{1}{q_m^{\mathrm{a}}} - \frac{1}{q_m}\right]&\end{aligned} \tag{C.2}$$

where $\left(q_{\mathrm{m}}^{\mathrm{a}}\right)^2 = \left(k_{\mathrm{y}} + 2\pi\mathrm{m}/d\right)^2 - k_r^2$.

For the case of the system operating as a reactive high-impedance surface ($R_{\mathrm{w}} = 0$) the reflection coefficient simplifies to

$$R = -1 + \frac{2}{1 + j\frac{k_{\mathrm{x}}}{2\sin^2\left(k_{\mathrm{x}}h\right)}\zeta} \tag{C.3}$$

In the case of lossless wires, the magnitude of the reflection coefficient is equal to unity. However, $\zeta \neq 0$ for oblique incidence, affecting the phase of the reflection coefficient. The first term of ζ comes from the differences in the phase of the reflected plane wave, the second term from the differences in the coupling with evanescent Floquet modes, and the third term from differences of coupling inside the grid. For large h, the first term is dominant and the angular response is independent on d. Conversely, for small h all terms contribute and the second and third terms increase along with d.

Let us first focus on variations in the elevation angle, θ_{inc}. In that case, $q_m^{\mathrm{a}} > q_m$, so that both terms have the opposite sign. Therefore, it is possible to to find the optimal values of h and d that inhibits the angular dependency in the elevation angle, as it is shown in Fig. C.6(a). On the contrary, for variations in the azimuthal angle, ϕ_{inc}, it is found that $q_m^{\mathrm{a}} > q_m$ for $m > 0$ and $q_m^{\mathrm{a}} < q_m$ for $m < 0$. Since the $q_m^{\mathrm{a}} < q_m$ addends dominate, the second and third terms of Eq. C.2 are positive and the angular dependence gets stronger along with their value. In

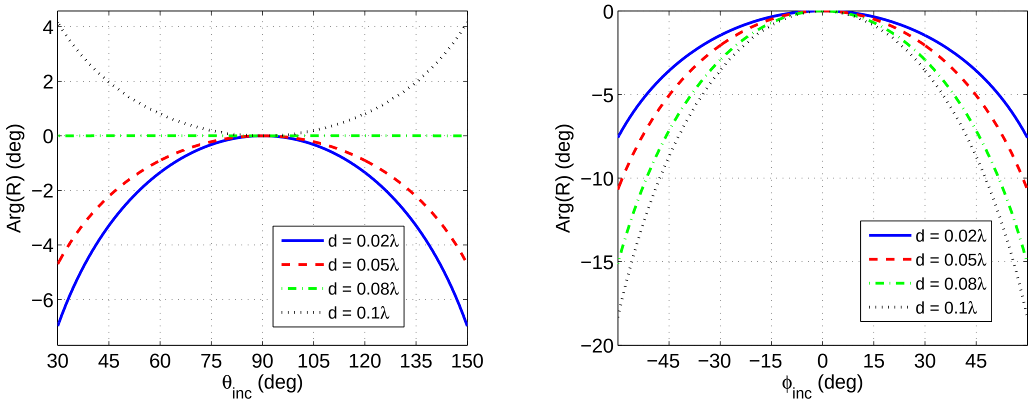

(a) (b)

Figure C.6 – Phase of the reflection coefficient as a function of the θ_{inc} (a) and the ϕ_{inc} (b) angles of arrival for a grid of lossless wires ($R_{\text{w}} = 0$) at the distance $h = 0.01\lambda$ to the ground plane and different values of the separation between wires $d = 0.02\lambda$, $d = 0.05\lambda$, $d = 0.08\lambda$ and $d = 0.1\lambda$.

other words, the angular performance in the azimuthal angle degrades for sparser grids ($\uparrow d$) and lower profiles ($\downarrow h$). This is evidenced in Fig. C.6(b), which represents the phase of the reflection coefficient as a function of the angle of arrival for a system satisfying the high-impedance condition under normal incidence.

As for the case of absorber operation ($R_{\text{w}} = \eta_0/d \cdot \sin^2(k_0 h)$), the impact of small changes in ζ is negligible and, approximating $\sin^2(x) \simeq x^2$, the reflection coefficient simplifies to

$$R = -1 + \frac{2}{1 + \frac{1}{\cos(\phi)\sin(\theta)}} \tag{C.4}$$

Strikingly, the angular response of the system is geometry-independent. This fact is evidenced in Fig. C.7, which represents the magnitude of the reflection coefficient as a function of the angle of arrival for a grid of lossy wires satisfying the absorbing boundary condition.

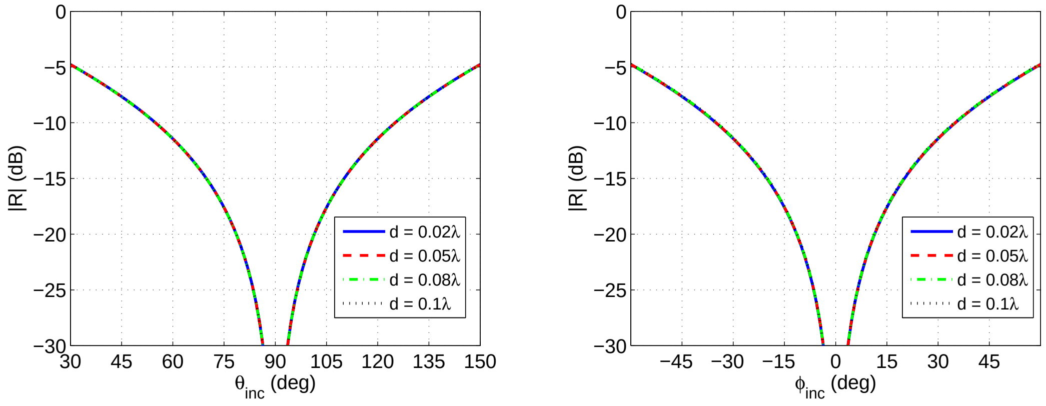

(a) (b)

Figure C.7 – Magnitude of the reflection coefficient as a function of the θ_{inc} (a) and the ϕ_{inc} (b) angles of arrival for a grid lossy wires ($R_{\text{w}} = \eta/d \cdot \sin^2(k_0 h)$) at the distance $h = 0.01\lambda$ to the ground plane and different values of the separation between wires $d = 0.02\lambda$, $d = 0.05\lambda$, $d = 0.08\lambda$ and $d = 0.1\lambda$.

Bibliography

[1] M. Vázquez and A. Adenot-Engelvin, “Glass-coated amorphous ferromagnetic microwires at microwave frequencies,” *J. Magn. Magn. Mater.*, vol. 321, no. 14, pp. 2066–2073, Jul. 2009.

[2] H. Chiriac and T. Ovari, “Amorphous Glass-Covered Magnetic Wires: Preparation, Properties, Applications,” *Progress in Material Science*, vol. 40, no. 5, pp. 333–407, 1996.

[3] A. Zhukov, M. Vázquez, J. Velázquez, A. Hernando, and V. Larin, “Magnetic properties of fe-based glass-coated microwires,” *J. Magn. Magn. Mater.*, vol. 170, no. 3, pp. 323–330, 1997.

[4] L. V. Panina, K. Mohri, K. Bushida, and M. Noda, “Giant magneto-impedance and magneto-inductive effects in amorphous alloys (invited),” *J. Appl. Phys.*, vol. 76, no. 10, p. 6198, 1994.

[5] A. Zhukov, A. F. Cobeno, J. Gonzalez, A. Torcunov, E. Pina, M. J. Prieto, J. M. Blanco, V. Larin, and S. Baranov, “Ferromagnetic resonance, magnetic behaviour and structure of fe-based glass-coated microwires,” *J. Magn. Magn. Mater.*, vol. 203, no. 1, pp. 238–240, 1999.

[6] M. Vázquez, M. Knobel, M. L. Sanchez, R. Valenzuela, and A. P. Zhukov, “Giant magnetoimpedance effect in soft magnetic wires for sensor applications,” *Sensors and Actuators A: Physical*, vol. 59, no. 1-3, pp. 20–29, Apr. 1997.

[7] G. Taylor, “A Method of Drawing Metallic Filaments and a Discussion of Their Properties and Uses,” *Phys. Rev.*, vol. 23, no. 5, pp. 655–660, 1924.

[8] A. Ulitovski and N. Avernin, “Method of fabrication of metallic microwire,” p. 14, 1964.

[9] V. Larin, A. Torcunov, A. Zhukov, J. González, M. Vazquez, and L. Panina, “Preparation and properties of glass-coated microwires,” *J. Magn. Magn. Mater.*, vol. 249, no. 1-2, pp. 39–45, Aug. 2002.

[10] H. Chiriac, S. Corodeanu, M. Lostun, G. Ababei, and T. A. Óvári, “Magnetic behavior of rapidly quenched submicron amorphous wires,” *J. Appl. Phys.*, vol. 107, no. 9, pp. 09A301–09A303, 2010.

[11] H. Chiriac, S. Corodeanu, M. Lostun, G. Stoian, G. Ababei, and T. A. Óvári, "Rapidly solidified amorphous nanowires," *J. Appl. Phys.*, vol. 109, no. 6, pp. 063 902–063 904, 2011.

[12] H. Chiriac, "Preparation and characterization of glass covered magnetic wires," *Mater. Sci. Engineering: A*, vol. 304-306, pp. 166–171, May 2001.

[13] E. H. C. P. Sinnecker, D. Páramo, V. Larin, A. Zhukov, M. Vázquez, A. Hernando, and J. González, "Glass coated microwires with enhanced coercivity," *J. Magn. Magn. Mater.*, vol. 203, pp. 54–56, 1999.

[14] P. Marin, M. Vazquez, J. Arcas, and A. Hernando, "Thermal dependence of magnetic properties in nanocrystalline FeSiBCuNb wires and microwires," *J. Magn. Magn. Mater.*, vol. 203, pp. 6–11, 1999.

[15] H. Chiriac, N. Lupu, V. Dobrea, and S. Corodeanu, "Mechanical properties of magnetic Fe-based and Co-based amorphous wires and microwires," *Phys. Status Solidi A*, vol. 206, no. 4, pp. 648–651, Apr. 2009.

[16] J. Velázquez, M. Vázquez, D. X. Chen, and A. Hernando, "Giant Magnetoimpedance in nonmagnetostrictive amorphous wires," *Phys. Rev. B*, vol. 50, no. 22, pp. 737–740, 1994.

[17] D. Menard, M. Britel, P. Ciureanu, and A. Yelon, "Giant magnetoimpedance in a cylindrical magnetic conductor," *J. Appl. Phys.*, vol. 84, no. 5, p. 2805, 1998.

[18] M. Knobel, M. L. Sanchez, C. Gomez-Polo, P. Marin, M. Vázquez, and A. Hernando, "Giant magneto-impedance effect in nanostructured magnetic wires," *J. Appl. Phys.*, vol. 79, no. 3, pp. 1646—-1654, 1996.

[19] K. V. Rao, F. B. Humphrey, and J. L. Costa-Kramer, "Very large magneto-impedance in amorphous soft ferromagnetic wires," *J. Appl. Phys.*, vol. 76, no. 10, p. 6204, 1994.

[20] L. V. Panina, D. P. Makhnovskiy, and K. Mohri, "Magnetoimpedance in amorphous wires and multifunctional applications: from sensors to tunable artificial microwave materials," *J. Magn. Magn. Mater.*, vol. 272-276, pp. 1452–1459, May 2004.

[21] D. Yong-jian, J. Jian-jun, D. Gang, T. Bin, B. Shao-wei, and H. Hua-hui, "Magnetic and Microwave Properties of Glass-Coated Amorphous Ferromagnetic Microwires," *Trans. Nonferrous Met. Soc. China*, vol. 17, pp. 1352–1357, Jul. 2007.

[22] D. Pozar, *Microwave Engineering.* Wiley & Sons, 2005.

[23] A. G. Gurevich and G. A. Melkov, *Magnetization Oscillations and Waves.* CRC Press, New York, 1996.

[24] S. E. Lofland, H. García-Miquel, M. Vázquez, and S. Bhagat, "Microwave magnetoabsorption in glass-coated amorphous microwires with radii close to skin depth," *J. Appl. Phys.*, vol. 92, no. 4, p. 2058, 2002.

[25] L. Kraus, G. Infante, Z. Frait, and M. Vázquez, "Ferromagnetic resonance in microwires and nanowires," *Phys. Rev. B*, vol. 83, no. 17, pp. 4438–4449, May 2011.

[26] F. Yildiz, B. Z. Rameev, S. I. Tarapov, L. R. Tagirov, and B. Aktas, "High-frequency magnetoresonance absorption in amorphous magnetic microwires," *J. Magn. Magn. Mater.*, vol. 247, no. 2, pp. 222–229, Jun. 2002.

[27] G. Goglio, S. Pignard, A. Radulescu, L. Piraux, I. Huynen, D. Vanhoenacker, and A. V. Vorst, "Microwave properties of metallic nanowires," *Appl. Phys. Lett.*, vol. 75, no. 12, pp. 1769–1772, 1999.

[28] H. García-Miquel, M. Esbri, J. Andres, J. Garcia, J. Garcia-Beneytez, and M. Vázquez, "Power absorption and ferromagnetic resonance in Co-rich metallic glasses," *IEEE Trans. Magn.*, vol. 37, no. 1, pp. 561–564, 2001.

[29] N.-E. Belhadj-Tahar, A. Fourrier-Lamer, and H. de Chanterac, "Broad-band simultaneous measurement of complex permittivity and permeability using a coaxial discontinuity," *IEEE Trans. Microwave Theory Tech.*, vol. 38, no. 1, pp. 1–7, 1990.

[30] J. Garcia-Beneytez, F. Vinai, L. Brunetti, H. García-Miquel, and M. Vázquez, "Study of magneto impedance effect in the microwave frequency range for soft magnetic wires and microwires," *Sensors and Actuators A: Physical*, vol. 81, no. 1-3, pp. 78–81, Apr. 2000.

[31] A. Labrador, C. Gómez-Polo, J. Pérez-Landazabal, V. Zablotskii, I. Ederra, R. Gonzalo, G. Badini-Confalonieri, and M. Vázquez, "Magnetotunable left-handed FeSiB ferromagnetic microwires." *Opt. Lett.*, vol. 35, no. 13, pp. 2161–2163, Jul. 2010.

[32] J. Torrejón, G. Badini Confalonieri, K. Pirota, and M. Vázquez, "Multifunctional magnetoelastic sensor device based in multilayer magnetic microwires," *Sensor Lett.*, vol. 5, no. 1, pp. 153–156, 2007.

[33] O. Reynet, A. Adenot-Engelvin, S. Deprot, O. Acher, and M. Latrach, "Effect of the magnetic properties of the inclusions on the high-frequency dielectric response of diluted composites," *Phys. Rev. B*, vol. 66, no. 9, pp. 1–9, Sep. 2002.

[34] D. P. Makhnovskiy and L. V. Panina, "Field dependent permittivity of composite materials containing ferromagnetic wires," *J. Appl. Phys.*, vol. 93, no. 7, p. 4120, 2003.

[35] N. Haider, D. Caratelli, and A. G. Yarovoy, "Recent Developments in Reconfigurable and Multi-Band Antenna Technology ," *Int. J. Antennas Propag.*, p. 869170, 2013.

[36] H. García-Miquel, J. Carbonell, and J. Sánchez-Dehesa, "Left handed material based on amorphous ferromagnetic microwires tunable by dc current," *Appl. Phys. Lett.*, vol. 97, no. 9, p. 094102, 2010.

[37] M. Ipatov, V. Zhukova, A. Zhukov, and J. Gonzalez, "Magnetoimpedance sensitive to dc bias current in amorphous microwires," *Appl. Phys. Lett.*, vol. 97, no. 25, p. 252507, 2010.

[38] M. Ipatov, V. Zhukova, A. Zhukov, J. Gonzalez, and A. Zvezdin, "High frequency magneto impedance in amorphous microwires," *J. Phys.: Conf. Series*, vol. 200, no. 8, p. 082009, Jan. 2010.

[39] M. Ipatov, A. Chizhik, V. Zhukova, J. Gonzalez, and A. Zhukov, "Correlation of surface domain structure and magneto-impedance in amorphous microwires," *J. Appl. Phys.*, vol. 109, no. 11, p. 113924, 2011.

[40] D. P. Makhnovskiy and L. V. Panina, "Experimental demonstration of tunable scattering spectra at microwave frequencies in composite media containing CoFeCrSiB glass-coated amorphous ferromagnetic wires and comparison with theory," *Phys. Rev. B*, vol. 74, no. 6, pp. 1–11, Aug. 2006.

[41] M. Ipatov, V. Zhukova, L. V. Panina, and A. Zhukov, "Ferromagnetic Microwires Composite Metamaterials with Tuneable Microwave Electromagnetic Parameters," *PIERS*, vol. 5, no. 6, pp. 586–590, 2009.

[42] L. V. Panina, S. I. Sandacci, and D. P. Makhnovskiy, "Stress effect on magnetoimpedance in amorphous wires at gigahertz frequencies and application to stress-tunable microwave composite materials," *J. Appl. Phys.*, vol. 97, no. 1, p. 013701, 2005.

[43] D. Menard, M. Britel, P. Ciureanu, a. Yelon, V. P. Paramonov, a. S. Antonov, P. Rudkowski, and J. O. Strom-Olsen, "High frequency impedance spectra of soft amorphous fibers," *J. Appl. Phys.*, vol. 81, no. 8, p. 4032, 1997.

[44] J. Torrejón, G. a. Badini-Confalonieri, and M. Vázquez, "Multipeak ferromagnetic resonance behaviour tailored by magnetoelastic coupling in FeSiB/CoNi layered microwires," *J. Phys. D: Appl. Phys.*, vol. 43, no. 14, p. 145001, Apr. 2010.

[45] F. X. Qin, H. X. Peng, L. V. Panina, M. Ipatov, V. Zhukova, A. Zhukov, and J. Gonzalez, "Smart Composites With Short Ferromagnetic Microwires for Microwave Applications," *IEEE Trans. Magn.*, vol. 47, no. 10, pp. 4481–4484, 2011.

[46] F. Qin, C. Brosseau, and H. X. Peng, "In situ microwave characterization of microwire composites under mechanical stress," *Appl. Phys. Lett.*, vol. 99, no. 25, p. 252902, 2011.

[47] F. X. Qin, N. Pankratov, H. X. Peng, M. H. Phan, L. V. Panina, M. Ipatov, V. Zhukova, A. Zhukov, and J. Gonzalez, "Novel magnetic microwires-embedded composites for structural health monitoring applications," *J. Appl. Phys.*, vol. 107, no. 9, p. 09A314, 2010.

[48] E. F. Knott, J. F. Shaeffer, and M. T. Tuley, *Radar Cross Section.* 2nd ed., SciTech, Raleigh, NC, 2004.

[49] S. A. Baranov, "Use of a microconductor with natural ferromagnetic resonance for radio-absorbing materials," *Tech. Phys. Lett.*, vol. 24, no. 7, pp. 549–550, Jul. 1998.

[50] P. Marín, D. Cortina, and A. Hernando, "Electromagnetic Wave Absorbing Material Based on Magnetic Microwires," *IEEE Trans. on Magn.*, vol. 44, no. 11, pp. 3934–3937, Nov. 2008.

[51] S. A. Baranov, M. Yamaguchi, K. Garcia, and M. Vázquez, "Dimensional absorption high-frequency properties of the cast glass coated microwires," *Surf. Eng. Appl. Electrochem.*, vol. 44, no. 6, pp. 425–427, 2008.

[52] H. García-Miquel, J. Carbonell, V. E. Boria, and J. Sánchez-Dehesa, "Experimental evidence of left handed transmission through arrays of ferromagnetic microwires," *Appl. Phys. Lett.*, vol. 94, no. 5, p. 054103, 2009.

[53] J. Carbonell, H. García-Miquel, and J. Sánchez-Dehesa, "Double negative metamaterials based on ferromagnetic microwires," *Phys. Rev. B*, vol. 81, no. 2, pp. 1–6, Jan. 2010.

[54] D. R. Smith, W. J. Padilla, D. C. Vier, S. C. Nemat-Nasser, and S. Schultz, "Composite medium with simultaneously negative permeability and permittivity," *Phys. Rev. Lett.*, vol. 84, pp. 4184–4187, May 2000.

[55] J. Chen, D. Tang, B. Zhang, Y. Yang, M. Lu, H. Lu, F. Lu, and W. Xu, "Left-handed materials made of dilute ferromagnetic wire arrays with gyrotropic tensors," *J. Appl. Phys.*, vol. 102, no. 2, p. 023106, 2007.

[56] J. Jin, S. Liu, Z. Lin, and S. Chui, "Effective-medium theory for anisotropic magnetic metamaterials," *Phys. Rev. B*, vol. 80, no. 11, pp. 1–6, Sep. 2009.

[57] S. Liu, W. Chen, J. Du, Z. Lin, S. Chui, and C. Chan, "Manipulating Negative-Refractive Behavior with a Magnetic Field," *Phys. Rev. Lett.*, vol. 101, no. 15, pp. 11–14, Oct. 2008.

[58] L. Kraus, "Theory of ferromagnetic resonances in thin wires," *Cze. J. Phys.*, vol. 32, no. 11, pp. 1264–1282, Nov. 1982.

[59] R. F. Harrington, *Time-Harmonic Electromagnetic Fields.* New York: McGraw-Hill, 1961.

[60] S. A. Ramakrishna and O. J. F. Martin, "Resolving the wave vector in negative refractive index media." *Opt. Lett.*, vol. 30, no. 19, pp. 2626–8, Oct. 2005.

[61] W. Eggiman, "Scattering of a Plane-Wave on a Ferrite Cylinder at Normal Incidence," *IRE Trans. Microwave Theory Tech.*, vol. 8, no. 4, pp. 440–445, 1960.

[62] C. A. Balanis, *Advanced Engineering Electromagnetics.* New York: Wiley, 1989.

[63] P. A. Belov, C. R. Simovski, and S. A. Tretyakov, "Two-dimensional electromagnetic crystals formed by reactively loaded wires," *Phys. Rev. E*, vol. 66, no. 3, pp. 6610–6616, Sep. 2002.

[64] P. Epstein and A. Berk., “Ferrite Post in a Rectangular Waveguide,” *J. Appl. Phys.*, vol. 27, pp. 1328–1335, 1956.

[65] T. Yoshida, M. Umeno, and S. Miki., “Propagation Characteristics of a Rectangular Waveguide Containig a Cylindrical Rod of Magnetized Ferrite,” *IEEE Trans. Microwave Theory Tech.*, vol. 20, no. 11, pp. 739–743, 1972.

[66] N. Okamoto, I. Nishkioka, and Y. Nakanishi, “Scattering by a Ferrimagnetic Cylinder in a Rectangular Waveguide,” *IEEE Trans. Microwave Theory Tech.*, vol. 19, no. 6, pp. 521–527, 1971.

[67] N. Okamoto and Y. Nakanishi, “Correction to “Scattering by a Ferrimagnetic Cylinder in a Rectangular Waveguide”,” *IEEE Trans. Microwave Theory Tech.*, vol. 20, no. 11, pp. 782–783, 1972.

[68] P. Bhartia, “Correction on “Scattering by a Ferrimagnetic Cylinder in a Rectangular Waveguide”,” *IEEE Trans. Microwave Theory Tech.*, vol. 22, no. 11, p. 975, 1974.

[69] P. C. Waterman and J. C. Pedersen, “Scattering by finite wires of arbitrary ϵ, μ, and σ,” *Journal of the Optical Society of America A*, vol. 15, no. 1, p. 174, 1998.

[70] ——, “Scattering by finite wires,” *J. Appl. Phys.*, vol. 72, no. 2, pp. 349–359, 1992.

[71] P. C. Waterman, “Scattering, absorption, and extiction by thin fibers,” *Journal of the Optical Society of America*, vol. 22, no. 11, pp. 2430–2441, 2005.

[72] S. Alyones, C. W. Bruce, and A. K. Buin, “Numerical Methods for Solving the Problem of Electromagnetic Scattering by a Thin Finite Conducting Wire,” *IEEE Trans. Antennas Propag.*, vol. 55, no. 6, pp. 1856–1861, Jun. 2007.

[73] S. J. Orfanidis, *Electromagnetic Waves and Antennas.* Electronic Book: http://www.ece.rutgers.edu/ orfanidi/ewa/, 2008.

[74] A. Cardama, L. Jofre, J. M. Rius, J. Romeu, S. Blanch, and M. Ferrando, *Antenas.* Edicions UPC, 1998.

[75] S. A. Tretyakov, S. Maslovski, and P. A. Belov, “An analytical model of metamaterials based on loaded wire dipoles,” *IEEE Trans. Antennas Propag.s*, vol. 51, no. 10, pp. 2652–2658, Oct. 2003.

[76] A. Alù and N. Engheta, “Cloaking a sensor,” *Phys. Rev. Lett.*, vol. 102, no. 23, 233901, Jun. 2009.

[77] J. B. Andersen and A. Frandsen, “Absorption Efficiency of Receiving Antennas,” *IEEE Trans. Antennas Propag.*, vol. 53, no. 9, pp. 2843–2849, 2005.

[78] D. H. Kwon and D. Pozar, “Optimal Characteristics of an Arbitrary Receive Antenna,” *IEEE Trans. Antennas Propag.*, vol. 57, no. 12, pp. 3720–3727, Dec. 2009.

[79] I. Liberal and R. W. Ziolkowski, "Analytical and Equivalent Circuit Models to Elucidate Power Balance in Scattering Problems," *IEEE Trans. Antennas Propag.*, vol. 61, no. 5, pp. 2714–2726, 2013.

[80] R. F. Harrington, "On the gain and beamwidth of directional antennas," *IRE Trans. Antennas Propag.*, vol. 6, no. 3, pp. 219–225, 1958.

[81] R. G. Newton, "Optical Theorem and Beyond," *Am. J. Phys.*, vol. 44, no. 7, pp. 639–642, 1976.

[82] C. F. Bohren and D. R. Huffman, *Absorption and Scattering of Light by Small Particles*. New York: Wiley, 1998.

[83] S. D. Campbell and R. W. Ziolkowski, "Impact of strong localization of the incident power density on the nano-amplifier characteristics of active coated nanoparticles," *Opt. Commun.*, vol. 285, no. 16, pp. 3341–3352, Jul. 2012.

[84] I. Liberal, I. Ederra, R. Gonzalo, and R. W. Ziolkowski, "A Multipolar Analysis of Near-Field Absorption and Scattering Processes," *Submitted to IEEE Trans. Antennas Propag.*, vol. 61, no. 5, pp. 2714–2726, 2013.

[85] J. V. Blade, "On the Equivalent Circuit of a Receiving Antenna," *IEEE Antennas and Prop. Mag.*, vol. 44, no. 1, pp. 164–165, 2002.

[86] A. W. Love, "Comment : On the Equivalent Circuit of a Receiving Antenna," *IEEE Antennas Propag. Mag.*, vol. 44, no. 5, pp. 124–125, 2002.

[87] R. E. Collin, "Limitations of the Thevenin and Norton Equivalent Circuits for a Receiving Antenna," *IEEE Antennas Propag. Mag.*, vol. 45, no. 2, pp. 119–124, 2003.

[88] A. Alù and S. I. Maslovski, "Power relations and a consistent analytical model for receiving wire antennas," *IEEE Trans. Antennas Propag.*, vol. 58, no. 5, pp. 1436–1448, May 2010.

[89] N. Engheta, A. Salandrino, and A. Alù, "Circuit elements at optical frequencies: Nanoinductors, nanocapacitors, and nanoresistors," *Phys. Rev. Lett.*, vol. 95, p. 095504, Aug 2005.

[90] L. V. Panina, M. Ipatov, V. Zhukova, A. Zhukov, and J. Gonzalez, "Magnetic field effects in artificial dielectrics with arrays of magnetic wires at microwaves," *J. Appl. Phys.*, vol. 109, no. 5, p. 053901, 2011.

[91] V. Boucher, L.-P. Carignan, T. Kodera, C. Caloz, A. Yelon, and D. Ménard, "Effective permeability tensor and double resonance of interacting bistable ferromagnetic nanowires," *Phys. Rev. B*, vol. 80, no. 22, pp. 9–13, Dec. 2009.

[92] V. Boucher and D. Ménard, "Effective magnetic properties of arrays of interacting ferromagnetic wires exhibiting gyromagnetic anisotropy and retardation effects," *Phys. Rev. B*, vol. 81, no. 17, pp. 1–21, May 2010.

[93] N. Engheta and R. W. Ziolkowski, *Electromagnetic Metamaterials: Physics and Engineering Explorations*. Wiley-IEEE Press, 2006.

[94] A. Sihvola, "Metamaterials in electromagnetics," *Metamaterials*, vol. 1, no. 1, pp. 2–11, Mar. 2007.

[95] J. D. Jackson, *Classical Electrodynamics.* New York: Wiley, 1999.

[96] P. A. Belov, S. A. Tretyakov, and A. Viitanen, "Dispersion and Reflection properties of Artificial Media Formed by Regular Lattices of Ideally Conducting Wires," *J. Electromagn. Waves Appl.*, vol. 16, no. 8, pp. 1153–1170, 2002.

[97] S. I. Maslovski, S. A. Tretyakov, and P. A. Belov, "Wire media with negative effective permittivity: A quasi-static model," *Microwave Opt. Tech. Lett.*, vol. 35, no. 1, pp. 47–51, Oct. 2002.

[98] P. A. Belov, R. Marqués, S. I. Maslovski, I. S. Nefedov, M. Silveirinha, C. R. Simovski, and S. A. Tretyakov, "Strong spatial dispersion in wire media in the very large wavelength limit," *Phys. Rev. B*, vol. 67, no. 11, pp. 1–4, Mar. 2003.

[99] I. S. Nefedov, A. Viitanen, and S. A. Tretyakov, "Propagating and evanescent modes in two-dimensional wire media," *Phys. Rev. E*, vol. 71, no. 4, pp. 1–10, Apr. 2005.

[100] P. Ikonen, E. Saenz, R. Gonzalo, C. R. Simovski, and S. A. Tretyakov, "Mesoscopic effective material parameters for thin layers modeled as single and double grids of interacting loaded wires," *Metamaterials*, vol. 1, no. 2, pp. 89–105, Dec. 2007.

[101] S. I. Maslovski and M. Silveirinha, "Non-local permittivity from a quasi-static model for a class of wire media," *Phys. Rev. B*, vol. 80, no. 24, pp. 245 101–245 110, 2009.

[102] R. Marqués, F. Martín, and M. Sorolla, *Metamaterials with Negative Parameters.* New York: Wiley, 2008.

[103] D. F. Sievenpiper, Z. Lijun, R. Broas, N. Alexopolous, and E. Yablonovitch, "High-impedance electromagnetic surfaces with a forbidden frequency band," *IEEE Trans. Microwave Theory Tech.*, vol. 47, no. 11, pp. 2059–2074, 1999.

[104] S. A. Tretyakov, *Analytical Modeling in Applied Electromagnetics.* Artech House, 2003.

[105] R. Hansen, "Effects of a high-impedance screen on a dipole antenna," *Antennas and Wireless Propagation Letters*, vol. 1, no. 1, pp. 46–49, 2002.

[106] J.-M. Baracco, L. Salghetti-Drioli, and P. de Maagt, "AMC Low Profile Wideband Reference Antenna for GPS and GALILEO Systems," *IEEE Trans. Antennas Propag.*, vol. 56, no. 8, pp. 2540–2547, Aug. 2008.

[107] O. Luukkonen, F. Costa, A. Monorchio, and S. A. Tretyakov, "A Thin Electromagnetic Absorber for Wide Incidence Angles and Both Polarizations," *IEEE Trans. Antennas Propag.*, vol. 57, no. 10, pp. 1–6, 2009.

[108] S. A. Tretyakov and S. I. Maslovski, "Thin absorbing structure for all incidence angles based on the use of a high-impedance surface," *Microwave Opt. Tech. Lett.*, vol. 38, no. 3, pp. 175–178, Aug. 2003.

[109] D. F. Sievenpiper, J. Schaffner, R. Loo, G. Tangonan, S. Ontiveros, and R. Harold, "A Tunable Impedance Surface Performing as a Reconfigurable Beam Steering Reflector," *IEEE Trans. Antennas Propag.*, vol. 50, no. 3, pp. 384–390, 2002.

[110] D. F. Sievenpiper, J. H. Schaffner, S. Member, H. J. Song, R. Y. Loo, and G. Tangonan, "Two-Dimensional Beam Steering Using an Electrically Tunable Impedance Surface," *IEEE Trans. Antennas Propag.*, vol. 51, no. 10, pp. 2713–2722, 2003.

[111] B. A. Munk, *Frequency Selective Surfaces: Theory and Design.* New York: Wiley, 2000.

[112] M. Paquay, J.-C. Iriarte, I. Ederra, R. Gonzalo, and P. de Maagt, "Thin AMC Structure for Radar Cross-Section Reduction," *IEEE Trans. Antennas Propag.*, vol. 55, no. 12, pp. 3630–3638, Dec. 2007.

[113] O. Luukkonen, C. R. Simovski, G. Granet, G. Goussetis, D. Lioubtchenko, A. V. Raisanen, and S. A. Tretyakov, "Simple and Accurate Analytical Model of Planar Grids and High-Impedance Surfaces Comprising Metal Strips or Patches," *IEEE Trans. Antennas Propag.*, vol. 56, no. 6, pp. 1624–1632, Jun. 2008.

[114] P. A. Belov and S. A. Tretyakov, "Resonant Reflection from Dipole Arrays Located Very Near to Conducting Planes," *J. Electromagn. Waves Appl.*, vol. 16, no. 1, pp. 129–143, 2002.

[115] M. Gustafsson and D. Sjoberg, "Physical Bounds and Sum Rules for High-Impedance Surfaces," *IEEE Trans. Antennas Propag.*, vol. 59, no. 6, pp. 2196–2204, 2011.

[116] F. Costa, A. Monorchio, and G. P. Vastante, "Tunable High-Impedance Surface With a Reduced Number of Varactors," *IEEE Antennas Wireless Propag. Lett.*, vol. 10, pp. 11–13, 2011.

[117] V. Twersky, "On the scatttering of waves by an infinite grating," *IRE Trans. Antennas Propag.*, vol. 4, no. 3, pp. 330–345, Jul. 1956.

[118] D. J. Kem, D. H. Werner, and M. J. Wilhelm, "Active Negative Impedance Loaded EBG Structures for the Realization of Ultra-Wideband Artificial Magnetic Conductors," in *IEEE Antennas and Propagation Society International Symposium,*, 2003, pp. 427 – 430.

[119] H. C. Strifors and G. C. Gaunaurd, "Scattering of Electromagnetic Waves by a Perfectly Conducting Cylinder with a Thin Lossy Magnetic Coating," *IEEE Trans. Antennas Propag.*, vol. 48, no. 10, pp. 1528–1532, 2000.

[120] R. L. Fante and M. T. McCormack, "Reflection properties of the salisbury screen," *IEEE Trans. Antennas Propag.*, vol. 36, no. 10, pp. 1443–1454, 1988.

[121] A. Kazemzadeh, "Nonmagnetic Ultrawideband Absorber," *IEEE Trans. Antennas Propag.*, vol. 59, no. 1, pp. 135–140, 2011.

[122] D. P. Makhnovskiy and L. V. Panina, "Field and Stress-Tunable Microwave Composite Materials Based on Ferromagnetic WIres," in *Progress in Ferromagnetism Research*, V. N. Murray, Ed. Hauppauge-NY: Nova Science Publishers, Inc, 2005, pp. 257–295.

[123] K. Mandal, S. Puerta, M. Vázquez, and A. Hernando, "The frequency and stress dependence of giant magnetoimpedance in amorphous microwires," *IEEE Trans. Magn.*, vol. 36, no. 5, pp. 3257–3259, 2000.

[124] CST, Computer Simulation Technology. [Online]. Available: http://www.cst.com/

[125] H. Strifors and G. Gaunaurd, "Scattering of electromagnetic waves by a perfectly conducting cylinder with a thin lossy magnetic coating," *IEEE Trans. Antennas Propag.*, vol. 48, no. 10, pp. 1528–1532, 2000.

[126] A. Sihvola, *Electromagnetic Mixing Formulas and Applications.* The Institution of Engineering and Technology, London, 1999.

[127] D. S, McLachlan, A. Priou, I. Chenerie, E. Issac, and F. Henry, "Modeling the permittivity of composite materials with a general effective medium equation," *J. Electromagn. Waves Appl.*, vol. 6, pp. 1099 – 1131, 1992.

[128] J. J. Benedetto and G. Zimmermann, "Sampling multipliers and the Poisson summation formula," *J. Fourier Anal. Appl.*, vol. 3, no. 5, pp. 505–523, 1997.

[129] "NIST Digital Library of Mathematical Functions," http://dlmf.nist.gov/, Release 1.0.5 of 2012-10-01, online companion to [130]. [Online]. Available: http://dlmf.nist.gov/

[130] F. W. J. Olver, D. W. Lozier, R. F. Boisvert, and C. W. Clark, Eds., *NIST Handbook of Mathematical Functions.* New York, NY: Cambridge University Press, 2010, print companion to [129].

List of Publications

Journal Papers

1. **I. Liberal**, I. Ederra, R. Gonzalo, and R. W. Ziolkowski, "Near-Field Electromagnetic Trapping through Curl-Spin Forces," *Phys. Rev. A* (Accepted), 2013.

2. **I. Liberal**, I. Ederra, R. Gonzalo, and R. W. Ziolkowski, "A Multipolar Analysis of Near-Field Absorption and Scattering Processes," *IEEE Trans. Antennas Propag.* (Submitted), 2013.

3. **I. Liberal** and R. W. Ziolkowski, "Analytical and Equivalent Circuit Models to Elucidate Power Balance in Scattering Problems," *IEEE Trans. Antennas Propag.*, vol. 61, no. 5, pp. 2714-2726, 2013.

4. **I. Liberal**, I. Ederra, and R. Gonzalo, "Fe-Rich Ferromagnetic Wires for Self-Sensing Materials," IEEE *Trans. Microwave Theory Tech.*, vol. 60, no. 9, pp. 2752-2759, 2012.

5. **I. Liberal**, I. Ederra, C. Gómez-polo, A. Labrador, J. I. Pérez-landazábal, and R. Gonzalo, "A Comprehensive Analysis of the Absorption Spectrum of Conducting Ferromagnetic Wires," *IEEE Trans. Microwave Theory Tech.*, vol. 60, no. 7, pp. 2055-2065, 2012.

6. **I. Liberal**, I. Ederra, and R. Gonzalo, "Theory of ferromagnetic wires resonating in the proximity of a ground plane: Application to artificial impedance surfaces," *J. Appl. Phys.*, vol. 111, no. 06, p. 064911, 2012.

7. **I. Liberal**, I. Ederra, J. Teniente, and R. Gonzalo, "Multifrequency

Radiator With Spatial Diversity Based on Metasurfaces," *IEEE Antennas Wireless Propag. Lett.*, vol. 11, pp. 519-522, 2012.

8. **I. Liberal**, I. Ederra, J. Teniente, and R. Gonzalo, "Multi-Functional Antennas Based on Meta-Surfaces," *IEEE Trans Antennas Propag.*, vol. 60, no. 6, pp. 3020-3024, 2012.

9. **I. Liberal**, I. S. Nefedov, I. Ederra, R. Gonzalo, and S. A. Tretyakov, "Reconfigurable Artificial Surfaces Based on Impedance Loaded Wires Close to a Ground Plane," *IEEE Trans Antennas Propag.*, vol. 60, no. 4, pp. 1921-1929, 2012.

10. **I. Liberal**, I. S. Nefedov, I. Ederra, R. Gonzalo, and S. A. Tretyakov, "On the effective permittivity of arrays of ferromagnetic wires," *J. Appl. Phys.*, vol. 110, no. 10, p. 104902, 2011.

11. **I. Liberal**, I. S. Nefedov, I. Ederra, R. Gonzalo, and S. A. Tretyakov, "Electromagnetic response and homogenization of grids of ferromagnetic microwires," *J. Appl. Phys.*, vol. 110, no. 10, p. 104902, 2011.

12. **I. Liberal**, I. Ederra, C. Gómez-Polo, A. Labrador, J. Pérez-Landazabal, and R. Gonzalo, "Theoretical Modeling and Experimental Verification of the Scattering From a Ferromagnetic Microwire," *IEEE Trans. Microwave Theory Tech.*, vol. 59, no. 3, pp. 517-526, 2011.

13. **I. Liberal**, D. Caratelli, and A. Yarovoy, "Conformal antenna array for ultrawideband direction-of-arrival estimation," *Int. J. Microwave Wireless Tech.*, vol. 3, no. 4, pp. 439450, Mar. 2011.

14. D. Caratelli, **I. Liberal**, and A. Yarovoy, "Design and full-wave analysis of conformal ultra-wideband radio direction finders," *IET Microwaves, Antennas Propag.*, vol. 5, no. 10, pp. 1164-1174, 2011.

Invited International Conferences

1. **I. Liberal**, I. Ederra, E. Sáenz and R. Gonzalo, "Multi-frequency Antenna Systems based on Meta-Surfaces", *IWAT*, Hong-Kong, China, March, 2011.

International Conferences

1. **I. Liberal**, I. Ederra, R. Gonzalo and R. W. Ziolkowski "Electromagnetic Forces Produced by Dipole Antennas", *EuCAP*, Goteborg, Sweden, April, 2013.
2. **I. Liberal**, I. Ederra, R. Gonzalo, "Characterization of Ferromagnetic Wires for Self-Sensing Materials", *EuMW*, Amsterdam, The Netherlands, November, 2012.
3. **I. Liberal**, I. Ederra and R. Gonzalo, "Artificial Impedance Surfaces based on Ferromagnetic Wires", *IWAT*, Tucson, USA, March, 2012.
4. **I. Liberal**, I. Ederra, R. Gonzalo, C. Gómez-Polo, A. Labrador, J. I. Pérez-Landazábal, "Experimental Verification of the Electromagnetic Response of Ferromagnetic Microwires", *EuMW*, Manchester, UK, November, 2011.
5. **I. Liberal**, I. Ederra, R. Gonzalo, "Low-Profile Dual-Band Antenna based on Meta-Surfaces", *Metamaterials*, Barcelona, Spain, November, 2011.
6. J. C. Iriarte, J.L. Martínez de Falcón, I. Maestrojuán, **I. Liberal**, A. Rebollo, I. Ederra and R. Gonzalo, "Broadband RCS Reduction Using AMC Technology", *EuCAP*, Rome, Italy, April, 2011.
7. J. C. Iriarte, D. Etayo, I. Palacios, I. Maestrojuan, **I. Liberal**, A. Rebollo, J. Teniente, I. Ederra and R. Gonzalo, "Water Content Evolution in Leaves Based on Active Terahertz Imaging", *EuCAP*, Rome, Italy, April, 2011.
8. **I. Liberal**, I. Ederra and R. Gonzalo, "Analytical Modelling of Amorphous Glass-Coated Microwires for Microwave Applications ", *EuCAP*, Rome, Italy, April, 2011.
9. **I. Liberal**, I. Ederra and R. Gonzalo, "Compact Multi-Frequency Metamaterial-Inspired Antenna ", *EuCAP*, Rome, Italy, April, 2011.
10. **I. Liberal**, I. Ederra and R. Gonzalo, "Design of a Dual-Frequency Highly-Directive Planar Antenna with Meta-Surfaces", *LAPC*, Loughborough, UK, November, 2010.

11. **I. Liberal**, D.Caratelli, A. Yarovoy, R. Cicchetti and M. Russo "Conformal Butterfly Antennas for Ultra-Wideband Radio Direction Finding Applications", *EuMW*, Paris, France, November, 2010.

12. **I. Liberal**, I. Ederra and R. Gonzalo, "Highly-Directive Aperture-Coupled Microstrip Patch Antenna based on Planar Meta-Surface", *IEEE AP-S*, Toronto, Canada, July, 2010.

National Conferences

1. I. Palacios, **I. Liberal**, I. Ederra, J. Teniente, R. Gonzalo"Fabricación de un Mezclador para la Detección de Radiación Sub-mm ", *URSI*, Bilbao, Spain, October, 2010.

2. D. Etayo, J. C. Iriarte, I. Palacios, I. Ederra, J. Teniente, R. Gonzalo, **I. Liberal**, J. L. Martínez de Falcón, Itziar Maestrojuán, "Tecnología de THz para la Caracterización del Contenido en Agua en Plantas", *URSI*, Bilbao, Spain, October, 2010.

3. **I. Liberal**, I. Ederra and R. Gonzalo, "Aplicación de Meta-Superficies como Superstratos en Tecnología Microstrip", *URSI*, Bilbao, Spain, October, 2010.

4. **I. Liberal**, A. Yarovoy and D. Caratelli, "Design and Full-Wave Analysis of Conformal Antenna Arrays for Ultrawide-band Direction-Of-Arrival Estimation", *URSI*, Delft, The Netherlands, June, 2009.